



Technische Universität Dresden
Bereich Mathematik und Naturwissenschaften
Fakultät Physik
Institut für Kern- und Teilchenphysik
Experimentelle Teilchenphysik

Masterarbeit
zur Erlangung des Hochschulgrades
Master of Science
im Studiengang Physik

Systematics Studies for Boosted Tau-Pair Topologies at the ATLAS Experiment

vorgelegt von
Fabian Petsch
geboren am 23.05.1994 in Belzig

eingereicht am 12.12.2018

Erstgutachter: Prof. Dr. Arno Straessner
Zweitgutachter: Prof. Dr. Michael Kobel

Abstract

Decays of tau lepton pairs are important final state signatures in theories that aim to extend the Standard Model of particle physics. In particular, in searches for heavy resonances, e. g. for multi-TeV graviton particles predicted by the Randall-Sundrum model, such pairs of tau leptons are expected to be produced with a high boost. However, the standard tau reconstruction and identification methods employed by the ATLAS experiment at the Large Hadron Collider (LHC) cease to work when the spatial separation between the two taus becomes very low. Accordingly, for both fully-hadronic and semi-leptonic di-tau decays complementary algorithms have been developed.

In this thesis, their performance is evaluated in terms of the agreement between data and Monte Carlo generated events. In the case of the semi-leptonic di-tau decay mode, systematic uncertainties for the reconstruction and identification efficiency as well as for the di-tau energy scale are determined from systematically varied $G_{\text{RS}}^{\text{bulk}} \rightarrow \text{hh} \rightarrow 4\tau$ signal samples. In all relevant kinematic regions, the relative efficiency uncertainties amount to 0.5–3% and 0.1–2% for semi-leptonic di-tau decays with a final state electron or muon, respectively. Equally for both channels, uncertainties of 0.2–2% are derived for the di-tau energy scale. Fully-hadronic di-tau decays are studied in the context of an analysis that extracts the mass peak of the Z boson in boosted $Z \rightarrow \tau\tau$ decays, with 80.4 fb^{-1} recorded by the ATLAS detector at $\sqrt{s} = 13 \text{ TeV}$ in 2015–2017. As a result, scale factors for the di-tau identification are measured. With regard to the $Z \rightarrow \tau\tau(+\text{jets})$ signal events two different Monte Carlo generators are compared. While for Powheg+Pythia8 the di-tau reconstruction is validated with a scale factor that is compatible with one (1.0 ± 0.1), Sherpa 2.2.1 overestimates the event yield of simulated and reconstructed fully-hadronic $Z \rightarrow \tau\tau$ decays which leads to a scale factor of 0.75 ± 0.05 .

Zusammenfassung

Zerfälle von Tau-Lepton-Paaren sind wichtige Signaturen in vielen Theorien, die das Standardmodell der Teilchenphysik versuchen zu erweitern. Insbesondere bei der Suche nach schweren Resonanzen, zum Beispiel beim Zerfall eines Randall-Sundrum Gravitons mit einer Masse von mehreren TeV, erfolgt die Produktion solcher Tau-Paare mit einem großen Impuls. Die Algorithmen, welche standardmäßig zur Rekonstruktion und Identifikation von Tau-Leptonen beim ATLAS-Experiment am Large Hadron Collider zum Einsatz kommen, funktionieren nur noch sehr eingeschränkt, wenn der räumliche Abstand zwischen zwei Tau-Zerfällen gering ist. In diesem Zusammenhang wurden ergänzende Methoden entwickelt, um derartige geboostete Di-Tau-Objekte zu rekonstruieren, sowohl im Falle von semi-leptonischen als auch für voll-hadronische Zerfälle.

Im Rahmen dieser Arbeit wird die Leistungsfähigkeit der Di-Tau-Algorithmen in Bezug auf die Übereinstimmung von gemessenen Ereignissen und solchen, die mit Hilfe von Monte-Carlo-Simulationen erzeugt wurden, untersucht. Für die semi-leptonischen Zerfallskanäle werden systematische Unsicherheiten für die Rekonstruktions- und Identifikationseffizienzen sowie für die Energiekalibrierung der Di-Taus bestimmt. Die Berechnung erfolgt mittels systematisch variiertes Simulations-Datensätze für das $G_{RS}^{\text{bulk}} \rightarrow hh \rightarrow 4\tau$ -Signal. Die relativen Unsicherheiten bezüglich der Effizienzen ergeben 0.5–3% und 0.1–2% für semi-leptonische Di-Tau-Zerfälle mit jeweils einem Elektron bzw. Muon im Endzustand, und zwar in allen relevanten kinematischen Bereichen. Die Unsicherheiten für die Energieskala belaufen sich, unabhängig vom jeweiligen semi-leptonischen Endzustand, auf 0.2–2%. Die Untersuchung voll-hadronischer Di-Tau-Endzustände erfolgt im Kontext einer Analyse, die nach Zerfällen von geboosteten Z-Bosonen sucht. Dabei stehen 80.4 fb^{-1} an Daten zur Verfügung, die in den Jahren von 2015 bis 2017 vom ATLAS-Detektor bei einer Schwerpunktsenergie von 13 TeV aufgenommen wurden. Für ein ausgewähltes Massenfenster der Z-Resonanz werden Skalierungsfaktoren für die Di-Tau-Identifikation bestimmt. Bezogen auf die simulierten Signal-Datensätze, d.h. für $Z \rightarrow \tau\tau(+\text{jets})$ -Ereignisse, werden zwei verschiedene Monte Carlo Ereignis-Generatoren verglichen. Für Powheg+Pythia8 kann die Di-Tau-Rekonstruktion durch einen mit Eins kompatiblen Skalierungsfaktor (1.0 ± 0.1) validiert werden, wohingegen die Simulation mittels Sherpa 2.2.1 signifikant mehr rekonstruierte voll-hadronische $Z \rightarrow \tau\tau$ -Zerfälle ergibt, als die gemessenen Verteilungen zeigen. Entsprechend ergibt sich ein Skalierungsfaktor von 0.75 ± 0.05 .

Contents

1. Introduction	1
2. Theoretical Framework	3
2.1. The Standard Model	3
2.1.1. Phenomenology and Particle Content	4
2.1.2. Lagrangian Formulation	5
2.2. Physics of Tau Leptons	7
2.3. The Z Resonance	9
2.4. The Randall-Sundrum Model	13
3. The LHC and the ATLAS Detector	18
3.1. The LHC	18
3.2. The ATLAS Detector	19
3.2.1. The Inner Detector	21
3.2.2. The Calorimeter System	21
3.2.3. The Muon Spectrometer	22
3.2.4. The Trigger System	23
4. Reconstruction and Identification of High-Level Objects at ATLAS	25
4.1. Electrons	25
4.2. Muons	26
4.3. Jets	27
4.4. Taos	28
4.5. Missing Transverse Energy	29
5. Reconstruction and Identification of Boosted Di-Taos	30
5.1. Fully-Hadronic Di-Tau Decays	31
5.2. Semi-Leptonic Di-tau Decays	33
5.2.1. Semi-Leptonic Decays with a Final State Electron	33
5.2.2. Semi-Leptonic Decays with a Final State Muon	34
5.3. Performance and Validation	34
6. Systematic Uncertainties for Semi-Leptonic Di-Tau Decays	36
6.1. Graviton Samples with Systematic Variations	36
6.2. Systematic Uncertainties for the Reconstruction and Identification Efficiency	37
6.3. Systematic Uncertainties for the Di-Tau Energy Scale	42

6.4. Summary for the Semi-Leptonic Di-Tau Decays	44
7. Validation Studies for Boosted Di-Taus in Z+jets Events	48
7.1. Data and Monte Carlo Samples	48
7.2. Boosted Topology	49
7.3. Event Selection	51
7.4. Estimation of QCD Fakes	53
7.5. Description of the Signal Region	57
7.6. Identification Scale Factors	58
7.7. $Z \rightarrow \tau\tau(+\text{jets})$ Studies for Semi-Leptonic Di-Tau Decays	65
8. Summary	67
9. Outlook	69
Bibliography	71
A. Performance Plots for the Boosted Di-Tau Algorithms	79
B. Data and Monte Carlo Samples	81
B.1. Graviton Signal Samples	81
B.2. Samples for the Z+jets Validation Studies	84
C. Additional Plots for the Z+jets Validation Studies	100

1. Introduction

Particle physics, which aims to explain the fundamental composition of the universe, has a rich history that reaches back no further than about one and a half centuries. With the discovery of the electron by J.J. Thomson [1] as the first sub-atomic particle, the substructure of the atom could be unravelled, and shortly afterwards its description was placed on a quantum-mechanical foundation by N. Bohr and E. Rutherford. Although by then studies of cosmic rays had revealed a variety of elementary particles, including the first evidence for anti-matter [2], the onset of the hunt for the ever smaller did not really happen until the early 1950s, when modern accelerator and detector technology became available.

In the 1970s, the growing collection of both experimental evidence and theoretical knowledge culminated in the Standard Model, one of the cornerstones of modern physics. Since its beginnings, many new elementary particles have been discovered, be it the tau lepton [3] and its neutrino [4], the gluon [5], the W/Z resonances [6–9], the top quark [10, 11] or the Higgs boson [12, 13], and the Standard Model has made impressively precise forecasts of their properties and interactions. All in all, this probably makes it the best supported theory ever.

However, the Standard Model has some important limitations, as for example it cannot incorporate a theory of gravity. The Randall-Sundrum model [14, 15] provides a possible solution to this shortcoming. Since it predicts graviton particles and their corresponding Kaluza-Klein excitations to lie on the TeV scale, such kind of heavy resonances might be found by the ATLAS experiment at the Large Hadron Collider. In particular, the decay of a Randall-Sundrum graviton into two SM-like Higgs bosons and a pair of boosted b-quarks and tau-leptons in the final state poses an interesting experimental signature.

In this thesis, the performance of the reconstruction and identification for boosted pairs of tau leptons is studied, for both di-tau decays with two hadronically decaying taus [16] and the case where either of the them results in a final state electron or muon [17]. The obtained systematic uncertainties and scale factors for the di-tau identification are intended to be of use for the $G_{\text{RS}}^{\text{bulk}} \rightarrow hh \rightarrow bb\tau\tau$ analysis.

The thesis is organised as follows: Chapter 2 begins with an outline of the Standard Model, both in phenomenology and theory, whilst emphasis is put on the physics of tau leptons and the Z boson resonance as a well-known benchmark process. Chapter 3 gives some technical insights into the ATLAS detector at the LHC, for which the di-tau algorithms have been developed. Every physical object that is of relevance to searches carried out at ATLAS is reconstructed by a dedicated algorithm, as explained in chapter 4. On this basis, chapter 5 introduces sophisticated methods to capture highly boosted tau pairs, via both their semi-leptonic and fully-

1. Introduction

hadronic decay modes. As a means of evaluating and validating their performance in both measured and Monte Carlo generated data, two corresponding approaches are presented thereafter. In chapter 6, systematic uncertainties for the identification efficiency and energy scale of semi-leptonic di-tau decays are determined. Finally, chapter 7 investigates the fully hadronic di-tau final state, originating from boosted Z bosons, while calculating scale factors for the di-tau identification procedure.

2. Theoretical Framework

This chapter aims to explain the context of the thesis whilst introducing key ideas of its theoretical foundation. A brief summary of the Standard Model of particle physics (see section 2.1), presented in both a phenomenological and a mathematical description, is followed by an introduction to the physics of tau leptons (see section 2.2). In section 2.3, the Z resonance is explored from a historical and a physics point of view. Lastly, in section 2.4 a possible way to incorporate quantum-level gravity into the Standard Model is suggested, whilst thereby resolving one of its shortcomings, i. e. the hierarchy problem.

2.1. The Standard Model

The Standard Model is the most successful theory that high energy physics currently knows of, in the sense that its predictions withstood many experimental tests throughout the past decades. It is a relativistic quantum field theory and as such forms a synthesis of many theoretical concepts, e. g. scattering theory, special relativity and many-body quantum mechanics, whilst providing a description that is in accordance with both the particle- and wave-like nature of matter. Historically [18], its beginnings are marked by a combination of quantum electrodynamics (QED), the already existing formulation of electromagnetism in the quantum realm, and a theory for weak interactions by Glashow in 1961 [19]. However, it was not yet understood how a mechanism that would give mass to the heavy gauge bosons but at the same time leave the photon massless could be introduced to the model. Preferably, this had to be done without giving up on the concept of gauge theories and whilst keeping the theory renormalizable. This issue was addressed by Englert and Brout [20], Higgs [21] and Guralnik et al. [22] in 1964, who independently suggested the existence of a novel scalar field, whose excitations are now famously known as Higgs bosons. The mass problem would then be solved through a process called spontaneous symmetry breaking. Shortly afterwards, in 1967, Weinberg completed the electroweak picture by combining the above-mentioned suggestions and also adding mass terms for the fermions [23]. Finally, in the 1970s, the last piece of the puzzle, a description of the strong force, was added in the form of quantum chromodynamics (QCD). Thereby the Standard Model got extended by a classical Yang-Mills theory [24], which also lies at the core of the electroweak sector.

2.1.1. Phenomenology and Particle Content

Elementary particles, which are described as excitations of quantum fields, form the basic building blocks of nature. In total, the Standard Model counts 25 of these fundamental constituents. Within this simple concept, they may be grouped into those that make up the universe’s matter content and those that mediate either the electromagnetic, weak or strong force. The former class solely consists of massive spin- $\frac{1}{2}$ -particles, which makes them fermions according to the spin-statistics theorem [25]. The interactions any type of matter particle undergoes depends on the charge properties it possesses. In this context, the term ‘charge’ may refer to the electromagnetic charge, the weak hypercharge or the color charge (red, green or blue) carried by strongly interacting particles. The twelve fermions of the Standard Model (see table 2.1) are further subdivided into quarks and leptons, indicating if they are influenced by the strong force or not. For each of them, there exists a matching anti-particle of equal mass but with opposite charge, which is implicitly included in the following discussion.

With respect to their lightest siblings, we distinguish between up-type (u,c,t) and down-type (d,s,b) quarks. Since no free colour charges have been observed, quarks may only exist in colourless bound states which are called hadrons. These include pairings of a quark and an anti-quark (mesons) where a certain colour and anti-colour cancel each other out, states of three quarks (baryons) with a red, a green and a blue constituent in analogy to additive colour mixing as well as exotic tetra- [26] and pentaquark states [27]. Furthermore, this confinement is explained by the fact that in QCD the potential increases linearly at large distances.

For every lepton (e, μ, τ) with $Q = -1$ there exists an electrically neutral counterpart, i. e. a neutrino (ν_e, ν_μ, ν_τ)¹. Since the weak force violates parity [30], the electroweak theory needs to account for this chiral asymmetry. The fermionic fields are hence split into left-handed doublets and right-handed singlets², though no electrically neutral leptons that show a right-chiral behaviour have been observed so far and are thus not incorporated into the model.

Moreover, the fermions are sorted into three generations. This does not only reflect the historical order of their discovery and sorts them according to their masses³ but also puts them into groups of particles sharing an identical set of quantum numbers. This set contains the electromagnetic charge Q , the third component of the weak isospin I_W^3 and the weak hypercharge Y_W , which are related by the Gell-Mann-

¹Neutrinos are special in the sense that they change their flavour when propagating through space. The confirmation of these oscillations proved that neutrinos do have mass, albeit very little and of unknown value. Several experiments that relate to the neutrino masses are under way, e. g. in order to investigate the mass hierarchy (the ORCA [28] detector of KM3NeT in the Mediterranean Sea) or to measure their absolute values (KATRIN [29] at Karlsruhe in case of the electron neutrino).

²With the help of the projection operator $P_{L,R} = \frac{1}{2}(1 \mp \gamma_5)$ we obtain $\psi = \psi_L + \psi_R = P_L\psi + P_R\psi$.

³In case of the leptons we have the electron, muon and tau with $m_e = 511$ keV, $m_\mu = 106$ MeV and $m_\tau = 1.78$ GeV which were discovered by J.J.Thomson in 1897 [1], C. D. Anderson and S. Neddermeyer in 1937 [31] and M. L. Perl et al. in 1975 [3] respectively.

Nishijima formula

$$Q = I_W^3 + Y_W. \quad (2.1)$$

The mediator particles (see table 2.2) are bosonic and therefore carry a spin of one. The massless gluons come in eight independent states of different colour and anti-colour admixtures. In contrast to the electrically neutral photons in QED they are therefore able to self-interact. The Z and W^\pm bosons, which also couple to one another in certain combinations ⁴, give rise to the weak force. The photon, the Z boson and the gluons are their own anti-particles.

The masses of all Standard Model particles are generated with the help of the spinless Higgs boson, by a mechanism that is explained in more detail in 2.1.2.

Table 2.1.: Fermions of the Standard Model.

	Generation			I_W^3	Y_W	C
	1	2	3			
Leptons	$\begin{pmatrix} \nu_e \\ e \end{pmatrix}_L$	$\begin{pmatrix} \nu_\mu \\ \mu \end{pmatrix}_L$	$\begin{pmatrix} \nu_\tau \\ \tau \end{pmatrix}_L$	$\frac{1}{2}$	$-\frac{1}{2}$	0
	e_R	μ_R	τ_R	$-\frac{1}{2}$	$-\frac{1}{2}$	-1
				0	-1	-1
Quarks	$\begin{pmatrix} u \\ d \end{pmatrix}_L$	$\begin{pmatrix} c \\ s \end{pmatrix}_L$	$\begin{pmatrix} t \\ b \end{pmatrix}_L$	$\frac{1}{2}$	$\frac{1}{6}$	$\frac{2}{3}$
	u_R	c_R	t_R	$-\frac{1}{2}$	$\frac{1}{6}$	$-\frac{1}{3}$
	d_R	s_R	b_R	0	$\frac{2}{3}$	$\frac{2}{3}$
			0	$-\frac{1}{3}$	$-\frac{1}{3}$	

Table 2.2.: Bosons of the Standard Model.

	Force	Mass
γ	electromagnetic	0
W^\pm	} weak	80.4 GeV
Z		91.2 GeV
g	strong	0
h	-	125.2 GeV

2.1.2. Lagrangian Formulation

The Standard Model is a local gauge theory with the underlying symmetry group $SU(3)_c \times SU(2)_I \times U(1)_Y$, where the subscripts correspond to the colour charge of QCD, the weak isospin I_W and the weak hypercharge Y_W .

⁴This has been confirmed very recently by the ATLAS Collaboration for the $W^\pm W^\pm \rightarrow W^\pm W^\pm$ [32] and $W^\pm Z \rightarrow W^\pm Z$ [33] channels.

2. Theoretical Framework

The Lagrangian density \mathcal{L}_{SM} of the Standard Model,

$$\mathcal{L}_{\text{SM}} = \mathcal{L}_{\text{gauge}} + \mathcal{L}_{\text{ferm}} + \mathcal{L}_{\text{H}} + \mathcal{L}_{\text{Yuk}}, \quad (2.2)$$

may be grouped into four terms that describe the kinematics and self-interaction of the gauge fields ($\mathcal{L}_{\text{gauge}}$), the fermionic interactions ($\mathcal{L}_{\text{ferm}}$), the Higgs sector (\mathcal{L}_{H}) and the Yukawa couplings and mass terms of the fermions (\mathcal{L}_{Yuk}). $\mathcal{L}_{\text{gauge}}$ expands to

$$\mathcal{L}_{\text{gauge}} = -\frac{1}{4}W_{\mu\nu}^i W^{i,\mu\nu} - \frac{1}{4}B_{\mu\nu} B^{\mu\nu} - \frac{1}{4}G_{\mu\nu}^a G^{a,\mu\nu} \quad (2.3)$$

with the field-strength tensors related to the gauge fields W_{μ}^i for $\text{SU}(2)_{\text{I}}$, B_{μ} for $\text{U}(1)_{\text{Y}}$ and G_{μ}^a for $\text{SU}(3)_{\text{c}}$. The second term,

$$\mathcal{L}_{\text{ferm}} = \sum_f i\bar{L}\gamma^{\mu}D_{\mu}L + i\bar{R}\gamma^{\mu}D_{\mu}R \quad (2.4)$$

introduces the fermionic Dirac spinors, summed over all left-handed doublets L and right-handed singlets R as listed in table 2.1. Here, the four-gradient ∂_{μ} has been replaced by the covariant derivative

$$D_{\mu} = \partial_{\mu} + ig_{\text{W}}T^iW_{\mu}^i + g_{\text{Y}}Y_{\text{W}}B_{\mu} + ig_{\text{S}}T_{\text{c}}^aG_{\mu}^a, \quad (2.5)$$

which is of central importance when constructing Yang-Mills theories in general. It not only contains the actual interaction between the matter multiplets and the gauge fields but also ensures the theory's gauge invariance. Here we denote the coupling constants for the $\text{SU}(2)_{\text{I}}$, $\text{U}(1)_{\text{Y}}$ and $\text{SU}(3)_{\text{c}}$ as g_{W} , g_{Y} and g_{S} , respectively. The symmetry groups' generators are $T^i = \sigma^i/2$ for the left-handed doublets with the Pauli matrices σ^i , the weak hypercharge Y_{W} and $T_{\text{c}}^a = \lambda^a/2$ for the quark-triplets with the Gell-Mann matrices λ^a ⁵.

The Higgs term [34]

$$\mathcal{L}_{\text{H}} = (D_{\mu}\phi)^{\dagger}D^{\mu}\phi - V(\phi) \quad (2.6)$$

adds the complex scalar field ϕ that forms a weak isospin doublet. Its potential (see figure 2.1)

$$V(\phi) = \mu^2\phi^{\dagger}\phi + \lambda(\phi^{\dagger}\phi)^2 \quad (2.7)$$

has two parameters μ and λ , where $\lambda > 0$ is required by vacuum stability [35] and choosing $\mu^2 < 0$ ensures a non-zero vacuum expectation value. The ground state is calculated by minimising the potential, which leads to

$$\phi_0 = \begin{pmatrix} 0 \\ \frac{v}{\sqrt{2}} \end{pmatrix} \quad \text{with} \quad v = \sqrt{-\frac{\mu^2}{\lambda}} \quad (2.8)$$

and breaks the $\text{SU}(2)_{\text{I}} \times \text{U}(1)_{\text{Y}}$ invariance to a $\text{U}(1)_{\text{C-QED}}$ symmetry. Commonly, ϕ is then rotated in $\text{U}(1)_{\text{C}}$ space and rewritten in the so-called unitary gauge

$$\phi = \begin{pmatrix} 0 \\ \frac{1}{\sqrt{2}}(v + \text{H}(x)) \end{pmatrix} \quad (2.9)$$

⁵For the right-handed singlets we have $T^i = 0$ and for the leptons $T_{\text{c}}^a = 0$

with the physical Higgs field H . Inserting this into \mathcal{L}_H then directly displays the physical content of the theory, including bilinear terms in W^\pm and Z that generate their masses and the Higgs mass and self-coupling terms from its potential.

In the the last part of \mathcal{L}_{SM} , written in unitary gauge,

$$\mathcal{L}_{\text{Yuk}} = -\frac{1}{\sqrt{2}} \sum_{\text{f}} \lambda_{\text{f}} (\bar{L}R + \bar{R}L)(v + H), \quad (2.10)$$

the Yukawa couplings λ_{f} relate to the fermion masses by

$$m_{\text{f}} = \frac{\lambda_{\text{f}}}{\sqrt{2}}. \quad (2.11)$$

Currently, it is not yet understood how the neutrino masses have to be incorporated into the model. They might for example appear as massive Dirac fields as the other fermions or as Majorana particles ⁶.

From the Lagrangian formulation of the Standard Model with massless neutrinos we can thus read 14 out of its 18 degrees of freedom, the gauge couplings g_W , g_Y and g_S , the nine Yukawa coupling constants λ_{f} and the two parameters λ and μ from the Higgs potential. The final four parameters originate from the CKM-matrix that describes the mixing of quark mass and flavour eigenstates.

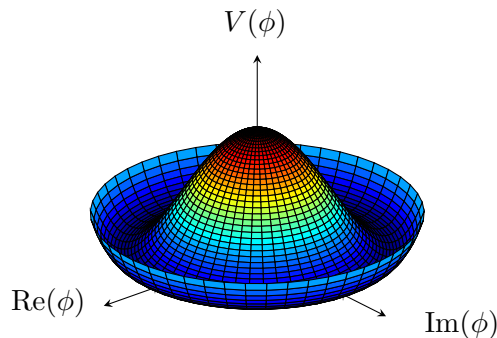


Figure 2.1.: Potential of the complex scalar Higgs field ϕ .

2.2. Physics of Tau Leptons

The tau lepton is the heaviest of the three leptons with $m_\tau = (1776.86 \pm 0.12) \text{ MeV}$ [36]. It has a very short lifetime $\tau = 2.90 \times 10^{-13} \text{ s}$ compared to e. g. the muon with $\tau = 2.20 \times 10^{-6} \text{ s}$ and is therefore almost exclusively detected via its decay products. Tau leptons decay weakly as illustrated

⁶Majorana particles are their own antiparticles

2. Theoretical Framework

in 2.2, always producing a tau neutrino. The main decay modes are summarized in figure 2.3. In about one third of all cases, the intermediate W^- boson creates a lepton-antineutrino pair, with almost equal shares for electrons and muons. Due to the tau leptons high mass, hadronic decay modes are also kinematically possible. Most frequently, they lead to final states with one or three charged ($m_{\pi^\pm} = 140$ MeV) and up to two neutral ($m_{\pi^0} = 135$ MeV) pions. Generally, charge conservation requires an odd number of charged pions. Though decays with five charged pions are possible, they are very rare and are not relevant to most analyses associated to tau leptons. The remaining branching fraction is mostly accounted for by channels that involve charged or neutral kaons. The anti-tau lepton undergoes the same, albeit charge conjugated decay modes.

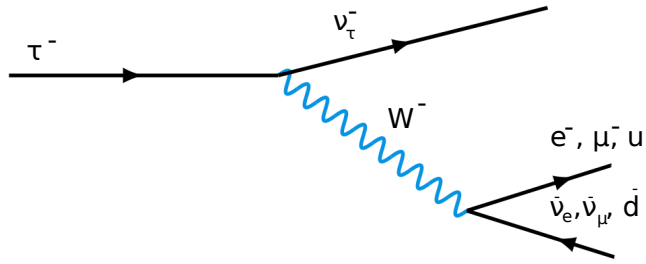


Figure 2.2.: Feynman diagram of the tau decay.

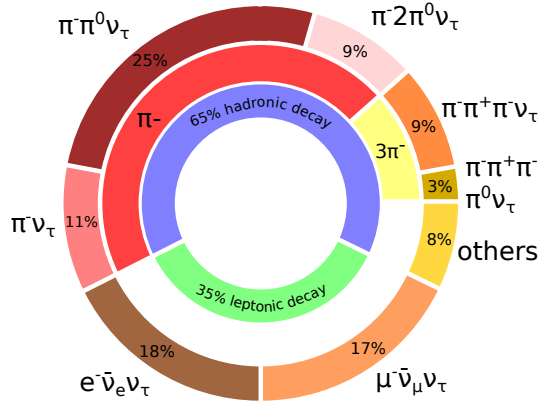


Figure 2.3.: Tau decay modes [36].

2.3. The Z Resonance

The Z resonance does not only present an interesting field of study in itself, but also has been and still is a very important benchmark process. After a brief review of the properties of the Z boson, a chronological outline of the research involving its resonance is given. According to the different production facilities, the most important physics processes are also explained.

Properties of the Z boson

The Z boson was discovered in 1983 at CERN's Super Proton Synchrotron (SPS). It is an electrically neutral vector boson with a spin of one that mediates the weak force together with its charged cousins, the W^\pm bosons. Due to its high mass of $m_Z = 91.2 \text{ GeV}$ and decay width of $\Gamma_Z = 2.5 \text{ GeV}$ [36] it has a very short life time of about $1 \times 10^{-25} \text{ s}$. In contrast to the photon, the Z boson therefore appears as an intermediate state and is experimentally only accessible via its decay products. Apart from the allowed electroweak gauge boson self-couplings and the interaction with the Higgs boson, the couplings to matter particles exclusively happen for fermion-antifermion pairs with branching fractions illustrated in figure 2.4. These couplings are not equal for the left-handed fermion and right-handed antifermion states. This behaviour gives an experimental handle on the weak mixing angle [37] which is an important parameter of the electroweak sector of the Standard Model ⁷.

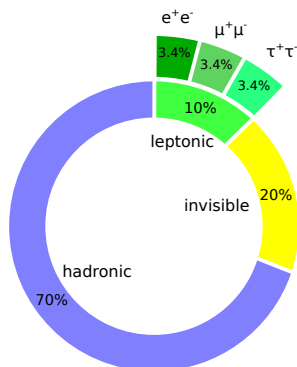


Figure 2.4.: Branching fractions of the Z boson [36]. The categories termed hadronic and invisible combine the decays into quark-antiquark and neutrino-antineutrino pairs respectively.

⁷The weak mixing angle θ_W can for instance be expressed in terms of the vector boson masses $\cos \theta_W = \frac{m_W}{m_Z}$.

2. Theoretical Framework

Electroweak studies at e^+e^- accelerators

In the 1990s, the Large Electron Positron Collider (LEP) at CERN and the Stanford Linear Collider (SLC) studied the parameters of the Z resonance in great detail and thereby also performed high precision electroweak measurements. They were designed to produce large numbers of Z bosons and to operate at $\sqrt{s} \approx m_Z$. The results published by the LEP Electroweak Working Group and the SLD collaborations [38] combine the datasets of the two accelerators and still hold the most precise values for the mass and width of the Z boson, i. e. $m_Z = (91.1875 \pm 0.0021)$ GeV and $\Gamma_Z = (2.4952 \pm 0.0023)$ GeV. With a relative uncertainty of $2.2 \times 10^{-5} \%$, this makes m_Z one of the best known parameters of the Standard Model. To make this possible, LEP carried out several runs dedicated to centre-of-mass energies at and around the Z pole. The corresponding cross sections are summarized in figure 2.5. A set of parameters that describe the resonance was then fitted to the lineshape. Although it is of course possible to extract m_Z directly from the invariant mass spectrum of its decay products, this method induces larger systematic uncertainties. The lineshape approach however poses a simple counting problem.

The leading order contributions to the lineshape are illustrated in 2.6. For centre-of-mass energies well below the Z peak, only $e^+e^- \rightarrow f\bar{f}$ scattering via photon exchange has to be considered and the lineshape can be described by the QED cross section

$$\sigma_\gamma = \frac{4\pi\alpha^2}{3s} Q_f^2 \sim \frac{1}{s}. \quad (2.12)$$

For $\sqrt{s} \approx m_Z$, this process becomes negligible whilst the diagram with the intermediate Z boson dominates. In fact, the simple leading order evaluation as in figure 2.6 then is insufficient, since replacing the photon propagator by the Z propagator, which is proportional to

$$\frac{1}{q^2 - m_Z^2} \quad (2.13)$$

leads to a divergent matrix element. This issue is only solved by corrections from vacuum polarizations to the propagator which might be interpreted as an account for the unstableness of the Z boson. This higher order calculation leads to the Breit-Wigner distribution

$$\sigma_Z = \frac{12\pi s}{m_Z^2} \frac{\Gamma_{ee}\Gamma_{ff}}{(s - m_Z^2)^2 + m_Z^2\Gamma_Z^2}, \quad (2.14)$$

around the Z peak. In between the two cases for σ_γ and σ_Z , for $\sqrt{s} \approx 50 - 80$ GeV, and also for $\sqrt{s} \gg m_Z$ both processes are of equal importance. However, in order to make precision fits to the lineshape, corrections from higher processes, e. g. initial and final state radiation, have to be considered.

Measurements at the LHC

At pp -colliders such as the LHC, Z bosons are produced by parton-level interactions. The dominant production mode is the so-called Drell-Yan (DY) process [39]. On

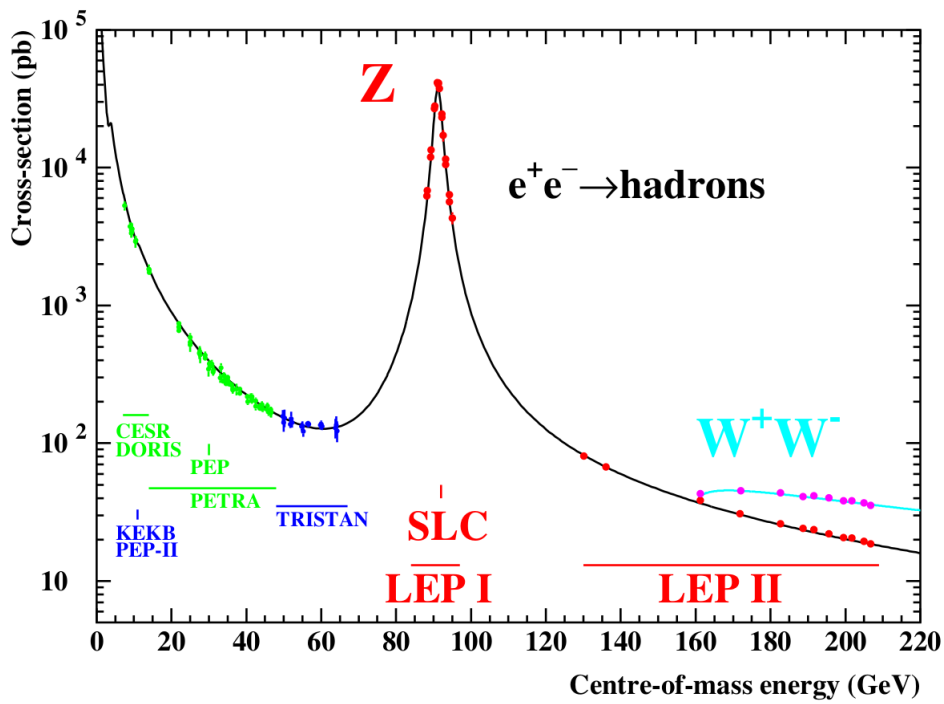


Figure 2.5.: Lineshape of the Z resonance from the hadronic cross section, comparing the SM prediction (solid line) and the measurement results provided by various electron-positron colliders [38].

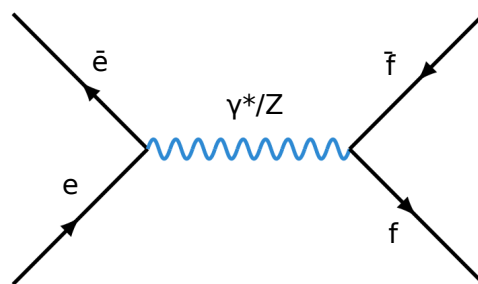


Figure 2.6.: Leading order contributions to the Z lineshape at e^+e^- -colliders.

2. Theoretical Framework

a first note, it is very similar to the e^+e^- -annihilation that has been discussed in the previous section (see figure 2.7). In fact, at leading order the quark-level cross section can heuristically be obtained from equation 2.12. Replacing Q_f with Q_q and adding a factor $\frac{1}{N_c}$ where $N_c = 3$ in order to ensure colour conservation ⁸ gives

$$\sigma_{qq} = \frac{1}{N_c} \frac{4\pi\alpha^2}{3s} Q_q^2. \quad (2.15)$$

In order to arrive at the cross section for the full DY process, σ_{qq} is rewritten in its differential form, depending on the momentum fractions x_1 , x_2 of the quark and antiquark with respect to the proton momenta. The outcome is folded with the corresponding parton distribution functions (PDFs) $f_q(x_1)$ and $f_{\bar{q}}(x_2)$ ⁹. Summing over all possible parton pairs finally leads to

$$\sigma(pp \rightarrow f\bar{f} + X) = \sum_{q,\bar{q}} \int_0^1 \int_0^1 f_q(x_1) f_{\bar{q}}(x_2) \frac{\partial^2 \sigma(q\bar{q} \rightarrow f\bar{f})}{\partial x_1 \partial x_2} dx_1 dx_2. \quad (2.16)$$

Since s in equation (2.15) still refers to the $q\bar{q}$ -system, it is usually replaced by $s = x_1 x_2 \tilde{s}$ for the colliding protons in the limit where $\sqrt{\tilde{s}} \gg m_p$. Moreover, the differential DY cross sections are usually expressed in variables that are easier to observe by the experiments than x_1 and x_2 , e.g. the invariant mass m_{inv} or the rapidity y of the fermion system. The determination of these multi-differential cross sections also allows for comparisons of different PDFs and therefore presents a nice synergy between theory and experiment.

Though owing to the partonic interactions the Drell-Yan process is more complex than e^+e^- -annihilation, it is actually the theoretically best explored hadronic process and provides an interface between QED and QCD. In fact, it was the first one to be calculated at next-to-next-to leading order (NNLO) in perturbative QCD (pQCD) ¹⁰. Though the higher order QCD corrections are more substantial, electroweak contributions up to NLO have to be considered when the uncertainties on the theoretical DY cross section are to reach the percent-level. Both the ATLAS and CMS collaborations have put great effort into validating these predictions in the low-mass ($26 \text{ GeV} < m_{\text{inv}} < 66 \text{ GeV}$) [40], high-mass ($116 \text{ GeV} < m_{\text{inv}} < 1500 \text{ GeV}$) [41] and Z regime ($46 \text{ GeV} < m_{\text{inv}} < 200 \text{ GeV}$) [42].

Besides this, the DY process has many more use cases at the LHC. For many analyses, it is an important background process. This is true especially for the rediscovery of the SM-like Higgs boson in the $h \rightarrow \tau\tau$ channel ¹¹ and the search

⁸Out of the nine possible colour combinations for the quark and antiquark, only $r\bar{r}$, $b\bar{b}$, $g\bar{g}$ can contribute.

⁹The PDFs are probability density functions that describe the likelihood of finding a parton of a specific flavour with a certain momentum fraction.

¹⁰In pQCD, observables such as the cross section are expanded in orders of the strong coupling constant $\alpha_s = \frac{g_s^2}{4\pi}$

¹¹Since the coupling of the Higgs boson to fermions is proportional to m_f , $H \rightarrow e\bar{e}$ and $H \rightarrow \mu\bar{\mu}$ are much more difficult to observe. Though $H \rightarrow e\bar{e}$ is far beyond the reach of the LHC, $H \rightarrow \mu\bar{\mu}$ will be accessible for the HL-LHC [43, 44].

for heavy neutral bosons (Z' bosons) [45] that may exist beyond the realm of the Standard Model. While the Z' search is interested in the TeV-range and therefore quite far away from the actual Z pole, for $h \rightarrow \tau\tau$ the signal lies close to the $Z \rightarrow \tau\tau$ background and separating them needs an adequate mass resolution.

Taking yet another perspective, the Z decay to charged leptons commonly serves as a standard candle with various applications, e. g. for detector calibrations or efficiency measurements of the respective particles. From an experimental standpoint, the Z decay to light leptons, i. e. electrons or muons, provides a very clean signature with a good kinematic resolution and a high background rejection (see figure 2.8). The channels that include hadrons in the final state are only ever considered for very large energies, when the overwhelming QCD background is kinematically suppressed. For the purpose of this thesis however, the relevant Z decay mode is $Z \rightarrow \tau\tau$, which has a signature that is by far not as clean as for $Z \rightarrow ee$ or $Z \rightarrow \mu\mu$. This is mainly due to the multiple final states as explained in section 2.2 and the involvement of neutrinos. Nevertheless, it is used to test the reconstruction of tau leptons, e. g. for measuring the identification efficiency in $Z \rightarrow \tau\tau$ enriched data samples via a tag-and-probe method or for calibrating the tau energy scale (TES) [46]. The distributions of the visible mass m_{vis} of the $\tau_{\text{had}}\tau_{\mu}$ system, which are used for the TES calibration, are shown in figure 2.9. Evaluating the tau performance is an important step since many analyses, e. g. $h \rightarrow \tau\tau$, rely on it. The measurements in [46] employ a resolved strategy where the tau leptons are well separated and isolated. When further kinematic constraints are put on the two taus like in the boosted regime, studying the Z mass peak becomes even more challenging.

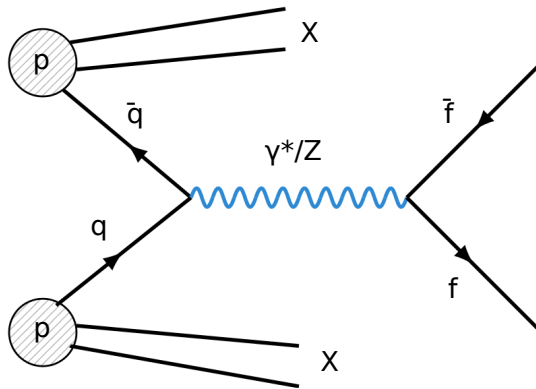


Figure 2.7.: Drell-Yan process at proton-proton colliders.

2.4. The Randall-Sundrum Model

The Standard Model is commonly believed to be an effective theory that is valid up to very high energies, where it has to be extended by a model that at least includes gravity. The corresponding cut-off value might lie at the Planck scale with

2. Theoretical Framework

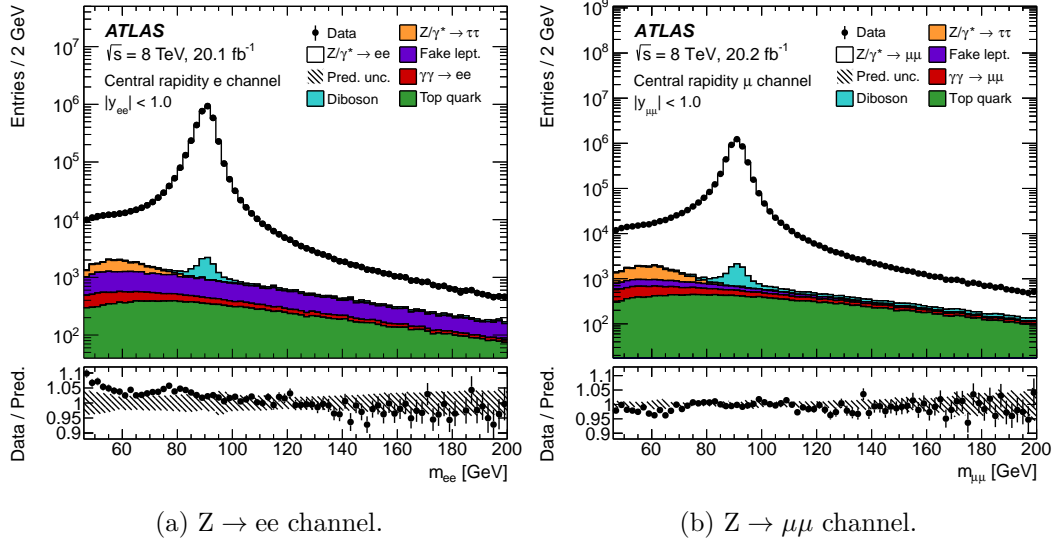


Figure 2.8.: Invariant mass spectra from Drell-Yan production for the central rapidity regions where $|\eta_e| < 1.37$ and $1.52 < |\eta_e| < 2.4$, or $|\eta_\mu| < 2.4$ is required for every electron or muon [42]. The rapidity of the dilepton system has to fulfill $|y_{ll}| < 1.0$.

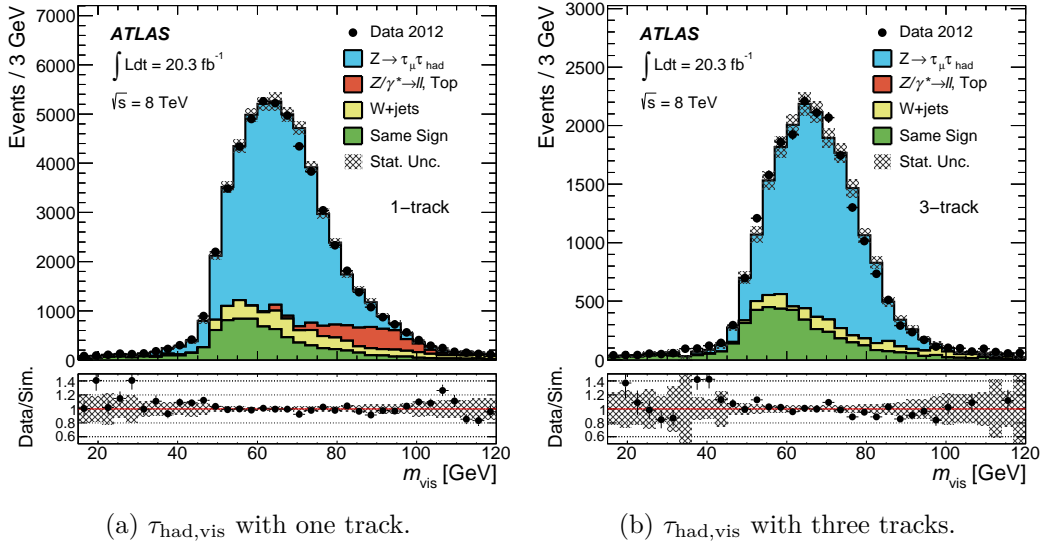


Figure 2.9.: Distributions of m_{vis} used for the calibration of the tau energy scale (TES) for hadronically decaying tau leptons with one or three associated tracks [46].

$M_P \approx 10 \times 10^{19}$ GeV, since at that point gravitational effects are expected to appear on the quantum level. Considering such large energies and masses, quantum loop corrections to the propagator of the Higgs boson lead to the so-called hierarchy problem. Here, the extra contributions to the mass of the Higgs boson diverge quadratically with the cut-off value. Therefore its bare mass, which cannot be calculated within the Standard Model, would have to be chosen with extreme precision in order to match the observed value of $m_h = 125$ GeV. Even though this is not an actual shortfall of the Standard Model, this large amount of fine-tuning seems worrisome for theories beyond the Standard Model that might be able to predict the bare Higgs mass.

The Randall-Sundrum (RS) model [14], proposed in 1999, presents an elegant solution to the hierarchy problem. It is one of many theories that suggests the existence of hidden space-like dimensions in order to incorporate gravity into the realm of particle physics, i. e. to bring together general relativity and the Standard Model on a fundamental level. In fact, the first theories that introduced an additional fifth dimension to the (3+1)-dimensional Minkowski space were already formulated in the 1920s by Theodor Kaluza and Oskar Klein. Here, the extra dimension is compactified on a circle and its characteristic length scale is thereby given by the radius R of the latter. Further refinements of the original proposals lead to the so-called ADD model [47], which is the first in the series of Kaluza-Klein related theories that is connected to the hierarchy problem. In this scenario, the fields of the Standard Model are confined to the apparent four-dimensional space, whilst gravity also propagates in multiple extra dimensions. Since it still is very difficult to probe Newton's law of gravity below the millimeter scale, they could be as large as $R \approx 1$ mm without contradicting current observations. Indeed, this size is needed in order to 'dilute' gravity, which might actually be of the order of the electroweak scale, down to the Planck scale. Unfortunately, this explanation is still not very satisfying as it only translates the hierarchy problem to the discrepancy between the predicted and expected size of the additional dimensions, i. e. $R \approx 1$ mm and $R \approx 1 \times 10^{-35}$ m (corresponding to the Planck length) respectively.

At this point the RS model demonstrates its strength since it solves the hierarchy problem but requires only a very modest tuning of its input parameters. The model suggests only one extra dimension that is compactified on a circle with radius R . Its coordinate shall be denoted as y in the following. At two fixed points, e. g. at $y = 0$ and $y = \pi R$, the extra dimension has two Minkowski-like four-dimensional worlds, called 3-branes, attached to it.

The model aims to solve the classical Einstein equations and is based on the non-factorizable metric

$$ds^2 = e^{-2k|y|} \eta_{\mu\nu} dx^\mu dx^\nu + dy^2, \quad (2.17)$$

where k is a free parameter and $\eta_{\mu\nu}$ denotes the Minkowski metric. The factor $e^{-2k|y|}$, called 'warp' factor, is responsible for a hierarchy between the two 3-branes. Here, the matter fields are not only constrained to the (3+1)-dimensional space,

2. Theoretical Framework

but reside on one of the 3-branes, termed TeV brane, only. The Higgs field and its vacuum expectation value get 'warped down' from the Planck scale on the other brane down to $v \approx 236$ GeV by $e^{-2k\pi R}$ if kR is chosen appropriately. Again, so far this is yet another reformulation of the hierarchy problem. The actual reduction in the amount of tuning happens within the Goldberger-Wise mechanism [48]. It completes the RS model by addressing an issue that has not yet been discussed: the stabilization of the compactified extra dimension. Since the laws of physics and the fundamental constants are to remain unaltered over time, this is an absolutely vital part of the theory. The Goldberger-Wise mechanism implements a scalar field in the five-dimensional bulk that is enclosed by the 3-branes. The potential of this field then stabilizes R and sets kR to the required value, whilst only a modest amount of tuning on the cosmological constant is needed. Randall and Sundrum have also proposed an alternative based on their original work, which is commonly referred to as the RS2 model [15]. In the limit $R \rightarrow \infty$ the extra dimension becomes infinite and only one of the two 3-branes remains.

Aside from solving the hierarchy problem, the RS model is also appealing from an experimental viewpoint. This is because the Kaluza-Klein gravitational modes obtain masses and mass splittings on the TeV scale, which makes their resonances detectable even at present colliders. At the LHC, the production would occur via quark- or gluon-fusion, their relative importance depending on the choice between the RS1 and the RS bulk model and the mass of the Kaluza-Klein mode [49]. The predicted branching fractions are summarized in 2.10. Since the di-jet production in the RS1 scenario is difficult to handle experimentally, the di-boson decay is the 'golden' channel in the graviton search at the LHC [50, 51].

This thesis is motivated by the coupling of the Kaluza-Klein gravitons to two SM-like Higgs bosons, in particular by the case where the latter further decay to a $\tau\bar{\tau}$ - and a $b\bar{b}$ -pair. Although this channel is not expected to appear as often as the di-boson channel or the $b\bar{b}b\bar{b}$ final state, it provides an interesting signature due to the two tau leptons.

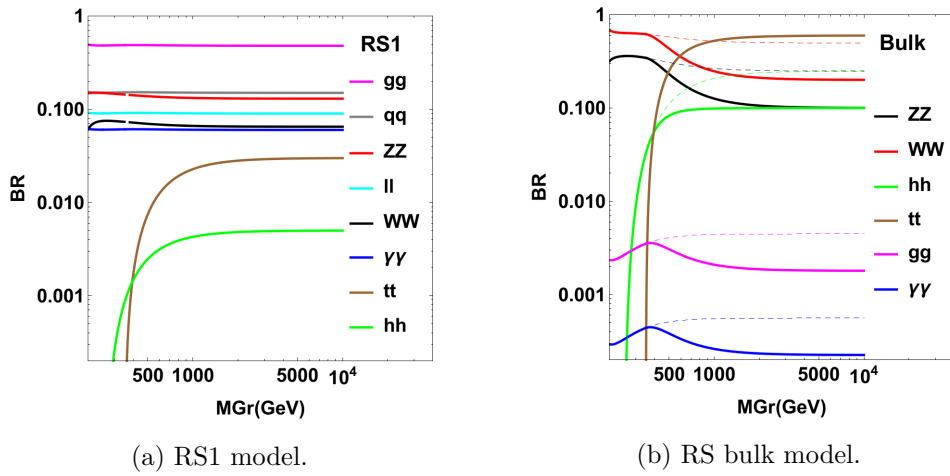


Figure 2.10.: Branching fractions for Kaluza-Klein gravitons in the RS1 and bulk model [49]. The letters q and l represent the sum of the light quarks (u,d,s,c,b) and three generations of leptons or neutrinos respectively. The dashed lines in 2.10b ignore the coupling to top quarks.

3. The LHC and the ATLAS Detector

3.1. The LHC

The Large Hadron Collider (LHC) [52, 53], which is predominantly used for proton-proton (pp) collisions, is the most powerful particle accelerator that has been built to date. It was designed to probe the Standard Model and search for new physics beyond it. With the confirmation of the Higgs boson in 2012 [12, 13] and the ongoing determination of its properties, it has already conducted a major scientific discovery.

The LHC is located at CERN's ¹ accelerator complex in Geneva near the border between France and Switzerland. It is installed in a tunnel with a circumference of about 27 km and hosts four major detector experiments, i. e. ATLAS [54], CMS [55], LHCb [56] and ALICE [57] (see figure 3.1). Whilst LHCb precisely measures the parameters of CP violation in B hadron decays and ALICE is dedicated mostly to heavy-ion collisions (such as Pb-Pb), ATLAS and CMS were designed to serve as multi-purpose experiments.

The storage ring itself houses a complex system of about 9600 multi-pole magnets in order to accelerate, direct, focus and clean the fillings. Except for the actual interaction points, the two beam lines of the LHC are kept in separate vacuum chambers that pass through the magnets' twin-apertures. The maximum beam energy is set by the 15 m long superconducting main dipole magnets that are used to bend the particles trajectories. They are cooled down to 1.9 K with the help of superfluid helium and are able to generate a magnetic field of 8.3 T.

In pp operation, the protons are taken from atoms of gaseous hydrogen that have their electron stripped off. They pass through a series of pre-accelerators before they are injected into the beam pipes. Circling either clockwise or counter-clockwise, bunches of $\approx 10^{11}$ protons are brought to collision at up to $\sqrt{s} = 13$ TeV before they eventually enter the beam dump after a turnaround of several hours. The mean number of events that correspond to a certain physics process with a cross section σ is given by

$$N = \int L \sigma dt, \quad (3.1)$$

where the dependence on the parameters of the accelerator ² has been combined into the instantaneous luminosity L , typically of order 10^{33-34} cm⁻¹ s⁻². Aside from the relevant events, signatures from other pp collisions in the same or nearby bunch

¹European Organization for Nuclear Research.

²This includes for example the beam profile, the filling scheme, the revolution frequency and the angle and transverse offset at the interaction point.

crossings, called in-time and out-of-time pile-up respectively, or even remnants from the same pp interaction (underlying event) form an important background.

The operation schedule of the LHC alternates periods of data-taking with annual and long-term breaks necessary for maintenance and upgrade work. After ramping up the beam energy to $\sqrt{s} = 8$ TeV in Run 1 (2009–2013) and the first long shutdown (2013–2015), the LHC currently is in the last month of Run 2 (2015–2018). This completes four highly successful years of pp running at almost its design centre-of-mass energy of 14 TeV and an integrated luminosity of about 80 fb^{-1} (2015–2017) already available for physics analysis.

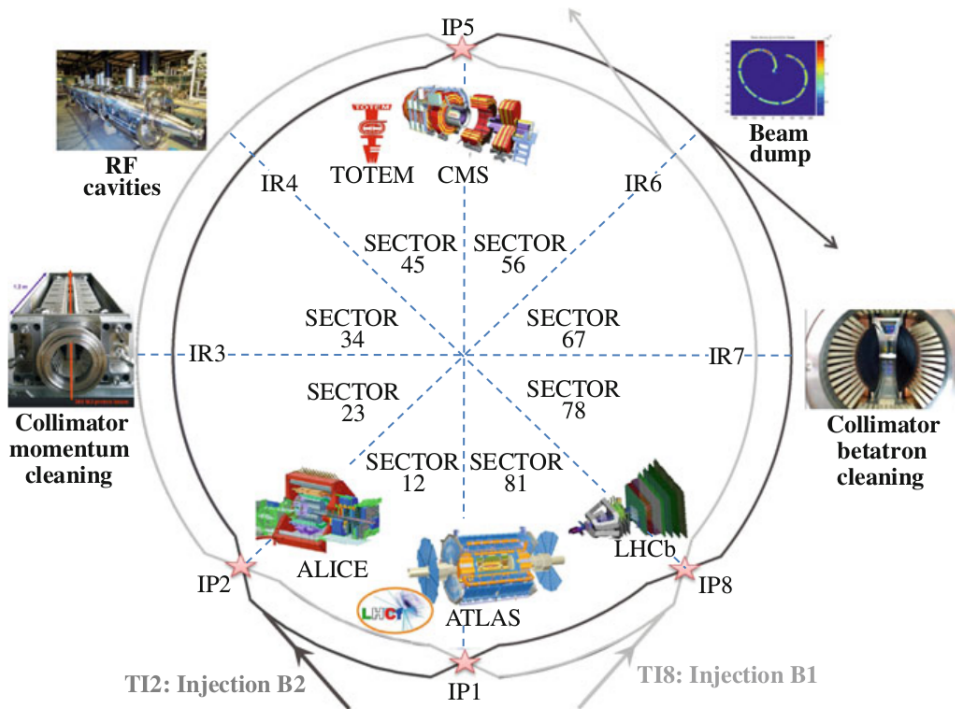


Figure 3.1.: Layout of the LHC with eight arcs, eight straight sections called ‘insertion regions’ (IRs), the interaction points (IPs) and the four main experiments [58].

3.2. The ATLAS Detector

The ATLAS detector [54] is the largest of the LHC’s experiments with a cylindrical shape of about 44 m in length, 25 m in diameter and a total weight of 7000 t (see figure 3.2). It collects and reconstructs the final state particles from the pp interactions that take place in its centre. Various subsystems, which are arranged in layers

3. The LHC and the ATLAS Detector

around the collision point, are employed in order to identify the outgoing particles and determine their properties, e. g. their type, charge and momentum.

Since the detector has a forward-backward and a cylindrical symmetry, a special coordinate system that originates in the collision point and suits this geometry is commonly adopted. Assuming a right-handed cartesian system where the x-axis points towards the centre of the LHC, the y-axis points upwards and the z-axis is aligned with the beam pipe, the ATLAS coordinate system is defined by the azimuthal angle ϕ in the transverse x-y-plane starting from the positive x-axis and the polar angle θ . The latter is most often reported in terms of the pseudorapidity ³

$$\eta = -\ln \left[\tan \left(\frac{\theta}{2} \right) \right] \quad (3.2)$$

with $\eta = 0$ for the transverse plane and $\pm\eta \rightarrow \infty$ along the beam axis. This coordinate is particularly useful at hadron colliders because the longitudinal momenta of the incoming partons are unknown and for massless particles differences in η are invariant under Lorentz boosts along the z-axis. From ϕ and η a distance measure

$$\Delta R = \sqrt{(\Delta\phi)^2 + (\Delta\eta)^2} \quad (3.3)$$

can be deduced. In addition, most analysis state quantities with respect to the x-y-plane, for example the transverse momentum p_T . As neutrinos pass through the whole detector with almost no interaction, the negative sum $E_{T,\text{miss}}$ of all transverse energy deposits is used to estimate their energy.

This thesis studies both the hadronic and leptonic decay modes of tau leptons as explained in section 2.2, therefore all four major components of ATLAS, i. e. the inner detector, the calorimeters, the muon chambers and the trigger system play an important role in the reconstruction chain.

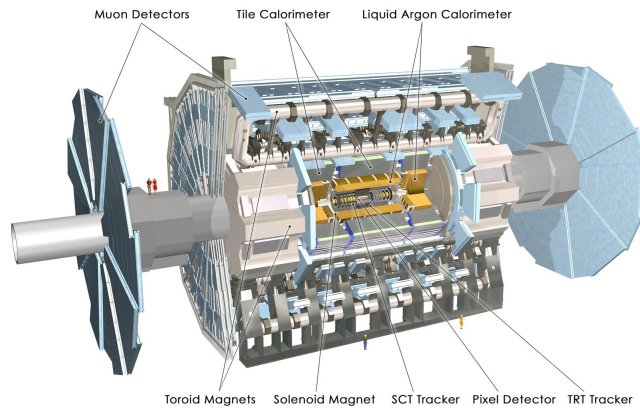


Figure 3.2.: Computer-generated image of the ATLAS detector [59].

³For highly relativistic particles, the pseudorapidity is a very good approximation of the rapidity $y = \frac{1}{2} \ln \left(\frac{E+p_z}{E-p_z} \right)$.

3.2.1. The Inner Detector

The inner detector is situated in close proximity, i. e. a few centimetres, to the beam pipe. It is about 6 m long and extends to one metre in all directions perpendicular to the z-axis (see figure 3.3). Its main purpose is the precise measurement of the charged particles' trajectories. In order to do so, the sub-systems are equipped with a very high granularity and fast read-out electronics. All of the inner detector's components are immersed in a 2 T magnetic field generated by the central solenoid magnet, which allows for momentum and charge reconstruction from the curvature of the trajectories.

Moreover, it is possible to not only reconstruct the primary vertex of a hard scattering process, but also the location of secondary vertices with a finite displacement. This is important for the tagging of jets originating from B hadron decays [60] or other particles that have a measurable decay length, e. g. tau leptons.

The two innermost sub-detectors, the silicon pixel detector and the semi-conductor tracker (SCT), ensure both the track and vertex reconstruction up to $|\eta| < 2.5$. The pixel detector has about 80 million silicon pixels which are allocated on three coaxial cylindrical layers and six disks equally spread over two end-caps. It is surrounded by the SCT's four barrel layers and nine disks at each side, collectively holding six million silicon microstrip sensors. The track reconstruction is assisted by the transition radiation tracker (TRT), though its main purpose is the distinction between electrons and charged pions. It consists of straw-like polyamide drift tubes which are arranged parallel to the beam axis in the barrel region and radially in several end-cap wheels. The TRT only extends to $|\eta| < 2.0$.⁴

During the first long shutdown in 2013-2015 an additional fourth pixel layer, the Insertable B-Layer (IBL), was installed between a new smaller radius beam pipe and the pixel detector [61]. This upgrade maintains the b tagging performance, even when the pre-existing innermost pixel layer (B-Layer) has suffered from radiation damage in the harsh environments of Run 2 and future data-taking periods.

3.2.2. The Calorimeter System

The calorimeter system (see figure 3.4) measures the amount and position of energy deposits from electromagnetic and hadronic showers. Except for neutrinos and muons, all particles are stopped in its two sub-systems, i. e. the liquid argon (LAr) or the tile calorimeter.

The LAr calorimeter [63, 64] accommodates three cryostates, one for the electromagnetic barrel ($|\eta| < 1.475$) and two encasing an electromagnetic end-cap (EMEC) ($1.375 < |\eta| < 3.2$), an hadronic end-cap (HEC) ($1.5 < |\eta| < 3.2$) and a forward calorimeter (FCal) ($3.2 < |\eta| < 4.9$) each. All of them use liquid argon as the active material, only the choice of absorber differs for the barrel and EM end-caps (lead),

⁴The intrinsic resolutions of the sub-detectors amount to $10 \times 115 \mu\text{m}^2$ in $(R-\phi) \times z$ or $(R-\phi) \times R$ coordinates for the pixel detectors' barrel and end-cap regions, similarly to $17 \times 580 \mu\text{m}^2$ for the SCT and to $130 \mu\text{m}$ for the TRT.

3. The LHC and the ATLAS Detector

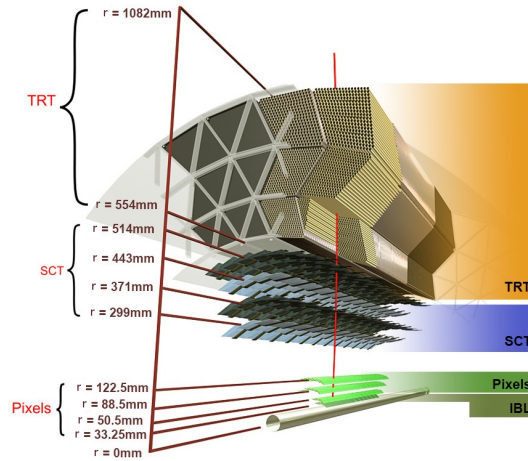


Figure 3.3.: Computer-generated image of the inner detector of ATLAS [62].

the HEC modules (copper) and the FCals (copper/tungsten). The overlap between the barrel and the end-caps at $\eta \approx 1.4$ is often referred to as the ‘crack’ region and needs to be treated cautiously, e. g. considering the reconstruction of electrons.

The tile calorimeter [65] encompasses the LAr systems and is divided into a barrel ($|\eta| < 1.0$) and two extended barrel ($0.8 < |\eta| < 1.7$) parts. They are constructed from wedge-like structures of alternating scintillator tiles and steel absorbers.

All in all, the calorimeters provide both an electromagnetic and hadronic coverage up to very high pseudorapidity values ($|\eta| < 4.9$).

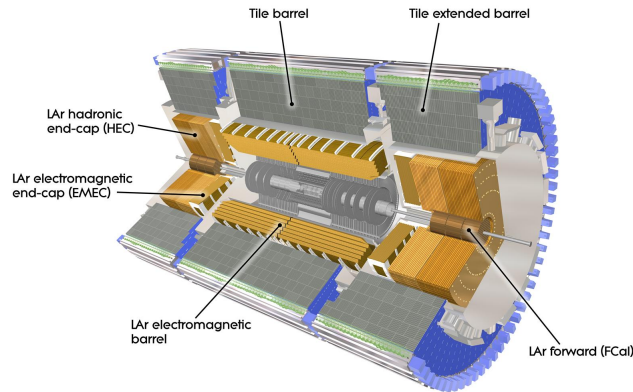


Figure 3.4.: Calorimeter system of the ATLAS detector [66].

3.2.3. The Muon Spectrometer

The muon spectrometer [67] is the outermost and most spacious sub-system of ATLAS (see figure 3.5). Its chambers are located on three concentric layers at radii

of 5 m, 7.5 m and 10 m in the barrel region and four wheels at each side of the interaction point ($|z| = 7$ m, 11 m, 14 m and 21 – 23m).

The sub-detector was designed to be a stand-alone tracking system for muons. Much like the inner detector, it is therefore suffused with a magnetic field generated by air-core magnets in one barrel and two end-cap toroids. Two sub-systems are employed in order to guarantee a precise tracking and a separate trigger capability.

In the barrel and end-cap regions respectively, resistive plate chambers (RPCs) ($|\eta| < 1.05$) and thin gap chambers (TGCs) ($1.05 < |\eta| < 2.4$) form the trigger system. They are able to detect muon hits fast enough to identify the corresponding bunch crossing and measure their η and ϕ coordinates.

The precise tracking is realised by monitored drift tubes (MDTs) ($|\eta| < 2.7$) and cathode strip chambers (CSCs) ($2.0 < |\eta| < 2.7$) with a higher granularity in the forward directions. The MDTs are only η -sensitive in the so-called ‘bending’ plane, thus their spatial information needs to be complemented by the trigger chambers.

On its own, the muon spectrometer can record muons above a momentum threshold of a few GeV ⁵ and achieve resolutions better than 3% across a wide p_T -range and about 10% for $p_T \approx 1$ TeV.

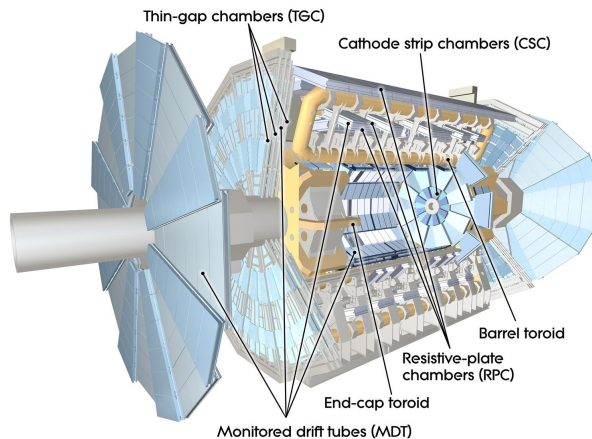


Figure 3.5.: Muon subsystem of the ATLAS detector [68].

3.2.4. The Trigger System

The enormous data flow generated by the sub-detectors in sections 3.2.1, 3.2.2 and 3.2.3 has to be reduced to a rate which is acceptable for processing and storage. Given this consideration, the ATLAS trigger system lowers the initial 40 MHz bunch crossing rate down to a few hundred Hz and circa one GB s⁻¹ for recording.

Since Run 2, the online selection gets conducted by an upgraded system with two stages [69]. Its focus lies on reconstructed physics objects (e. g. electrons, muons, tau

⁵The lower bound is mainly implied by the small energy loss in the calorimeter.

3. *The LHC and the ATLAS Detector*

leptons or jets) passing a certain momentum threshold. To start with, coarse information from the calorimeter and muon spectrometer is collected by the hardware-based Level-1 (L1) trigger and relevant events are picked by calculating basic event quantities (such as $E_{T,\text{miss}}$ or m_{inv}). Secondly, a software-based high-level trigger (HLT) can make more sophisticated decisions based on algorithms similar to those used in the offline reconstruction.

4. Reconstruction and Identification of High-Level Objects at ATLAS

At ATLAS, reconstructed high-level physics objects, such as electrons (see section 4.1), muons (see section 4.2), jets (see section 4.3), taus (see section 4.4) and $E_{T,\text{miss}}$ (see section 4.5), are the starting point for every analysis. In successive steps, they are assembled from low-level objects, including tracks [62] and vertices [70] from the inner detector and clusters of energy deposits in the calorimeter [71].

Since in most environments only very few reconstructed signatures correspond to a true particle of the desired type, every particle algorithm makes use of an individual identification step in order to discard events from background processes. Unless stated otherwise, the terminology that describes the performance of the reconstruction and identification algorithms is as follows: The reconstruction efficiency is the number of reconstructed particles that match to a simulated particle, called truth-matched in the following, divided by the total amount of simulated particles in the corresponding sample, the identification efficiency is computed with respect to particles that have already been reconstructed and the background rejection is defined as the inverse background efficiency.

4.1. Electrons

Electrons are reconstructed in three successive steps [72]: Firstly, fixed-size clusters in the EM calorimeter are formed from seeds provided by a sliding window algorithm [71]. For the central region ($|\eta| < 2.47$) the seeds are composed of 3×5 longitudinal towers in $(\eta-\phi)$ -space exceeding a total transverse energy of 2.5 GeV summed over all layers of the calorimeter and with a size of $\Delta\eta \times \Delta\phi = 0.075 \times 0.125$.¹ Secondly, track candidates from the inner detector are $(\eta-\phi)$ -associated to the clusters in the calorimeter and refitted to account for energy losses due to bremsstrahlung [73]. A preferred track is singled out by a classification according to the ΔR -matching and the amount and quality of pixel, SCT and TRT hits. The electron candidate then must pass a final criterium, i. e. be compatible to the primary vertex with the highest sum of squared transverse track momenta. In more detail, this selection applies cuts on the distance of closest approach in the transverse plane, d_0 , between the track and the beam line (the so-called impact parameter) with uncertainty σ_0 ($\frac{d_0}{\sigma_0} < 5$), the corresponding longitudinal distance Δz_0 and the polar angle θ of the

¹This granularity corresponds to a grid with $N_\eta \times N_\phi = 200 \times 256$ elements of size $\Delta\eta \times \Delta\phi = 0.025 \times 0.025$ overlaying the EM barrel and end-caps.

4. Reconstruction and Identification of High-Level Objects at ATLAS

track ($\Delta z_0 \sin \theta < 0.5$ mm). The combined information of the selected track and the calibrated [74] calorimeter cluster enters the calculation of the electron's four-momentum. Throughout this process, photons can be distinguished from electrons since they produce either no track at all or conversion tracks ($\gamma \rightarrow e^+e^-$) that stem from a mass-vetoed secondary vertex within the inner detector.

The electron identification effectively separates prompt electrons, e.g. produced via W,Z exchange or decays of J/ψ mesons ² from background events, i.e. semi-leptonic heavy flavour decays, photon conversions and most importantly fake candidates from hadronic jets (see section 4.3). The distinction is drawn by a likelihood-based discriminator which uses the shape and magnitude of the EM shower in the calorimeter, the quality of the track and the track-cluster matching as well as the amount of transition radiation in the TRT as input variables. It is optimized in bins of $|\eta|$ and E_T and provides three working points, i.e. Loose, Medium and Tight, in order of increasing background rejection and decreasing identification efficiency.

4.2. Muons

The reconstruction of muons employs four algorithms that combine the information from the calorimeters and from tracking procedures that happen independently in the muon spectrometer and the inner detector [76]. In the muon spectrometer, a track is put together by a combinatorial search seeded by segments of hits in various layers of the MDTs and CSCs. Combined muons are built from a global fit of hits in the inner detector and the muon chambers that is initiated by a reconstructed muon in either of the sub-detectors, but primarily in the muon spectrometer. The segment-tagged category requires only one segment apart from a track in the inner detector, thus collecting muons with a low p_T and in low-acceptance regions in the muon spectrometer. Calorimeter-tagged muons compensate for the service and cabling gap in the central region of the muon chambers ($|\eta| < 0.1$) since they only ask for an inner detector track and a muon-like energy deposit in the calorimeter. Muons that are reconstructed in the spectrometer alone and loosely extrapolated to the interaction point are useful when no tracking can be provided by the inner detector ($|\eta| > 2.5$). Candidates that are obtained from the combined approach are the largest and most important category, while segment-tagged, calorimeter-tagged and extrapolated muons are mostly a means of recovering acceptance in certain regions of the detector.

The muon identification is optimized in order to discriminate prompt muons, e.g. from W, Z or J/ψ decays, against the most frequent background events, i.e. charged pions and kaons decaying inside the inner detector. For combined muons, a cut-based selection exploits the fact that the in-flight light hadron decays produce a kinked trajectory and hence a poor global track fit and momentum disagreement between the muon spectrometer and inner detector. Quality cuts on the tracks from both

²Both prompt J/ψ mesons and those produced by B hadron decays are considered [75], though the former create electrons that are more signal-like to most analysis.

sub-systems are applied in all categories to ensure a high momentum resolution. Four working points targeting specific analysis needs are provided. They employ distinctive pickings from the four reconstruction algorithms and cuts on the combined muon identification variables. The loose criteria maximise the reconstruction efficiency, the tight selection has the highest purity, the medium working point minimises the systematic uncertainties and a high- p_T tuning puts emphasis on a good momentum resolution for muons with $p_T > 100$ GeV.

4.3. Jets

Jets are the conventional tool for handling the deposits from hadronic showers after the fragmentation and hadronization of partons due to the confinement of QCD. At ATLAS, jets are predominantly assembled using a sub-class of the sequential clustering algorithms [77], including the k_T , Cambridge/Aachen and anti- k_t methods [78]. For all of them, topological clusters built from calorimeter cells [79] serve as the initial inputs. They in turn are constructed by a seed-and-collect mechanism that groups neighbouring cells according to their signal significance, i. e. the ratio between the energy deposit and the expected noise [79]. As opposed to those obtained from the sliding window method for the reconstruction of electrons (see section 4.1), topological clusters hence possess a variable size.

To begin with, the distances between any two entities (d_{ij}) or an entity and the beam pipe (d_{iB}) are calculated. Gradually, objects are either merged or classified as a jet and removed from the process until none are left, depending on whether a d_{ij} or a d_{iB} yields the smallest value in the current step.

The definitions of the distances

$$d_{ij} = \min(p_{T,i}^{2p}, p_{T,j}^{2p}) \frac{\Delta R_{ij}^2}{R^2} \quad (4.1)$$

$$d_{iB} = p_{T,i}^{2p} \quad (4.2)$$

are characteristic for each algorithm in the sense that the choice of the parameter p ($p = 1$, $p = 0$ and $p = -1$ for the k_T , Cambridge/Aachen and anti- k_t clustering respectively) defines the relative importance between the momentum and geometrical scale. The minimal distance between two jets is given by the parameter R . For most purposes, jets at ATLAS are reconstructed as anti- k_t recombinations, for instance in jet performance studies [80], the tau reconstruction (see section 4.4) and the boosted di-tau algorithms (see chapter 5). Even though it is sequentially clustered, an anti- k_t jet is ideally cone-shaped which makes it comparatively easy to subtract a uniform background, e. g. from pile-up.

4.4. Taus

The tau reconstruction [46] gathers its visible hadronic decay products³, which typically have a collimation that is sufficient to justify an anti- k_t jet seed with $R = 0.4$. Additionally, the seed is required to have $p_T > 10$ GeV, $|\eta| < 2.5$ in accordance with the tracker and, for most analysis and performance evaluations [81], to lie outside the transition region of the calorimeter ($1.37 < |\eta| < 1.52$). The candidate is further subdivided into a core cone for the primary tau signature ($\Delta R < 0.2$) and an isolation region ($0.2 < \Delta R < 0.4$) that only shows a high occupation for mistakenly reconstructed QCD activity. For taus with $p_T < 50$ GeV and events with many reconstructed primary vertices, the vertex with the highest $\sum p_{T,\text{tracks}}^2$ favoured by the ATLAS default (see section 4.1) is not necessarily the one the tau originates from. Thus the tau vertex is chosen by a dedicated algorithm, selecting the primary vertex with the highest fraction of the p_T sum taken from all tracks in the core region that meet minimal quality criteria, i. e. $p_T > 1$ GeV, at least two pixel hits and in total more than six hits in the pixel detector and SCT.

All tracks within $\Delta R < 0.4$ with respect to the axis given by the jet seed and the tau vertex enter a BDT-based classification scheme that knows of four categories: tau tracks from charged hadrons (mainly from decays into π^\pm and inside the core cone), conversion tracks (e. g. from conversions as a result of $\pi^0 \rightarrow \gamma\gamma$ decays), isolation tracks (primarily from underlying event and in the isolation region) and a fake collection for the remaining tracks (dominated by pile-up contributions). Only taus with one or three associated tracks from the tau tracks, commonly termed ‘1-prong’ and ‘3-prong’, are forwarded to the identification.

The main background contamination in the reconstruction arises from quark- or gluon-initiated QCD jets, hence the identification is trained accordingly. Two BDTs handle the tau candidates with either one or three associated tracks independently. A detailed list of all identification variables can be found in [81]. They are corrected for the mean number of interactions per bunch-crossing μ , and the values of the output BDT score are chosen as a function of p_T in order to obtain flat signal efficiencies, i. e. for the reconstruction and identification combined, in both μ and p_T . Three working points, Loose, Medium and Tight, with target signal efficiencies of 60 %, 55 % and 45 % for 1-prong taus and 50 %, 40 % and 30 % for 3-prong taus are provided. While muons very rarely fake hadronically decaying taus due to their small energy deposit in the calorimeter, electrons pose a significant background for 1-prong taus. To obtain a corresponding electron veto, the electron likelihood discriminator is exploited. A dedicated very loose working point, which is tuned to 95 % efficiency for loose taus, is offered by the electron identification and used to reject reconstructed taus matched to a very loose electron within $\Delta R < 0.4$.

³They will be referred to as τ_{had} for the remainder of this thesis.

4.5. Missing Transverse Energy

Reconstructing the missing transverse energy, $E_{T,\text{miss}}$ [82], is a challenging task, since it relies on all sub-systems of the ATLAS detector and the quality of the physics objects discussed in the previous sections. It is computed from the sum of the p_T of fully calibrated electrons, photons, hadronically decaying taus, muons and jets as well as a term that takes into account any soft charged particles. The soft term collects the p_T of ID tracks that pass quality cuts, originate from the default primary vertex and are not associated to any particle or jet. Thus, the reconstructed $E_{T,\text{miss}}$ is largely robust with regard to pile-up. As physics objects are reconstructed independently, e. g. such that every τ_{had} entails an anti- k_t ($R = 0.4$) jet, the hard contributions are prioritized and refined overlap removal strategies are employed in order to prevent double countings.

5. Reconstruction and Identification of Boosted Di-Taus

The development of dedicated reconstruction and identification chains for boosted di-tau decays is motivated by the shortfalls of the standard tau techniques in this regime. The issues that arise are specific for the three di-tau decay modes.

For $\tau_{\text{had}}\tau_{\text{had}}$ di-taus the inefficiencies appear as early as on the reconstruction level since the two anti- $k_t(R = 0.4)$ seed jets merge when the spatial separation between the two tau decays becomes very low, i. e. for $\Delta R < 0.4$ (see figure 5.1) [16].

Regarding the semi-leptonic modes [17], the standard τ_{had} reconstruction performs almost fully efficient, even with a close by muon or electron (see figure 5.2 and 5.3) ¹. However, because of the nearby energy deposits of the electron, for $\tau_{\text{had}}\tau_e$ di-tau decays the direction of the reconstructed τ_{had} candidate is drastically changed with respect to the simulated hadronic tau decay, and thus a poor momentum reconstruction results. The identification breaks down below $\Delta R = 0.4$ for both $\tau_{\text{had}}\tau_e$ and $\tau_{\text{had}}\tau_\mu$ di-taus. In the $\tau_{\text{had}}\tau_e$ channel this happens because of the high sensitivity of the identification on the track provided by the electron and its energy deposit leaking into the τ_{had} candidate. In case of $\tau_{\text{had}}\tau_\mu$ decays only the additional track from the muon in the inner detector has a significant impact on the identification variables.

The electron algorithms perform reasonably well for $\Delta R > 0.2$ before the track-cluster matching in the electron reconstruction and its identification variables suffer from the τ_{had} 's energy deposits. Muons are reconstructed and identified almost independently of an overlapping τ_{had} .

The multi-TeV graviton samples that have been used for these studies show significantly different kinematics than the usual $Z \rightarrow \tau\tau$, $Z \rightarrow ee$ and $Z \rightarrow \mu\mu$ events employed in single tau, electron and muon performance evaluations. In particular, for $p_T(\tau) > 100$ GeV this leads to a significant amount of tau decays with secondary vertices that lie behind the first pixel layers [83]. Though neither the electron nor the muon algorithms are optimized for displaced secondary vertices, this especially poses an issue for the latter, since its identification has been trained against in-flight decays of light hadrons.

Details on the di-tau algorithms, which are briefly summarized in the following, can be found in [16] for fully-hadronic decays and [17] for the semi-leptonic

¹This is partly due to the definition of the reconstruction and identification efficiencies in figure 5.2 and 5.3. Here, a simulated τ_{had} candidate is categorized as reconstructed or identified when it matches to an anti- $k_t(R = 0.4)$ jet within $\Delta R < 0.4$ with no requirement on the number of associated tau tracks.

modes. They are not only meant to extend the standard tau reconstruction and identification below $\Delta R = 0.4$, but also allow for cross-checks and improvements for $0.4 < \Delta R < 1.0$.

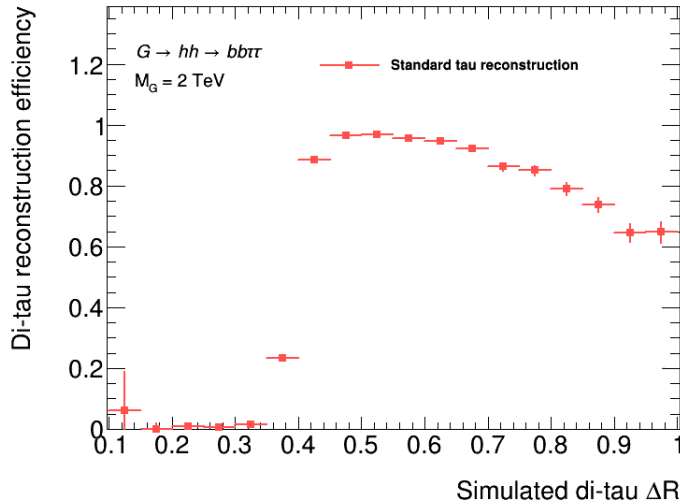


Figure 5.1.: Reconstruction efficiency for $\tau_{\text{had}}\tau_{\text{had}}$ based on the standard tau reconstruction as a function of their angular separation ΔR from $G \rightarrow hh \rightarrow bb\tau\tau$ samples with $M_G = 2$ TeV [16].

5.1. Fully-Hadronic Di-Tau Decays

The reconstruction of fully-hadronic di-tau decays is seeded by large anti- k_t ($R = 1.0$) jets with $p_T > 300$ GeV in order to contain the signatures from both τ_{had} decays and have them surrounded by a QCD discriminating isolation region. They are groomed for smaller anti- k_t subjets with $R = 0.2$ which are expected to match the energy deposits from the individual taus. The subjets with the highest and second-highest p_T are referred to as leading and subleading respectively. Primary and secondary vertices are assigned to each subjet as in the single tau reconstruction (see section 4.4). Tracks that pass impact parameter cuts, i.e. $d_0 < 1$ mm and $|z_0 \sin \theta| < 1.5$ mm (see section 4.1), in addition to the basic pile-up reduction cuts used in the vertex finding are associated to the whole di-tau seed jet and perhaps also to one of the subjets if they lie within the respective jet cones. A di-tau candidate needs to have at least two subjets with a minimum of one track and a maximum of four tracks, each, which provides a basic QCD reduction.

The identification uses a BDT which has been trained against QCD di-jet background from data. Its input variables exploit the distinct phenomenology of a QCD jet compared to a real di-tau, for example that it produces subjets with energy deposits and tracks which are less collimated, deposits most of its energy in the leading

5. Reconstruction and Identification of Boosted Di-Taus

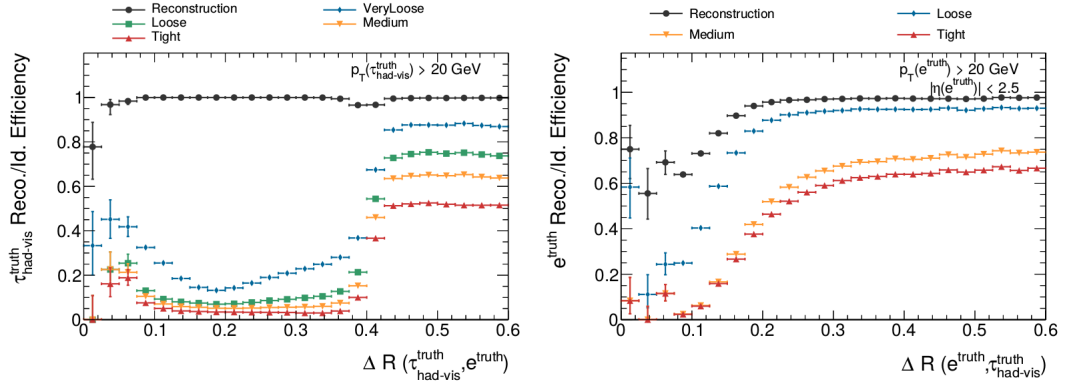


Figure 5.2.: Reconstruction and identification efficiencies for τ_{had} candidates close to a simulated electron based on the standard tau reconstruction and identification (left), reconstruction and identification efficiencies for electrons with a nearby simulated τ_{had} (right) - both obtained from $G \rightarrow hh \rightarrow \tau\tau\tau\tau$ samples with $M_G = 1\dots 5 \text{ GeV}$ [17].

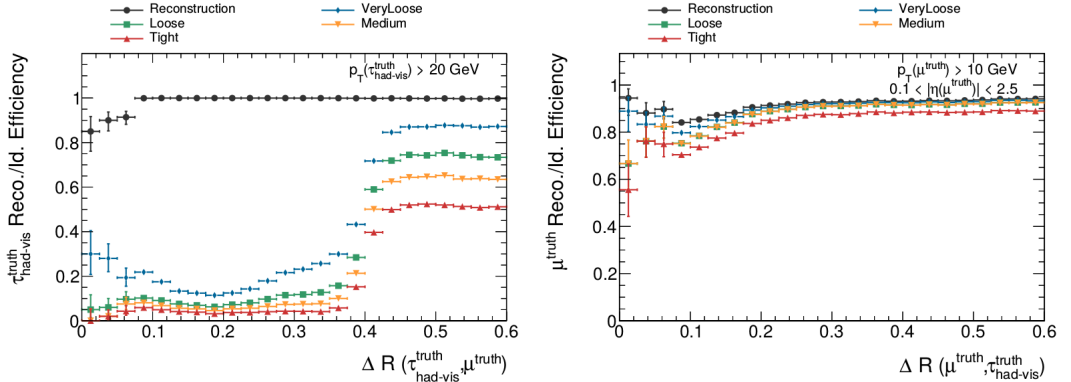


Figure 5.3.: Reconstruction and identification efficiencies for τ_{had} candidates close to a simulated muon based on the standard tau reconstruction and identification (left), reconstruction and identification efficiencies for muons with a nearby simulated τ_{had} (right) - both obtained from $G \rightarrow hh \rightarrow \tau\tau\tau\tau$ samples with $M_G = 1\dots 5 \text{ GeV}$ [17].

subject, distributes its energy more evenly amongst the subject-associated tracks and generates subjects that more often escape a clear 1- or 3-prong classification. A p_T - and μ -reweighting is applied on the training samples in order to obtain flat identification efficiencies in both variables. Four selections - very loose, loose, medium and tight - corresponding to lower cut values in the BDT score of 0.60, 0.65, 0.72, 0.77 and respective identification efficiencies of about 95 %, 90 %, 70 % and 30 % are available for usage in an analysis context.

5.2. Semi-Leptonic Di-tau Decays

5.2.1. Semi-Leptonic Decays with a Final State Electron

The reconstruction of $\tau_{\text{had}}\tau_e$ decays is seeded by anti- $k_t(R = 1.0)$ jets with $p_T > 300$ GeV, where the p_T requirement is a remnant from the objects of the fully-hadronic reconstruction it is based upon. They are filtered for anti- $k_t(R = 0.2)$ subjects exceeding $p_T = 15$ GeV to capture the τ_{had} signature and also searched for reconstructed electrons. Every combination of an electron and a subject with $\Delta R > 0.1$ is considered a $\tau_{\text{had}}\tau_e$ candidate. Tracks and primary vertices are associated to the seed jet and subjects as in the $\tau_{\text{had}}\tau_{\text{had}}$ case. When di-taus reconstructed from a simulated electron- τ_{had} system below $p_T = 300$ GeV are excluded, a high reconstruction efficiency of about 90 % down to $\Delta R(\tau_{\text{had}}^{\text{truth}}, e^{\text{truth}}) = 0.2$ is achieved.

Simulated $\tau_{\text{had}}\tau_e$ di-taus taken from $G \rightarrow hh \rightarrow 4\tau$ samples and data events with no pre-selection except for anti- $k_t(R = 1.0)$ jet triggers, thus dominated by QCD contributions, are handed to a BDT classifier for training and testing purposes. Di-tau candidates in the background sample are more abundant in the low- p_T regime and less frequent for higher p_T values. Therefore they are reweighted in bins of the p_T of the reconstructed electron and τ_{had} to prevent the BDT from being biased towards certain kinematic regions. Similar to the $\tau_{\text{had}}\tau_{\text{had}}$ identification, physically motivated variables that do not directly refer back to the candidate's kinematics are used to make the classifier independent of the di-tau production process. They focus on either the properties of the electron or τ_{had} candidates as well as on the entire anti- k_t jet area. A flattened BDT score with four lower threshold values, i. e. 0.05, 0.20, 0.35 and 0.50, which correspond to identification efficiencies of 95 %, 80 %, 65 % and 50 % and very loose, loose, medium and tight working points, is calculated. The flattening is deduced in bins of the p_T of the reconstructed electron and τ_{had} , effectively varying the initial BDT score cut with respect to the two variables and thereby ensuring p_T -independent identification efficiencies.

The dominant overlap with other di-tau modes that remains after the identification step is given by $\tau_{\text{had}}\tau_{\text{had}}$ decays, which may appear very similar to the BDT, e. g. due to the subject-related identification variables. An orthogonalization between the two di-tau decay channels can be achieved when further selections, for example regarding the kinematics of the electron and τ_{had} and the electron likelihood score, are considered.

5.2.2. Semi-Leptonic Decays with a Final State Muon

For $\tau_{\text{had}}\tau_{\mu}$ decays, the muon track is most often classified as a tau track that enters the identification of the τ_{had} candidate. Since the additional leptonic energy deposit in the calorimeter is negligible, in contrast to the $\tau_{\text{had}}\tau_e$ mode, removing the track of the muon and re-calculating the standard τ_{had} variables recovers its identification efficiency down to $\Delta R = 0.1$ with only slight losses due to the displaced secondary vertex of the tau (see figure A.3). Di-tau candidates which are built from every reconstructed τ_{had} -muon pair with $\Delta R < 1.0$ and propagated through the standard τ_{had} and muon classification therefore yield acceptable identification efficiencies.

An alternative approach which utilizes a novel BDT that operates on the di-tau candidates instead has also been tested. In terms of the input samples, the reweighting scheme and the working point tuning, its training follows the same procedure as for the $\tau_{\text{had}}\tau_e$ identification. In addition to the standard τ_{had} variables which have been corrected for the muon track, three variables describing the working point, isolation and energy loss of the muon are passed to the classifier.

When the results of the two methods are compared, their performance with regard to the identification efficiencies and background rejections is very similar. Although the output of the newly trained BDT yields background rejections which are about ten times larger, this comes at the cost of reduced identification efficiencies for di-taus with $p_T < 300$ GeV. Since this behaviour is beneficial to the $G \rightarrow hh \rightarrow bb\tau\tau$ analysis this strategy is pursued in the following chapters, albeit the approach based on the standard algorithms is more flexible and better suited to any analysis looking into a lower p_T -regime.

The only significant contribution from another di-tau decay channel which cannot easily be removed with a tight identification selection stems from the $\tau_e\tau_{\mu}$ mode, where an electron fakes the τ_{had} candidate. However, this overlap is far less significant than the $\tau_{\text{had}}\tau_{\text{had}}$ misclassification in the $\tau_{\text{had}}\tau_e$ channel.

5.3. Performance and Validation

The nominal efficiencies of the new reconstruction and identification for both the fully-hadronic and the semi-leptonic di-tau decay channels have been calculated throughout the development of the respective algorithms (see chapter A). With an actual application in a physics analysis in mind, their performance has to be evaluated in terms of the agreement between simulated Monte Carlo samples and data. In the next two chapters, two studies that approach this issue in their own way are presented. In chapter 6 the di-tau signal, taken from the $G \rightarrow hh \rightarrow 4\tau$ samples that have already been in use in section 5.2, is assumed to agree with data with no further scaling. According to this nominal selection, systematic uncertainties of the reconstruction and identification efficiencies as well as on the di-tau energy scale are extracted from $G \rightarrow hh \rightarrow 4\tau$ samples with various systematic variations that are considered in the simulation of the ATLAS detector. Since they have already been computed for the fully-hadronic channel [84], in this thesis only the results for

the semi-leptonic mode are discussed. The second approach of the boosted di-tau validation studies (see chapter 7) directly compares $Z \rightarrow \tau\tau(+\text{jets})$ events as a well-understood benchmark process from the Standard Model to data. In case of the fully-hadronic channel, scale factors on the identification efficiency are calculated, whereas due to technical limitations for the semi-leptonic modes only an outline of some first results is presented.

6. Systematic Uncertainties for Semi-Leptonic Di-Tau Decays

6.1. Graviton Samples with Systematic Variations

The systematic uncertainties that are presented in this chapter have been derived from $G_{\text{RS}}^{\text{bulk}} \rightarrow \text{hh} \rightarrow 4\tau$ Monte Carlo samples (see table B.1) with $M_G = 1\dots 5\text{TeV}$ and produced in conformity with the ATLAS simulation infrastructure [85]. Events generated with MadGraph5_aMC@NLO [86] at leading order were interfaced to Pythia8 [87] with the A14 tuning [88] and the NNPDF23LO PDF set [89] for parton shower modelling and EvtGen [90] for the simulation of heavy flavour decays. The ATLAS detector and its response were simulated with GEANT4 [91, 92].

Since the reconstruction and identification of boosted di-taus (see chapter 5) mainly depends on the tracking information from the inner detector and on the calorimeters, four $G_{\text{RS}}^{\text{bulk}} \rightarrow \text{hh} \rightarrow 4\tau$ samples that each take into account a specific modification of the detector in its simulation have been chosen accordingly. The ALT_GEO variation increases the overall material budget in all detector layers, the IBL_30 samples consider 30% more material in the IBL, PP0_50 simulates 50% more material in one of the patch panels (PP0) of the inner detector and in QGSP_BIC an alternative hadronic shower model is used. In contrast to the default one, i. e. QGSP_BERT, it applies the Binary cascade model instead of the Bertini cascade [93].

The $G_{\text{RS}}^{\text{bulk}} \rightarrow \text{hh} \rightarrow 4\tau$ samples contain about $2 \cdot 10^5$ and $1 \cdot 10^5$ events in each mass slice for $M_G = 1\dots 2.5\text{TeV}$ and $M_G = 3\dots 5\text{TeV}$, respectively (see table B.2). Since almost every event contains two simulated di-taus, in a total of approximately $1.5 \cdot 10^6$ events about $3 \cdot 10^6$ di-taus can be found, where the event numbers that correspond to the different branching fractions of the di-tau decay modes are listed in table 6.1.

The kinematics of the simulated semi-leptonic di-tau decays are depicted in figure 6.1. The p_T of the di-tau system, taken from the sum of the transverse momenta of the lepton¹ and the τ_{had} subjet, increases for higher graviton masses. In this regime, the high p_T of the Higgs boson leads to more collimated taus and hence to a lower spatial separation $\Delta R(\tau_{\text{had}}^{\text{truth}}, \ell^{\text{truth}})$ between their visible decay products. Considering the available graviton mass spectrum, $p_T(\text{di-tau}^{\text{truth}})$ and $\Delta R(\tau_{\text{had}}^{\text{truth}}, \ell^{\text{truth}})$ are anti-correlated and the best statistics are available for $0.2 < \Delta R(\tau_{\text{had}}^{\text{truth}}, \ell^{\text{truth}}) < 0.4$. Due to the neutrinos in both semi-leptonic channels, the peak of the visible mass at $m_{\text{vis}} \approx 50\text{GeV}$ lies well below the Higgs mass. The

¹In the following electron and muons are collectively referred to as leptons.

6.2. Systematic Uncertainties for the Reconstruction and Identification Efficiency

Table 6.1.: Branching fractions and number of events for the different di-tau decay channels, taken from $1.93 \cdot 10^5$ events in the nominal $G_{\text{RS}}^{\text{bulk}} \rightarrow \text{hh} \rightarrow 4\tau$ sample with $M_G = 1$ TeV.

Di-tau decay mode	Branching fraction	Number of events
$\tau_{\text{had}}\tau_{\text{had}}$	42.3 % ($\approx \frac{4}{9}$)	162300
$\tau_{\text{had}}\tau_{\text{e}}$	23.4 % ($\approx \frac{2}{9}$)	88900
$\tau_{\text{had}}\tau_{\mu}$	22.1 % ($\approx \frac{2}{9}$)	87300
$\tau_{\text{e}}\tau_{\mu}$	6.1 % ($\approx \frac{1}{18}$)	23600
$\tau_{\text{e}}\tau_{\text{e}}$	3.2 % ($\approx \frac{1}{36}$)	12200
$\tau_{\mu}\tau_{\mu}$	2.9 % ($\approx \frac{1}{36}$)	11700

p_{T} ratio between the leptons and the visible decay products of the hadronically decaying tau reflects the fact that the additional neutrino in the leptonic tau decay carries away a significant amount of transverse momentum.

6.2. Systematic Uncertainties for the Reconstruction and Identification Efficiency

In the following, both the reconstruction and the identification efficiencies are computed from truth-matched reconstructed di-taus with respect to all simulated di-taus for either of the two semi-leptonic channels. The relative uncertainties $\Delta\epsilon_{\text{tot}}$ on the two quantities are calculated individually for each systematically varied sample as

$$\Delta\epsilon_{\text{Variation}} = \frac{\epsilon_{\text{Nominal}} - \epsilon_{\text{Variation}}}{\epsilon_{\text{Nominal}}} \quad (6.1)$$

and then quadratically summed over all four modifications to yield

$$\Delta\epsilon_{\text{tot}} = \sqrt{\sum_{\text{Variations}} (\Delta\epsilon_{\text{Variation}})^2}. \quad (6.2)$$

They are provided in bins of $\Delta R(\tau_{\text{had}}^{\text{truth}}, \ell^{\text{truth}})$, $p_{\text{T}}(\tau_{\text{had}}^{\text{truth}})$ and $p_{\text{T}}(\ell^{\text{truth}})$ that represent different kinematic regions (see figure 6.2). The binning has been chosen in order to reflect the physical and technical boundaries of the di-tau reconstruction whilst providing sufficient statistics, i. e. at least a few hundred events passing the identification selection, in every region. The spatial separation $\Delta R(\tau_{\text{had}}^{\text{truth}}, \ell^{\text{truth}})$ is divided into three segments, labelled small, medium and large, as to where the highest di-tau population occurs ($0.2 < \Delta R < 0.4$), the two taus are highly collimated ($\Delta R < 0.2$) or where they are well separated ($0.4 < \Delta R < 1.0$) up to the anti- k_t ($R = 1.0$) seed jet limit. The low, medium and high $p_{\text{T}}(\tau_{\text{had}}^{\text{truth}})$ and $p_{\text{T}}(\ell^{\text{truth}})$ bins represent the very low p_{T} regime ($p_{\text{T}}(\tau_{\text{had}}^{\text{truth}}) < 20$ GeV or $p_{\text{T}}(\ell^{\text{truth}}) < 20$ GeV) and di-taus with either a moderate ($20 \text{ GeV} < p_{\text{T}}(\tau_{\text{had}}^{\text{truth}}) < 200$ GeV and $20 \text{ GeV} < p_{\text{T}}(\ell^{\text{truth}}) < 100$ GeV) or

6. Systematic Uncertainties for Semi-Leptonic Di-Tau Decays

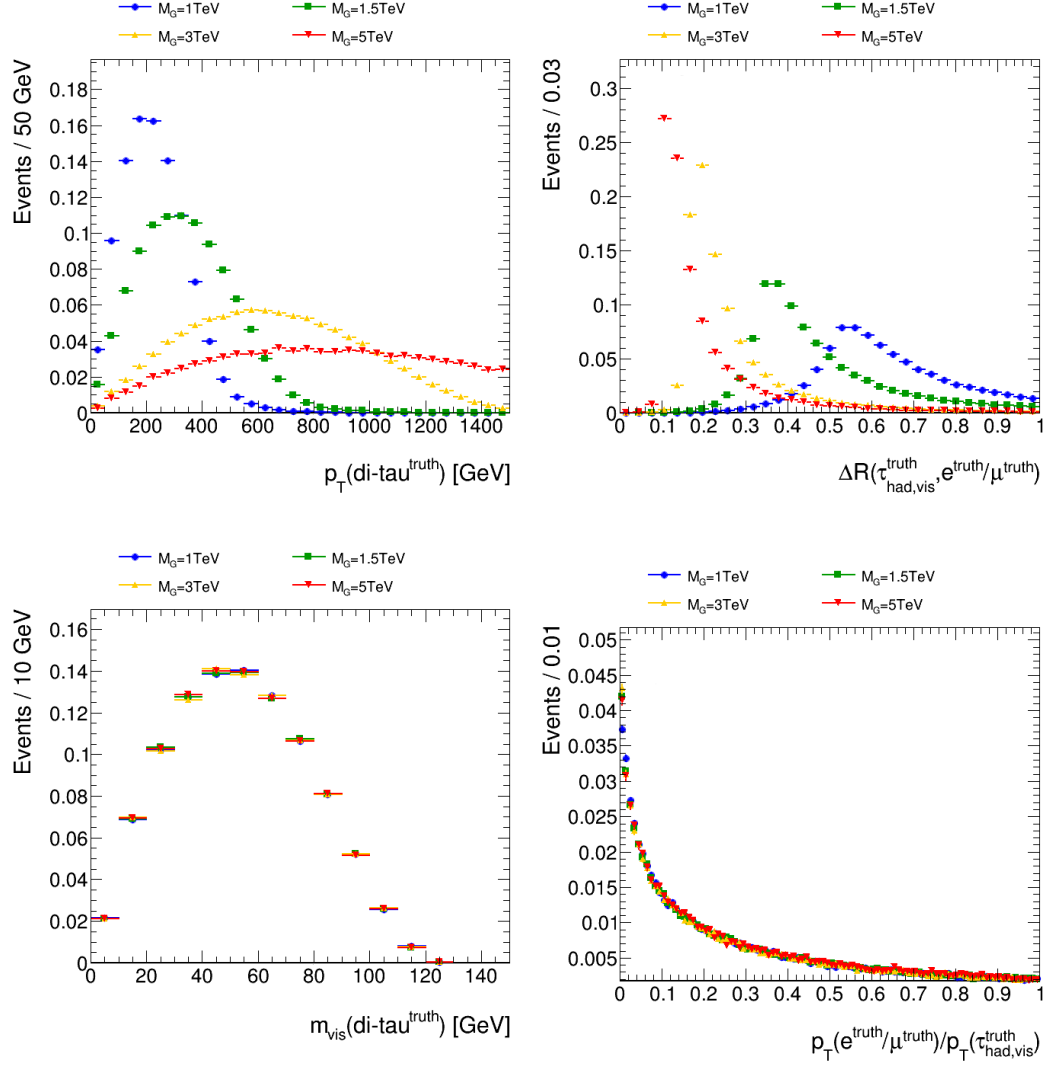


Figure 6.1.: Normalized distributions of the kinematics of simulated di-taus from $G_{\text{RS}}^{\text{bulk}} \rightarrow hh \rightarrow 4\tau$ events with an electron or muon in the final state. Only the decay products that are visible in the detector are considered.

6.2. Systematic Uncertainties for the Reconstruction and Identification Efficiency

high boost ($p_T(\tau_{\text{had}}^{\text{truth}}) > 200 \text{ GeV}$ and $p_T(\ell^{\text{truth}}) > 100 \text{ GeV}$). They also take into account the higher p_T values for $\tau_{\text{had}}^{\text{truth}}$ decays compared to ℓ^{truth} . An example of the efficiencies in one of the kinematic regions is shown in figure 6.3 for both semi-leptonic channels.

ΔR	$p_T(\tau_{\text{had, vis}})$	$p_T(\tau_{\text{lep}})$
Small 0 - 0.2	Low 0 - 20 GeV	Low 0 - 20 GeV
Medium 0.2 - 0.4	Medium 20 - 200 GeV	Medium 20 - 100 GeV
Large 0.4 - 1.0	High > 200 GeV	High > 100 GeV

Figure 6.2.: Kinematic regions for the reconstruction, identification and energy scale uncertainties given by a three-dimensional binning in $\Delta R(\tau_{\text{had}}^{\text{truth}}, \ell^{\text{truth}})$, $p_T(\tau_{\text{had}}^{\text{truth}})$ and $p_T(\ell^{\text{truth}})$.

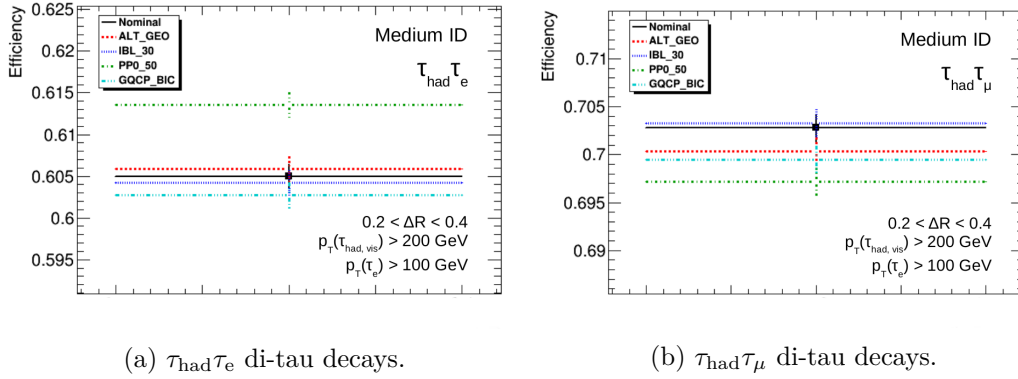


Figure 6.3.: Identification efficiencies for semi-leptonic di-taus in one specific kinematic region, derived from the nominal, ALT_GEO, IBL_30, PPO_50 and QGSP_BIC samples and for a medium working point.

In case of $\tau_{\text{had}}\tau_e$ di-tau decays, the reconstruction and identification efficiencies are listed in figure 6.4, where the entries along the horizontal axis belong to the working points and the different kinematic bins are displayed on the vertical axis. In the regions with a medium or large $\Delta R(\tau_{\text{had}}^{\text{truth}}, e^{\text{truth}})$ and at least one tau with a high p_T whilst the second one does not fall into the low p_T bin, reconstruction efficiencies of $\approx 80\text{--}96\%$ can be achieved. Only for di-taus with a large $\Delta R(\tau_{\text{had}}^{\text{truth}}, e^{\text{truth}})$, medium $p_T(\tau_{\text{had}}^{\text{truth}})$ and high $p_T(e^{\text{truth}})$ a drop down to $\approx 63\%$ can be observed, since these constraints reel in a significant amount of di-taus that do not pass the $p_T > 300 \text{ GeV}$ seed jet cut. This effect becomes even more apparent when the transverse momenta of both the visible τ_{had} decay and the electron are in the medium p_T regime. Since

6. Systematic Uncertainties for Semi-Leptonic Di-Tau Decays

there the electron and τ_{had} subjet alone can definitely not pass the 300 GeV threshold, only very few di-tau candidates acquire a sufficient amount of p_T from the remaining anti- k_t ($R = 1.0$) jet area. Di-taus that either have a low $p_T(\tau_{\text{had}}^{\text{truth}})$, a low $p_T(e^{\text{truth}})$ or a small $\Delta R(\tau_{\text{had}}^{\text{truth}}, e^{\text{truth}})$ are gathered in one bin. As the contribution from candidates that pass the identification selection is negligible when either of the two p_T requirements is fulfilled, the remaining reconstruction efficiency of about 35% stems from di-taus with a small $\Delta R(\tau_{\text{had}}^{\text{truth}}, e^{\text{truth}})$. Although the efficiency of the newly trained reconstruction rapidly decreases below $\Delta R(\tau_{\text{had}}^{\text{truth}}, e^{\text{truth}}) = 0.2$ due to the size of the anti- k_t ($R = 0.2$) subjet, a substantial amount of $\tau_{\text{had}}\tau_e$ candidates can be collected down to $\Delta R(\tau_{\text{had}}^{\text{truth}}, e^{\text{truth}}) = 0.1$. Considering the identification efficiencies, the best agreement between the desired values (95%, 80%, 65% and 50% for VeryLoose, Loose, Medium and Tight) is obtained in the regions where the most di-taus have been reconstructed in the first place. As the definition of the identification efficiency in figure 6.4 also takes into account the reconstruction efficiency, they are expected to lie below the targeted ones from the working point tuning.

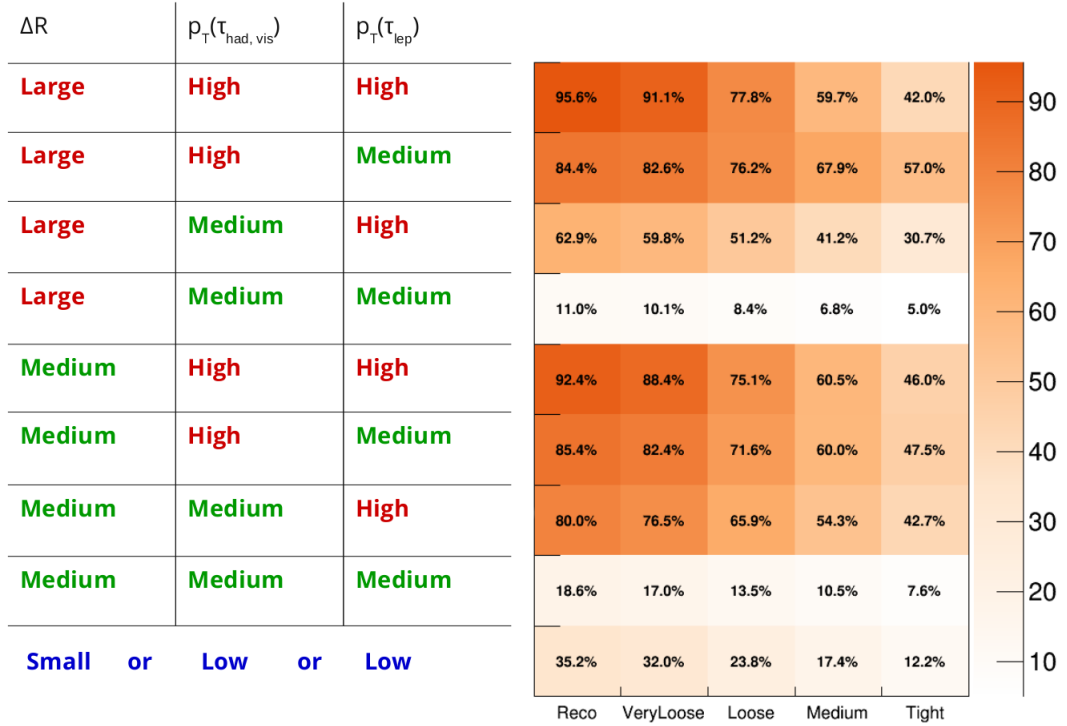


Figure 6.4.: Nominal reconstruction and identification efficiencies for $\tau_{\text{had}}\tau_e$ di-taus considering all working points and kinematic regions.

The resulting relative systematic uncertainties in figure 6.5 are stated in accordance with the two-dimensional scheme of the efficiency table in figure 6.4. In most kinematic regions, they amount to $\approx 0.5\text{--}3\%$, while the overall increase towards

6.2. Systematic Uncertainties for the Reconstruction and Identification Efficiency

tighter working points is mostly a consequence of the lower identification efficiencies. In the regime where both $p_T(\tau_{\text{had}}^{\text{truth}})$ and $p_T(e^{\text{truth}})$ are restricted to medium values the uncertainties rise to 4–6% because of the very low reconstruction efficiency. As they roughly stay the same across the identification selections, their absolute values also decrease as the identification efficiency gets lower. The efficiencies derived from the PPO_50 modification are the only ones that do not merely fluctuate around the nominal values, but let more di-taus pass the identification in every kinematic bin (as for example in figure 6.3a). Since this systematic shift has not been observed in case of the fully-hadronic mode, it has to be accounted for by the electron reconstruction and identification, e. g. by an altered track selection.

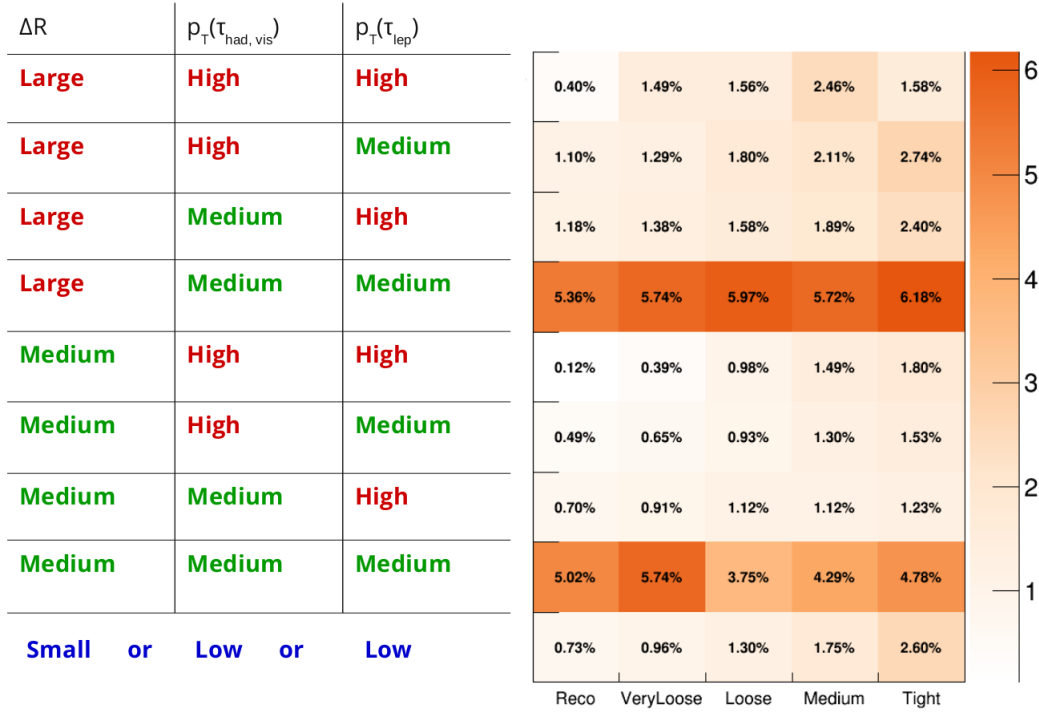


Figure 6.5.: Relative systematic uncertainties for the reconstruction and identification efficiencies of $\tau_{\text{had}}\tau_e$ di-taus considering all working points and kinematic regions.

For $\tau_{\text{had}}\tau_\mu$ decays the reconstruction and identification efficiencies are depicted in figure 6.6. They follow a similar three-dimensional kinematic binning as in the $\tau_{\text{had}}\tau_e$ case, though here di-taus with a small $\Delta R(\tau_{\text{had}}^{\text{truth}}, \mu^{\text{truth}})$ are not included in the low $p_T(\tau_{\text{had}}^{\text{truth}})$ and $p_T(\mu^{\text{truth}})$ bin since the reconstruction still yields good results in this regime. Except for the low p_T region, the reconstruction efficiencies range from about 85 % to 97 %. In accordance with the $\tau_{\text{had}}\tau_\mu$ tuning results (see figure A.4a), the identification efficiencies show a more rapid decrease in the high and especially in the small $\Delta R(\tau_{\text{had}}^{\text{truth}}, \mu^{\text{truth}})$ bins. Unlike for the efficiencies of the $\tau_{\text{had}}\tau_e$ di-taus

6. Systematic Uncertainties for Semi-Leptonic Di-Tau Decays

no systematic shift that is persistent in all kinematic regions is observed for either of the samples. The corresponding uncertainties, shown in figure 6.7, amount to 0.1–2% in most bins.

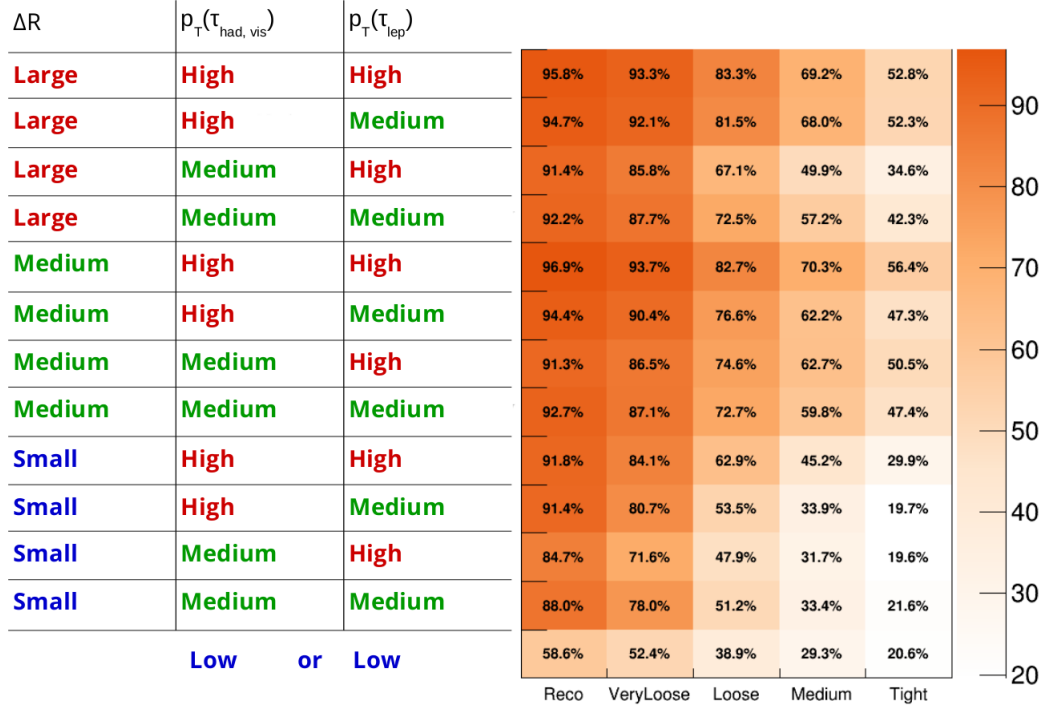


Figure 6.6.: Nominal reconstruction and identification efficiencies for $\tau_{\text{had}}\tau_{\mu}$ di-taus considering all working points and kinematic regions.

6.3. Systematic Uncertainties for the Di-Tau Energy Scale

In good approximation (see [17]), for both semi-leptonic channels the di-tau energy scales from simulation and from data are assumed to be identical in the course of this discussion. Similar to the reconstruction and identification uncertainties, the nominal distributions of the transverse momentum of truth-matched di-taus are compared to the ALT_GEO, IBL_30, PPO_50 and QGSP_BIC variations. Again, the uncertainties are provided in different kinematic regions according to figure 6.2 and an example for each decay mode is pictured in figure 6.8. Their computation starts with the application of a small scale factor α ($\alpha \ll 1$) to the p_T of the di-tau for each modified sample. The distributions with the newly derived energy scales

$$p_T^{\text{scaled}}(\text{di-tau}^{\text{truth}}) = (1 + \alpha) \cdot p_T(\text{di-tau}^{\text{truth}}) \quad (6.3)$$

are then compared to the unscaled nominal one with the help of a χ^2 -test. Repeating this procedure for different α values generates distributions of χ^2 -values that are

6.3. Systematic Uncertainties for the Di-Tau Energy Scale

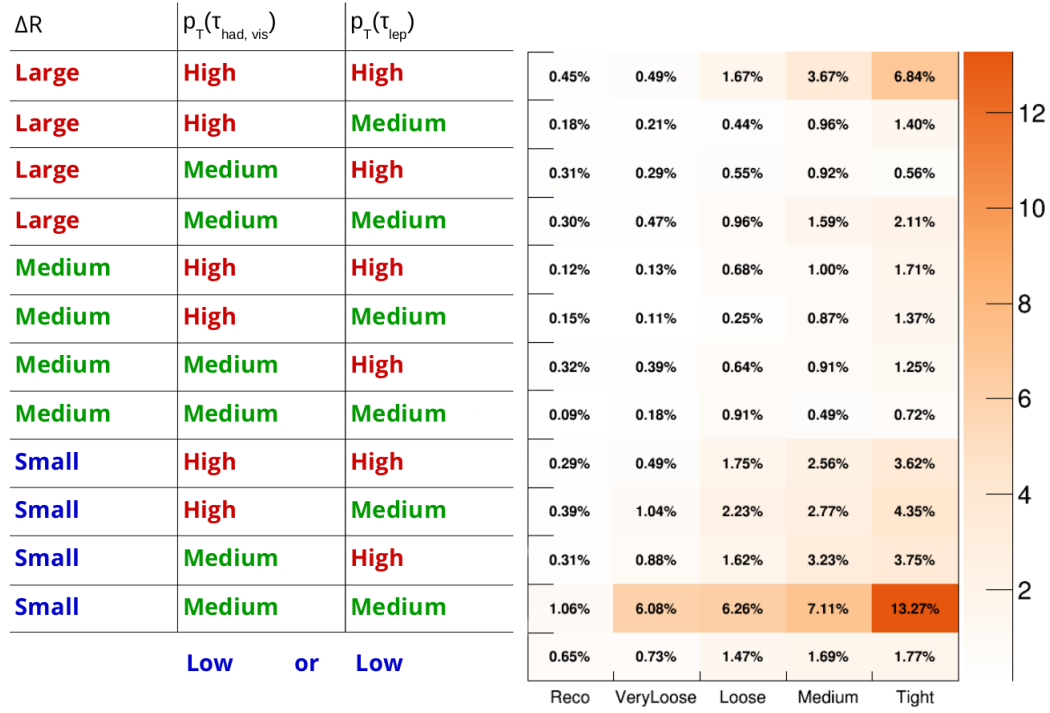


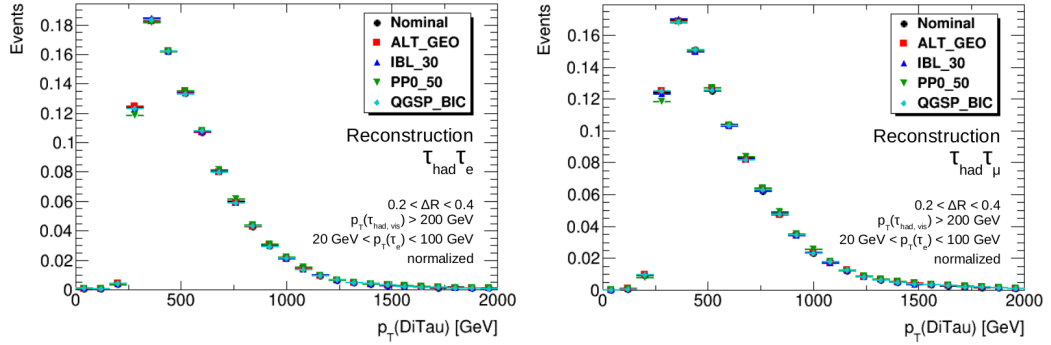
Figure 6.7.: Relative systematic uncertainties for the reconstruction and identification efficiencies of $\tau_{\text{had}}\tau_{\mu}$ di-taus considering all working points and kinematic regions.

6. Systematic Uncertainties for Semi-Leptonic Di-Tau Decays

parabolic in good approximation (see figure 6.9²). For each variation, the value of α that minimizes the χ^2 per degree of freedom is taken as the individual uncertainty. The total uncertainty

$$\alpha_{\text{tot}} = \sqrt{\sum_{\text{Variations}} \alpha_{\text{min,Variation}}^2} \quad (6.4)$$

is once more given by the quadratic sum of each contribution. Since the nominal scaling is set to one ($\alpha = 0$), α_{tot} provides both an absolute and relative description. The outcome is summarized in figure 6.10 for $\tau_{\text{had}}\tau_e$ decays and in figure 6.11 for the $\tau_{\text{had}}\tau_\mu$ channel. In both cases, the resulting uncertainties range from about 0.2% to 2% and their spread presumably is covered by statistical fluctuations. Though the identification for both semi-leptonic modes is slightly biased towards di-taus with a p_T between roughly 200 GeV and 600 GeV (see figure 6.12), forwarding the uncertainties for reconstructed di-taus alone to an analysis could thus be a reasonable recommendation. Only the PPO_50 variation shows a persistent shift in the di-tau p_T -distribution for both decay modes and considering all kinematic regions, thereby contributing the most to the total uncertainties (as indicated in figure 6.9).



(a) $\tau_{\text{had}}\tau_e$ di-tau decays.

(b) $\tau_{\text{had}}\tau_\mu$ di-tau decays.

Figure 6.8.: Normalized distributions of the transverse momentum for reconstructed and truth-matched semi-leptonic di-taus in one specific kinematic region, derived from the nominal, ALT_GEO, IBL_30, PPO_50 and QGSP_BIC samples.

6.4. Summary for the Semi-Leptonic Di-Tau Decays

This chapter has investigated the event topology of $G_{\text{RS}}^{\text{bulk}} \rightarrow hh \rightarrow 4\tau$ decays with regard to semi-leptonic decays of two close-by tau leptons, as well as a calculation of corresponding systematic uncertainties. It has been shown that heavy resonances,

²For technical reasons, the distributions in figure 6.9 have been obtained by applying the scale factor on the nominal rather than the modified samples, which can be seen when figure 6.8 and figure 6.9 are inspected closely, e. g. in case of the PPO_50 variation.

6.4. Summary for the Semi-Leptonic Di-Tau Decays

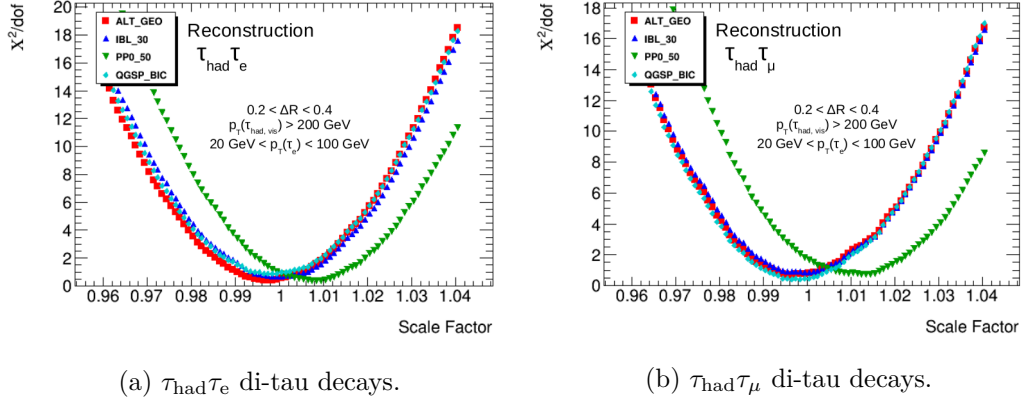


Figure 6.9.: χ^2 -values per degree of freedom (dof) for different scale factors ($1 + \alpha$) applied on the energy scale of reconstructed and truth-matched semi-leptonic di-taus in one specific kinematic region, derived from the nominal, ALT_GEO, IBL_30, PPO_50 and QGSP_BIC samples.

ΔR	$p_T(\tau_{\text{had, vis}})$	$p_T(\tau_{\text{lep}})$						
Large	High	High	1.16%	0.91%	1.16%	1.32%	1.36%	2 1.8 1.6 1.4 1.2 1 0.8 0.6 0.4 0.2
Large	Medium	High	0.50%	0.36%	0.57%	0.82%	0.27%	
Large	High	Medium	0.52%	0.39%	0.52%	0.90%	0.57%	
Large	Medium	Medium	0.22%	0.76%	1.00%	1.65%	2.13%	
Medium	High	High	0.96%	0.95%	0.96%	0.96%	0.95%	
Medium	Medium	High	0.59%	0.61%	0.74%	0.82%	0.76%	
Medium	High	Medium	0.91%	0.90%	0.98%	0.99%	1.25%	
Medium	Medium	Medium	0.17%	0.10%	0.22%	1.58%	1.16%	
Small or	Low or	Low	0.22%	0.39%	0.54%	0.74%	0.41%	
			Reco	VeryLoose	Loose	Medium	Tight	

Figure 6.10.: Systematic uncertainties for the energy scale of $\tau_{\text{had}}\tau_e$ di-taus considering all working points and kinematic regions.

6. Systematic Uncertainties for Semi-Leptonic Di-Tau Decays

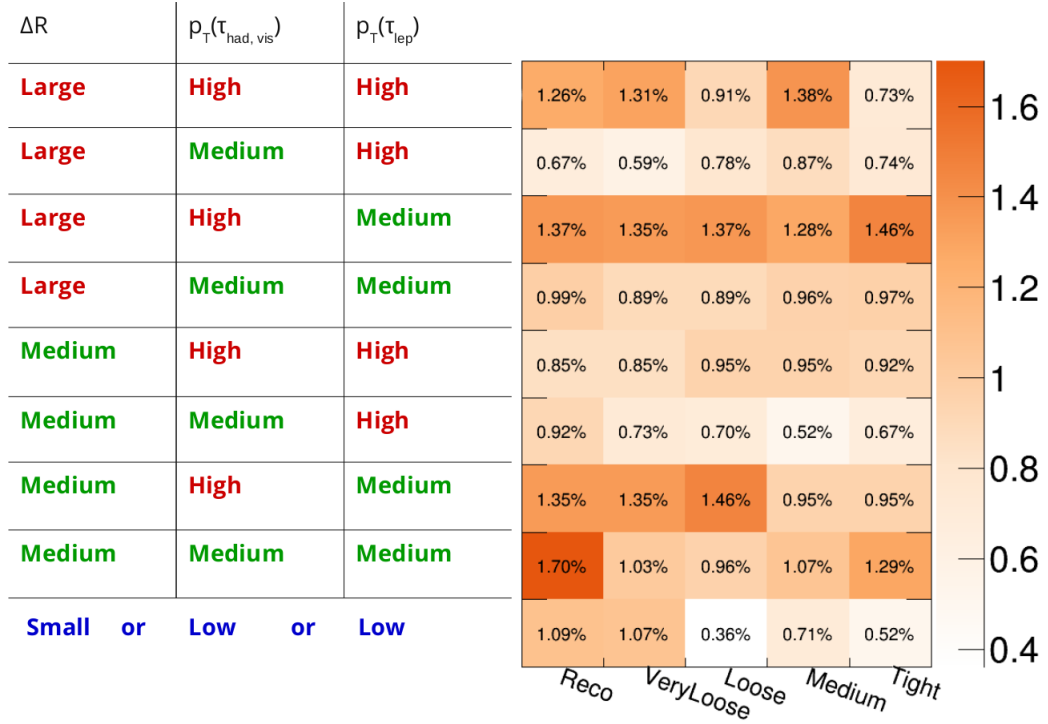


Figure 6.11.: Systematic uncertainties for the energy scale of $\tau_{\text{had}}\tau_{\mu}$ di-taus considering all working points and kinematic regions.

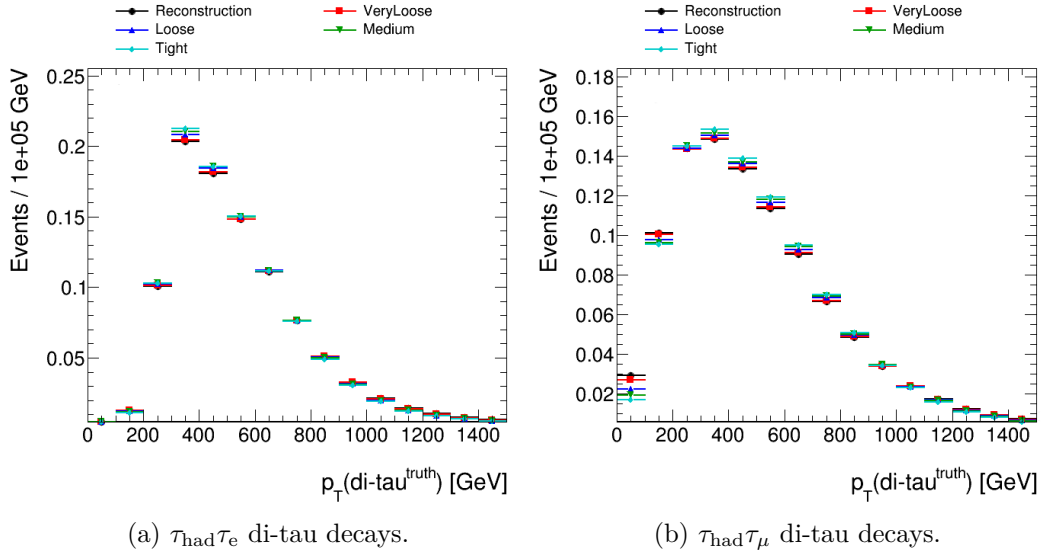


Figure 6.12.: Normalized distributions of the transverse momentum of reconstructed and truth-matched semileptonic di-taus considering different working points.

6.4. Summary for the Semi-Leptonic Di-Tau Decays

e. g. multi-TeV Randall-Sundrum gravitons and their subsequent decay into pairs of SM-like Higgs bosons, may lead to highly collimated and boosted pairs of tau leptons.

An in-depth discussion for the systematic uncertainties has been presented, though considering their application in the $G_{\text{RS}}^{\text{bulk}} \rightarrow \text{hh} \rightarrow \text{bb}\tau\tau$ analysis, they can be summarized with respect to the most relevant kinematic regions. Thus, for semi-leptonic di-tau decays with $p_{\text{T}}(\text{di-tau}) > 300 \text{ GeV}$, high reconstruction efficiencies of about 80 %–95 % are achieved. In this regime, for $\tau_{\text{had}}\tau_{\text{e}}$ and $\tau_{\text{had}}\tau_{\mu}$ decays respectively, the relative uncertainties for the reconstruction and identification efficiencies yield 0.5 %–3 % and 0.1 %–2 %. Among the four systematic variations of the $G_{\text{RS}}^{\text{bulk}} \rightarrow \text{hh} \rightarrow \text{bb}\tau\tau$ samples, the PPO_50 modification shows a persistent shift in all kinematic regions for $\tau_{\text{had}}\tau_{\text{e}}$ decays, but not in the $\tau_{\text{had}}\tau_{\mu}$ case.

For both decay modes alike and in all kinematic bins, the systematic uncertainties on the di-tau energy scale amount to 0.2 %–2 %. Again, PPO_50 leads to a significant shift in all distributions, albeit in this case for both semi-leptonic decay modes.

7. Validation Studies for Boosted Di-Taus in Z+jets Events

In this chapter, the reconstruction and identification of fully-hadronic di-tau decays is studied. The corresponding algorithms are validated, and it is investigated whether they lead to compatible results for data and Monte Carlo simulations. In order to do so, an analysis looking into decays of boosted Z bosons in $Z \rightarrow \tau\tau(+\text{jets})$ events is presented. The corresponding data and Monte Carlo samples are summarized in section 7.1. To begin with, the signal topology is introduced in section 7.2. Then, the cut selection is outlined in section 7.3, and a data-driven two-dimensional side-band approach is introduced in order to estimate the contribution of fake di-tau candidates from QCD. Following the discussion of the distributions of several variables in the signal region in section 7.5, scale factors for the di-tau identification are computed around the Z mass peak in section 7.6, while comparing two different Monte Carlo generators in terms of the signal samples, i. e. Powheg+Pythia8 and Sherpa 2.2.1.

7.1. Data and Monte Carlo Samples

The datasets that are analysed in the following were recorded by the ATLAS detector during the 2015-2017 pp operating periods of Run 2 at $\sqrt{s} = 13$ TeV (see tables B.4, B.5 and B.6). They amount to a total integrated luminosity of 80.4 fb^{-1} , with 36.1 fb^{-1} and 44.3 fb^{-1} corresponding to the combined 2015/2016 and 2017 data-taking campaigns respectively. When assessing the complexity of the collected events in order to produce accurately modelled Monte Carlo simulations, the mean number of interactions per bunch crossing is a crucial quantity. Due to the different operating conditions and beam parameters it has changed significantly over the course of the three years (see figure 7.1). To account for these differences, two sets of Monte Carlo samples from the MC16 production campaign are employed to match the individual pile-up profiles from 2015/2016 (MC16a) and 2017 (MC16d) (see tables B.7 and B.8). While each sample is scaled to the integrated luminosity of the dataset it corresponds to, the cross sections, filter efficiencies and weights for higher order corrections are identical for the two subsets. For the $Z \rightarrow \tau\tau(+\text{jets})$ signal process two different Monte Carlo simulations are compared: On the one hand an inclusive sample that contains events with $m_{\text{inv}}(\tau\tau) > 60 \text{ GeV}$ generated by Powheg [94] and interfaced to Pythia8 [87] and EvtGen [90] for the parton shower modelling is analysed. On the other hand a simulation produced with Sherpa 2.2.1 [95] with

$m_{\text{inv}}(\tau\tau) > 40 \text{ GeV}$ is used. The latter is sliced with the MAX(HT, pTV) option ¹ and the application of filters according to the heavy-flavour content. The background processes that are considered in this analysis, $W \rightarrow \tau\nu(+\text{jets})$, $t\bar{t}$ and di-boson decays (WW, WZ, and ZZ), are also produced with either of the two aforementioned generators. A full list and details on the PDF sets and tunings can be found in table B.7 for MC16a and in table B.8 for MC16d. Other processes, such as single top production, $W \rightarrow e\nu(+\text{jets})$ and $Z \rightarrow ee$, have been investigated and their contributions were found to be negligible. For all processes the simulation of the ATLAS detector was done with GEANT4 [91, 92].

The reconstruction algorithms explained in chapter 4 are run on both measured data and the Monte Carlo simulations. The outcome is stored in accordance with the event data model (EDM) of ATLAS [96] and contains all information that is necessary for a physics analysis. However, these AOD (Analysis Object Data) files are typically very large ($\sim \text{PB}$) and impractical for a day-to-day usage. Analysis groups are therefore provided with derived formats (DAODs), which are also centrally produced, where certain events, objects or variables are discarded and new high-level information is added. The HIGG4D6 dataset derivation used in this thesis fits the needs of the $G_{\text{RS}}^{\text{bulk}} \rightarrow hh \rightarrow bb\tau\tau$ analysis and holds reconstructed di-taus from the fully-hadronic decay channel (see chapter 5). Recorded events were triggered by either of the high- p_{T} anti- k_{t} ($R = 1.0$) jet triggers to be found in B.3. All results are derived with the help of the ATLAS analysis software (AnalysisBase 21.2) and the ROOT data analysis framework [97].

7.2. Boosted Topology

The topology which these studies aim to investigate consists of a boosted Z boson decaying to a pair of tau leptons in the fully hadronic final state and a hadronic recoil with a large transverse momentum. Owing to the trigger selection, i. e. the requirement of a high- p_{T} anti- k_{t} ($R = 1.0$) jet, the $Z \rightarrow \tau\tau(+\text{jets})$ samples already are preselected for boosted pairs of tau leptons. This can be seen in figure 7.2, where the majority of simulated tau pairs comes with a spatial separation of $0.2 < \Delta R < 1.0$. There, an event has most likely been triggered by either the seed jet of the di-tau or the recoil system. Although this entails also a significant contribution from semi- and fully-leptonic di-tau decays, even with muons in the final state, they are very unlikely to be reconstructed and identified as fully-hadronic di-tau decays later on.

The trigger ensures that both the signal and background samples mostly contain boosted back-to-back topologies. Regarding the latter, this includes for example boosted W bosons with a corresponding recoil jet from $W \rightarrow \tau\nu(+\text{jets})$, a top and anti-top quark flying in opposite directions or high- p_{T} di- and multi-jet QCD processes.

¹The slicing considers the maximum of the p_{T} of the Z boson and the scalar sum of the transverse momenta of all parton-level jets above 20 GeV.

7. Validation Studies for Boosted Di-Taus in $Z+\text{jets}$ Events

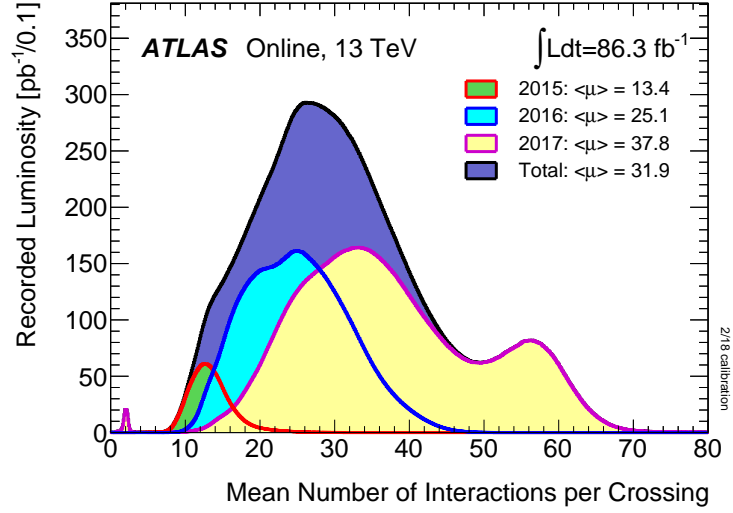


Figure 7.1.: Luminosity-weighted distributions of the mean number of interactions per bunch crossing for the 2015–2017 pp collision data at $\sqrt{s} = 13 \text{ TeV}$ [98].

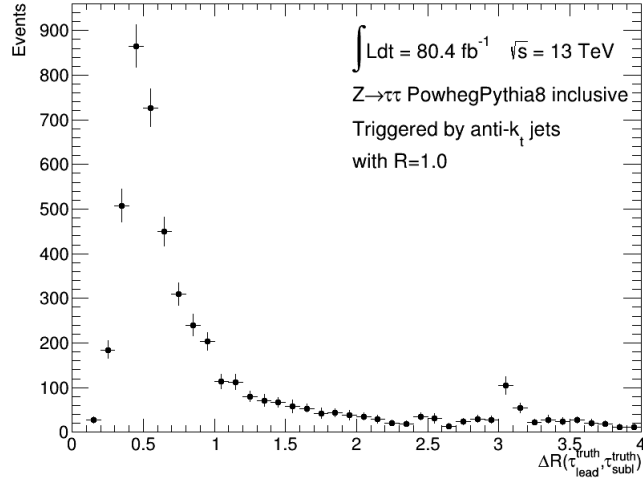


Figure 7.2.: Spatial separation ΔR between two simulated taus taken from $Z \rightarrow \tau\tau(+\text{jets})$ events generated with Powheg and Pythia8 and triggered by an anti- k_t jet with $R = 1.0$. Every event that contains at least two simulated taus is considered and the distribution is scaled to $\mathcal{L} = 80.4 \text{ fb}^{-1}$.

7.3. Event Selection

With no further selection, for the medium working point the background contribution is still at least one order of magnitude larger than the number of true tau pairs in a boosted Z boson decay. For that reason, cuts on several event and di-tau related variables are applied. Though it is not the intention of this thesis to rediscover the Z boson in the di-tau final state, they are optimized according to the significance [99] of true boosted $Z \rightarrow \tau_{\text{had}}\tau_{\text{had}}$ events which are treated as signal. The analysis that is outlined in the following sections makes use of the Sherpa-generated $Z \rightarrow \tau\tau(+\text{jets})$ samples. They provide better statistics in the regime of highly boosted Z bosons due to the p_{T} -slicing, and therefore allow for a more refined cut optimization.

The cut selection is primarily motivated by physics properties that are distinct for true di-taus and candidates from background. Besides, explicit cuts on the di-tau kinematics are largely avoided. Since this study serves as a validation, any restrictions on the phase space are preferably left for an actual analysis application.

The cut selection is optimized for the medium working point because it is preferred by the $G_{\text{RS}}^{\text{bulk}} \rightarrow \text{hh} \rightarrow \text{bb}\tau\tau$ analysis and poses a good trade-off between signal efficiency and background rejection. For reconstructed di-tau candidates prior to the event selection, the score of the BDT classifier is shown in figure 7.3. In addition to the medium di-tau identification cut, four cuts are employed in the event selection. They are listed and explained in the following:

- $E_{\text{T,miss}} > 75 \text{ GeV}$
- $|\Delta\phi(\text{di-tau}, \text{MET})| < 1.0$
- Zero b-tags on the anti- k_t ($R = 1.0$) seed jet
- $p_{\text{T}}(\text{subleading subjet}) > 50 \text{ GeV}$

The event yields for each cut are summarized in table 7.1, and the distributions for the corresponding variables, where the candidates have already passed the identification, are depicted in figure 7.4. One at a time, the histograms include another cut from the aforementioned list and thereby reflect their order of implementation. Only the background processes taken from the Monte Carlo samples are shown, because the data-driven estimation of the contribution that arises from QCD fake candidates (see section 7.4) is done in a more signal-like region. Nevertheless, figures 7.4a and 7.4b serve as a very approximate justification of the cuts that intend to reduce the QCD background

Due to the two neutrinos in the final state, signal events are expected to have a significant amount of missing transverse energy. According to figure 7.4a, truth-matched $Z \rightarrow \tau_{\text{had}}\tau_{\text{had}}$ di-taus can be found across a wide $E_{\text{T,miss}}$ range with a slow decrease from 20 GeV onwards. Fake candidates from QCD events however typically generate values smaller than 100 GeV, for instance because they may possess more balanced $E_{\text{T,miss}}$ topologies. Although it takes away a substantial amount of signal

7. Validation Studies for Boosted Di-Taus in Z +jets Events

events, the $E_{T,\text{miss}}$ selection is the cut that is the most effective against the QCD background.

In the case of a true signal event, the missing transverse energy points approximately in the same direction as the di-tau system. At the least, it should most of the time lie within the cone of the anti- k_t ($R = 1.0$) seed jet. Cutting on the azimuthal separation between the di-tau and $E_{T,\text{miss}}$ direction (see figure 7.4b) further reduces the QCD contribution, while almost no signal is lost.

Top quarks decay to a b quark and a W boson in almost all cases [100], and the final state is thus given by the couplings of the W boson. When events where the di-tau seed jet is initiated by a b hadron are rejected, the $t\bar{t}$ background is reduced by about two thirds (see figure 7.4c). The remaining contribution is mostly accounted for by the efficiency of the b-tagging algorithms. The branching fraction for the W decay into a tau, electron or muon is about 11% for each channel, and very rarely ($\approx 1\%$) a $t\bar{t}$ decay can therefore lead to a true pair of tau leptons. In figure 7.5, considering all physics processes taken from the Monte Carlo simulations except for $Z \rightarrow \tau\tau$ (+jets), truth-matched $Z \rightarrow \tau_{\text{had}}\tau_{\text{had}}$ di-taus that have passed all the selection criteria are depicted.

The last cut, applied on the p_T of the subleading subjet, discards di-taus in the very low p_T regime which are known to be modelled poorly. Moreover, it suppresses the background from $Z \rightarrow \tau\tau$ (+jets) events where there is no truth-match to a pair of hadronically decaying boosted taus. This may include semi-leptonic decays where an electron is falsely identified as a τ_{had} candidate or di-taus with only one simulated hadronic tau decay. Though strictly speaking this restricts the available di-tau phase space it is only a very minor cut in terms of the $G_{\text{RS}}^{\text{bulk}} \rightarrow \text{hh} \rightarrow \text{bb}\tau\tau$ kinematics.

The largest background contribution in the final selection, which cannot easily be reduced by a dedicated cut, is thus given by $W \rightarrow \tau\nu$ (+jets) events. Since these most likely include one simulated τ_{had} decay and genuine $E_{T,\text{miss}}$, their signature comes close to a signal event. The second τ_{had} candidate would then come from a misidentified jet.

Di-boson decays contribute only very little throughout all the selection regions, although they form the most signal-like background. As they contain WW, WZ and ZZ productions there are multiple possibilities for at least one true τ_{had} decay per event. Moreover, these processes generate true hadronic di-tau decays, where the two τ_{had} candidates originate from a single boosted Z boson (WZ, ZZ), from a W boson each (WW) or from a combination of the above (WZ) (see figure 7.5).

As explained in section 7.2, the boosted $Z \rightarrow \tau\tau$ (+jets) topology has been examined in detail, especially with respect to the kinematic relationship between the Z decay and its recoil system. In particular, events with identified di-tau candidates have been checked to contain a hadronic recoil with a sufficiently high p_T by matchings of anti- k_t ($R = 1.0$) and anti- k_t ($R = 0.4$) jets with regard to their spatial separation, e.g. in ΔR and $\Delta\phi$, to the di-tau candidate. However, most di-tau candidates have been found to possess such a recoil system, in both signal and background events alike. Therefore no additional cuts could be derived from this study in order

Table 7.1.: Event yields for the boosted $Z \rightarrow \tau_{\text{had}}\tau_{\text{had}}$ selection. Fake candidates from QCD are estimated by a data-driven approach, and thus are only available in the final signal region.

Selection	$Z \rightarrow \tau_{\text{had}}\tau_{\text{had}}$ truth-matched	Process				QCD fakes	data
		$Z \rightarrow \tau\tau$	$W \rightarrow \tau\nu$	$t\bar{t}$	di- boson		
BDT score > 0.72	1787.1	187.9	285.3	501.6	63.1	-	9761
$E_{\text{T,miss}} > 75$ GeV	995.2	119.6	190.6	277.7	41.2	-	1992
$ \Delta\phi(\text{di-tau}, \text{MET}) < 1.0$	973.3	116.6	180.5	241.7	38.5	-	1409
B veto	792.7	100.1	160.6	83.1	31.6	-	1068
$p_{\text{T}}(\text{subleading subjet}) > 50$ GeV	593.5	40.8	116.0	57.4	21.9	65.2	735

to increase the significance of the signal. Nonetheless, the outcome validates the specific choice of high- p_{T} anti- k_t ($R = 1.0$) jet triggers and the preselection of the dataset derivation, i. e. a skim for events with at least two anti- k_t ($R = 1.0$) jets with $p_{\text{T}} > 300$ GeV (see section 7.7), to select the desired boosted topology.

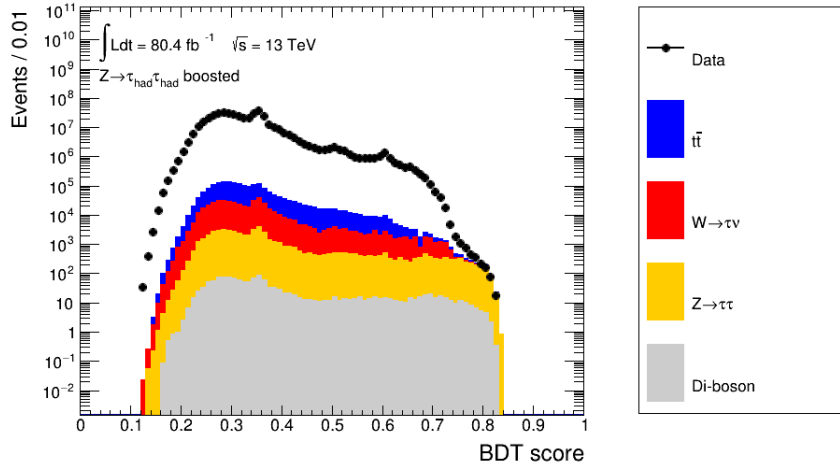


Figure 7.3.: Score of the BDT classifier for reconstructed di-taus in the fully hadronic decay channel. The four working points are given by lower cuts at 0.60 (very loose), 0.65 (loose), 0.72 (medium) and 0.77 (tight).

7.4. Estimation of QCD Fakes

The background that arises from mistakenly reconstructed QCD events is estimated with a two-dimensional side-band method, often called ABCD-method, which is a data-driven approach that is a common tool for many analyses at ATLAS and CMS. It is employed whenever there is no dedicated Monte Carlo simulation for a certain physics process or the available ones do not describe the datasets with sufficient

7. Validation Studies for Boosted Di-Taus in Z +jets Events

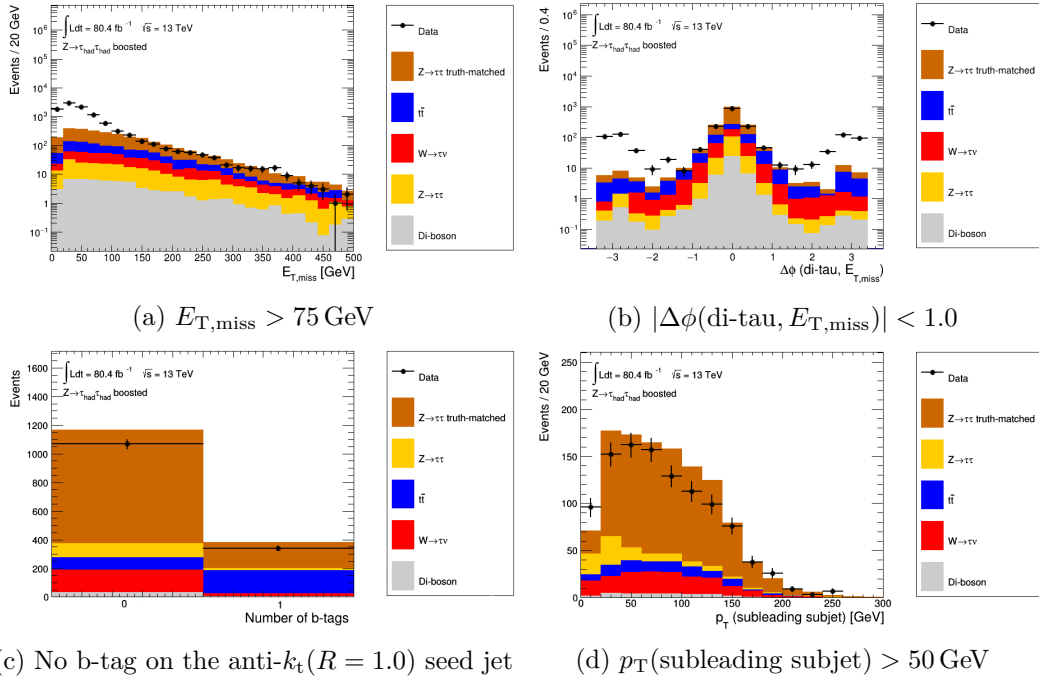


Figure 7.4.: Illustration of the boosted $Z \rightarrow \tau_{\text{had}}\tau_{\text{had}}$ cut selection. Cuts are added successively from the top-left to the bottom-right. The sub-captions indicate the cut that is implied by the respective histogram and applied in the subsequent one. The QCD background contribution is obtained from a data-driven estimation later on.

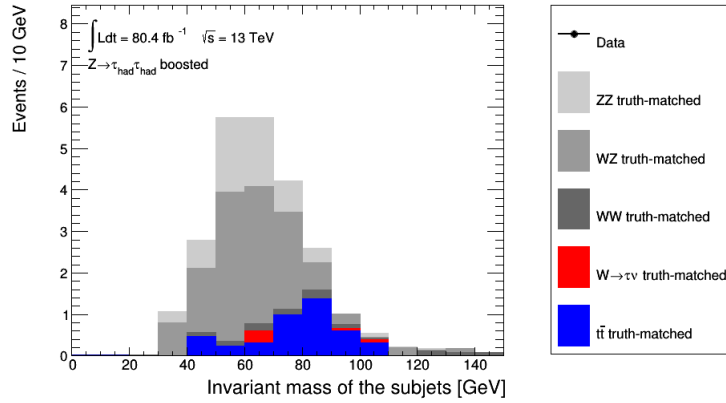


Figure 7.5.: Invariant mass of the two di-tau subjects, depicted for all considered physics processes except for $Z \rightarrow \tau\tau$ (+jets) and QCD, where the events have been truth-matched to a fully hadronic di-tau decay and have passed all selection criteria.

accuracy. The reasons for this might be modelling issues or a lack of statistics. The latter especially applies to analyses looking into sparsely populated corners of phase space, e. g. the search for boosted di-taus.

The estimation defines four regions, labelled A, B, C and D, by choosing two uncorrelated variables and applying a cut in each of them. The basic assumption then is that, given an appropriate assignment, the ratio of the number of fake candidates N stays the same across the regions, for instance that $\frac{N_A}{N_B} = \frac{N_C}{N_D}$.

Specifically, in this thesis the di-tau candidates are split into four subsets according to whether they pass or fail the identification and the $E_{T,\text{miss}}$ cut (see table 7.2), where A refers to the actual signal region. For regions B, C and D the corresponding distributions of the transverse momenta of the di-tau subjects can be seen in figure 7.6. Apart from this categorization, every di-tau is required to pass the full event selection as described in section 7.3. As a consequence, the estimated QCD fakes are only available at a very late stage in the analysis, yet this strategy avoids any extrapolation issues that could arise if the fake candidates had to be propagated through the event selection. Additionally, in exchange for the $E_{T,\text{miss}}$ side-bands the fake estimation has been tested with a distinction of di-taus with regard to their summed track charge (see figure 7.9b). Although the result is equally good, the $E_{T,\text{miss}}$ approach provides better statistics in the fake estimation regions, especially for signal-like di-tau candidates that pass the identification (see figure 7.6b).

To determine the amount of QCD fakes in region B, C and D, all Monte Carlo processes, including $Z \rightarrow \tau\tau(+\text{jets})$ events, are subtracted from data. Eventually, region A can then be populated with

$$N_A = N_B \cdot \frac{N_C}{N_D} \quad (7.1)$$

fake di-taus.

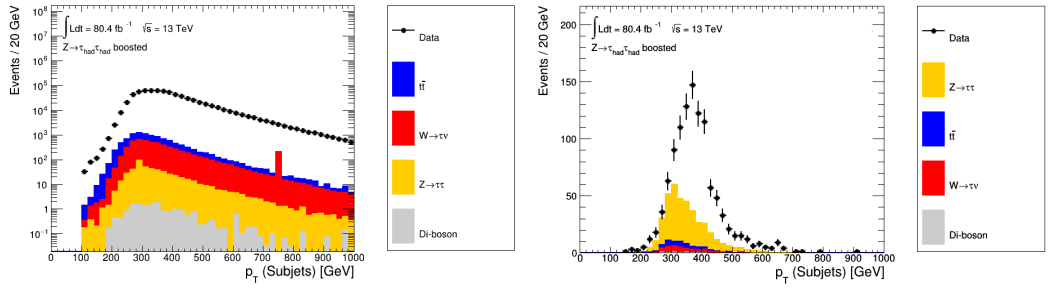
The resulting fake factors ($\frac{N_C}{N_D}$), which are binned in the transverse momentum of the two di-tau subjects ($p_T < 400$ GeV or $p_T > 400$ GeV), are shown in figure 7.7. The bin width and count is motivated by the amount of di-tau candidates in region C, which contains the least events compared to regions B and D.

Because of the high QCD background rejection ($\sim 10^4$) of the di-tau identification (see figure A.1), they are very small, i. e. of order 10^{-4} . The fake factors are derived and applied separately for the MC16a and MC16d samples, though they are statistically compatible for the two subcampaigns. In future, they may be derived inclusively for the entire Run 2 data-taking period.

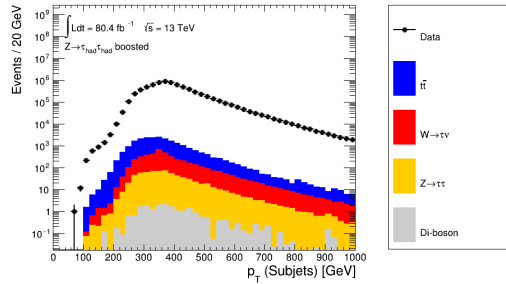
Table 7.2.: Region definitions for the ABCD-method.

	BDT score > 0.72	0.2 < BDT score < 0.72
$E_{T,\text{miss}} > 75$ GeV	A	B
$E_{T,\text{miss}} < 75$ GeV	C	D

7. Validation Studies for Boosted Di-Taus in Z +jets Events



(a) Region B (ID fail and $E_{T,miss} > 75$ GeV). (b) Region C (ID pass and $E_{T,miss} < 75$ GeV)



(c) Region D (ID fail and $E_{T,miss} < 75$ GeV)

Figure 7.6.: Control regions for the QCD fake estimation. They differ from the final event selection in the signal region by the inversion of either or both of the BDT score and $E_{T,miss}$ cuts.

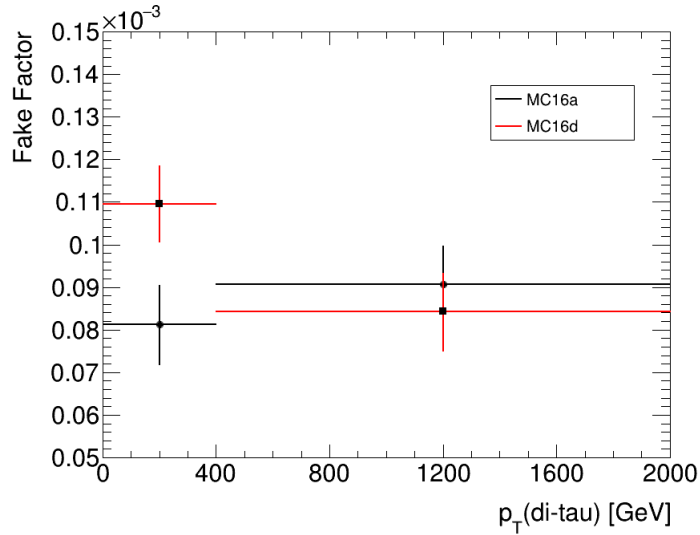


Figure 7.7.: Fake factors for the data-driven QCD background estimation.

7.5. Description of the Signal Region

In this section, the distributions of the signal region are presented and discussed. They are obtained from the data and Monte Carlo samples introduced in section 7.1, the QCD fake contribution that has been estimated in section 7.4 and include the event selection of section 7.3.

In the following, each histogram is equipped with a corresponding ratio plot that includes statistical uncertainties on both data and background. Additionally, the agreement between the two is assessed quantitatively by a χ^2 - and a Kolmogorov-Smirnov(KS)-test. The former displays the χ^2 value per degree of freedom ² and compares both the shape and normalization of data and simulation. The KS-test however is sensitive to the shape only.

To begin with, the di-tau kinematics are illustrated in figure 7.8. They show the invariant mass m_{inv} , the transverse momentum p_T , the pseudorapidity η and the azimuthal angle ϕ of the two di-tau subjects. The invariant mass (see figure 7.8a) peaks at around 60 GeV, i. e. well below $m_Z \approx 91$ GeV, since only the visible products of the τ_{had} decay are considered ³. The p_T -distribution (see figure 7.8b) contains di-taus mostly between 300 GeV and 500 GeV, where the low- p_T regime is largely excluded owing to the 300 GeV cut on the anti- $k_t(R = 1.0)$ seed jet and the upper tail is given by the finite boost of the Z decay. The angular variables demonstrate that di-taus are produced centrally in the detector (see figure 7.8c), but with no preferred direction in the x-y-plane (see figure 7.8d). In more detail, the kinematic distributions for the individual subjects are appended in figures C.1 and C.2.

In order to get a well-rounded impression of the modelling in the signal region, four more event and di-tau related variables are depicted in figure 7.9. The missing transverse energy $E_{T,\text{miss}}$ (see figure 7.9a), which includes the cut at 75 GeV, has already been discussed in the course of the event selection. The charge variable (see figure 7.9b) holds the sum of the charge values from all tracks that have been assigned to the two subjects. Since true $Z \rightarrow \tau_{\text{had}}\tau_{\text{had}}$ decays yield a net charge of zero, it shows a strong peak with the dominant contribution arising from events with truth-matched $Z \rightarrow \tau_{\text{had}}\tau_{\text{had}}$ candidates. The spatial separation between the two subjects (see figure 7.9c) of the di-tau has a lower boundary at $\Delta R = 0.2$ for all signal and background candidates due to the size of the anti- $k_t(R = 0.2)$ jets. Moreover, the majority of all truth-matched $Z \rightarrow \tau_{\text{had}}\tau_{\text{had}}$ decays does not exceed $\Delta R = 0.6$ because of the strong boost. Although a cut at this value would halve the most important background in the signal region, i. e. $W \rightarrow \tau\nu(+\text{jets})$, it severely restricts the di-tau kinematics and is therefore avoided. The ratio between the transverse momenta of the leading and subleading subjet (see figure 7.9d) peaks at 0.2 to 0.4 and continues with a slow decrease until $p_T^{\text{subl}} \approx p_T^{\text{lead}}$, for signal and background

²The number of degrees of freedom is equal to the amount of non-empty bins minus one.

³This result allows for an interesting comparison between the invariant mass spectra derived here and in the studies for the semi-leptonic di-tau decays (see 6.1). Although the Higgs boson is significantly heavier than the Z boson, due to the additional neutrino in the final state the invariant mass there peaks at about the same value but has a much broader distribution.

7. Validation Studies for Boosted Di-Taus in Z +jets Events

events alike. Di-tau candidates with a very imbalanced p_T spread among the subjects, i. e. a p_T ratio smaller than 0.2, are mostly excluded by the $p_T^{\text{subl}} > 50$ GeV cut.

All in all, the shape of the Monte Carlo samples is modelled well in all variables mentioned in this section. On top of that, the same assertion holds for the QCD fakes estimated from data. The difference in normalization, which can be observed in almost every variable, is accounted for by the scale factor that is discussed in the next section. Without prior knowledge concerning the validity of the Monte Carlo samples in the kinematic regime that is studied here, this could be an effect of any or even a combination of the simulated physics processes. What is more, it may also lead to repercussions on the QCD fake estimation. Finding dedicated control regions for either of the backgrounds is difficult, mainly because of the limited statistics or the high contamination with signal events. An example for the latter is given by a potential region with one b-tag on the anti- k_t ($R = 1.0$) di-tau seed jet (see figure 7.4c), which would be the first choice for assessing the modelling of $t\bar{t}$ events. Nonetheless, there is strong evidence that the observed mis-modelling is predominantly accounted for by the truth-matched $Z \rightarrow \tau_{\text{had}}\tau_{\text{had}}$ content. An indication is given by the tail of the mass distribution in figure 7.8a, i. e. from $m_Z > 90$ GeV, where almost no signal events can be found. There, both the $W \rightarrow \tau\nu$ (+jets) and $t\bar{t}$ background are modelled well. Similarly, this behaviour is shown in figure 7.9b, where the overestimation is concentrated in the bin that contains mostly truth-matched signal events, i. e. for a charge sum of zero. The best argument however is discussed in the following section, where the performance of two different generators for $Z \rightarrow \tau\tau$ (+jets) events is compared.

7.6. Identification Scale Factors

To account for the discrepancy between simulated events and data that has been observed in the signal region, a scale factor for the di-tau identification is determined. More specifically, the aim is to measure the deviation in terms of the amount of truth-matched $Z \rightarrow \tau_{\text{had}}\tau_{\text{had}}$ decays. In order to do so, a mass window that isolates the Z mass peak between 40 GeV and 90 GeV is selected. The corresponding event counts are summarized in table 7.3. The scale factor then is given by

$$\text{SF} = \frac{N_{\text{data}} - N_{\text{background}}}{N_{\text{signal}}}, \quad (7.2)$$

where N_{signal} refers to the number of truth-matched $Z \rightarrow \tau_{\text{had}}\tau_{\text{had}}$ decays and

$$N_{\text{background}} = N_{W \rightarrow \tau\nu(+\text{jets})} + N_{t\bar{t}} + N_{\text{Di-boson}} + N_{\text{QCD}} + N_{Z \rightarrow \tau\tau(+\text{jets})}^{\text{non-truth-matched}}. \quad (7.3)$$

Assuming that the event numbers approximately follow a Poisson distribution, the statistical uncertainties in the Z mass window are given by

$$\Delta N_{\text{data}} = \sqrt{N_{\text{data}}} \quad (7.4)$$

7.6. Identification Scale Factors

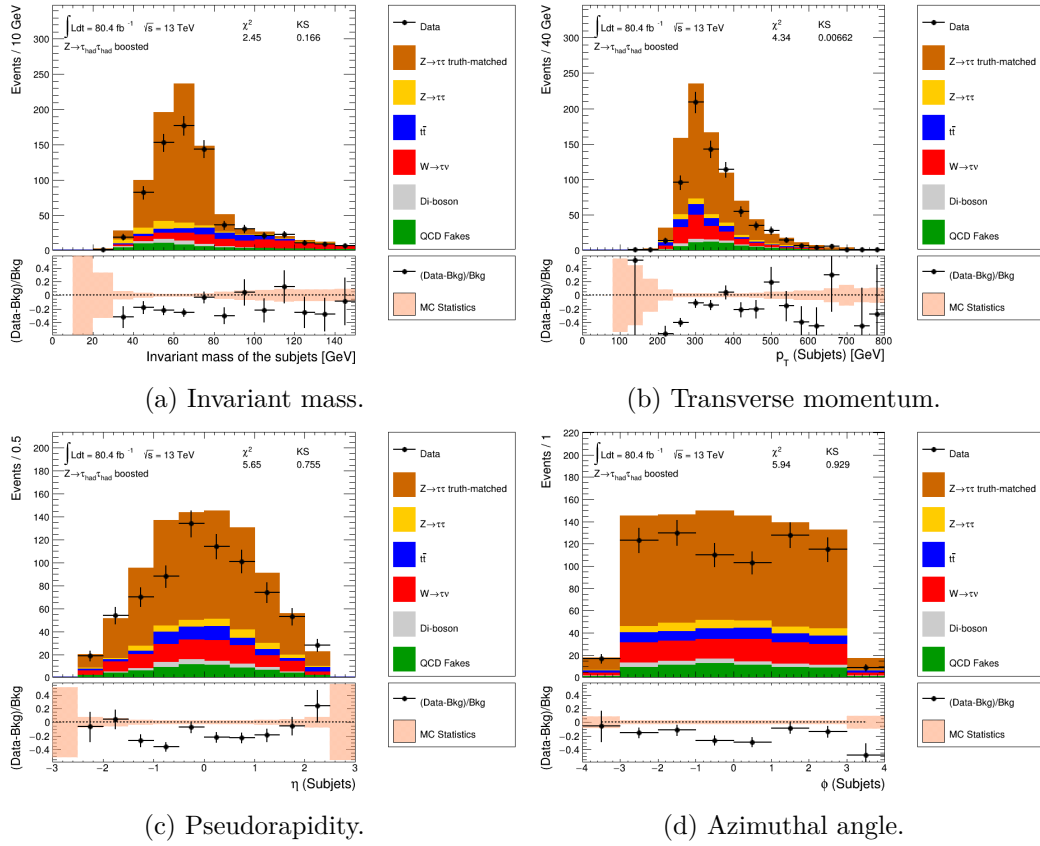


Figure 7.8.: Distributions for the kinematics of the two di-tau subjects, where the full event selection (see section 7.3) has been applied.

7. Validation Studies for Boosted Di-Taus in $Z+\text{jets}$ Events

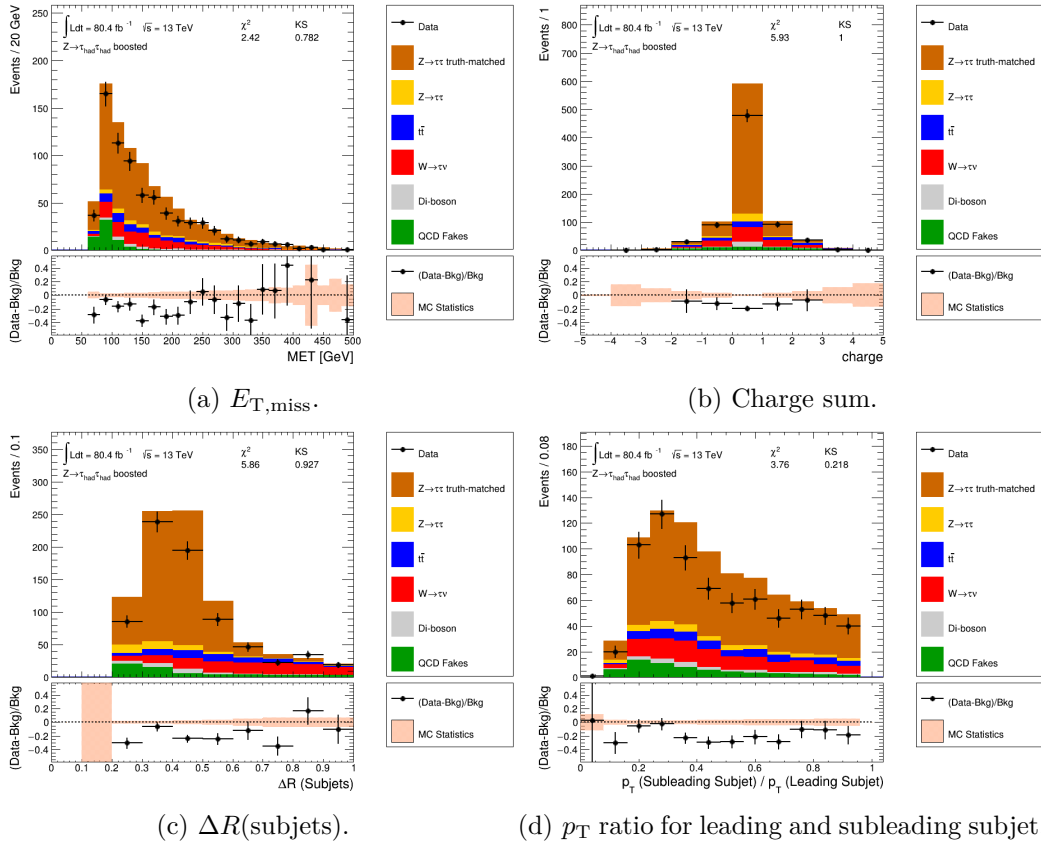


Figure 7.9.: Distributions for event and di-tau related variables, where the full event selection (see section 7.3) has been applied.

for N_{data} unweighted data events and

$$\Delta N_{\text{MC}} = \sqrt{\sum_{i=1}^{N_{\text{MC}}} w_i^2} \quad (7.5)$$

for N_{MC} Monte Carlo events with weights w_i . They are listed in table 7.3 for data and individually for each Monte Carlo sample. Since the event numbers are uncorrelated, their respective uncertainties are propagated via

$$\Delta \text{SF} = \sqrt{\left(\frac{\partial \text{SF}}{\partial N_{\text{data}}}\right)^2 (\Delta N_{\text{data}})^2 + \sum_{\text{MCs}} \left(\frac{\partial \text{SF}}{\partial N_{\text{MC}}}\right)^2 (\Delta N_{\text{MC}})^2} \quad (7.6)$$

and yield a total uncertainty of

$$\Delta \text{SF} = \frac{1}{N_{\text{signal}}} \sqrt{(\Delta N_{\text{data}})^2 + \sum_{\text{backgrounds}} (\Delta N_{\text{background}})^2 + \text{SF}^2 (\Delta N_{\text{signal}})^2}. \quad (7.7)$$

The scale factor for the di-tau identification with respect to truth-matched $Z \rightarrow \tau_{\text{had}} \tau_{\text{had}}$ decays amounts to 0.75 ± 0.05 , and thus is significantly different from one. The effect of its application is evaluated by a comparison between the unscaled (see figure 7.8) and scaled (see figure 7.10) distributions for the di-tau kinematics. In addition, the respective variables for the leading and subleading subjet can be found in figures C.1, C.3 and C.2, C.4. In every distribution, the combined background and signal contributions agree well with the measured data values when the scale factor is applied, except for the transverse momentum of the di-tau subjets in figure 7.10b. This deviation may be resolved by a dedicated energy calibration for boosted di-taus, in particular in the regime where $p_{\text{T}}(\text{di-tau}) < 300 \text{ GeV}$. In conclusion, the scaled histograms confirm the assumption that the discrepancies that have been observed in the previous section are either given by the $Z \rightarrow \tau\tau(+\text{jets})$ Monte Carlo simulation or the di-tau identification.

Table 7.3.: Event yields for the $Z \rightarrow \tau\tau$ mass window ($40 \text{ GeV} < m_Z < 90 \text{ GeV}$), derived from the $Z \rightarrow \tau\tau(+\text{jets})$ Sherpa 2.2.1 samples.

Sample name	Number of events	Statistical uncertainty
Data	592	24(4 %)
$Z \rightarrow \tau_{\text{had}} \tau_{\text{had}}$ truth-matched	557	8(1 %)
$Z \rightarrow \tau\tau(+\text{jets})$ non-truth-matched	31	2(7 %)
$W \rightarrow \tau\nu(+\text{jets})$	52	3(6 %)
$t\bar{t}$	34	4(10 %)
Di-boson	19	1(7 %)
QCD fakes	39.5	0.1(0.1 %)
Data - backgrounds	417	25(6 %)

7. Validation Studies for Boosted Di-Taus in Z +jets Events

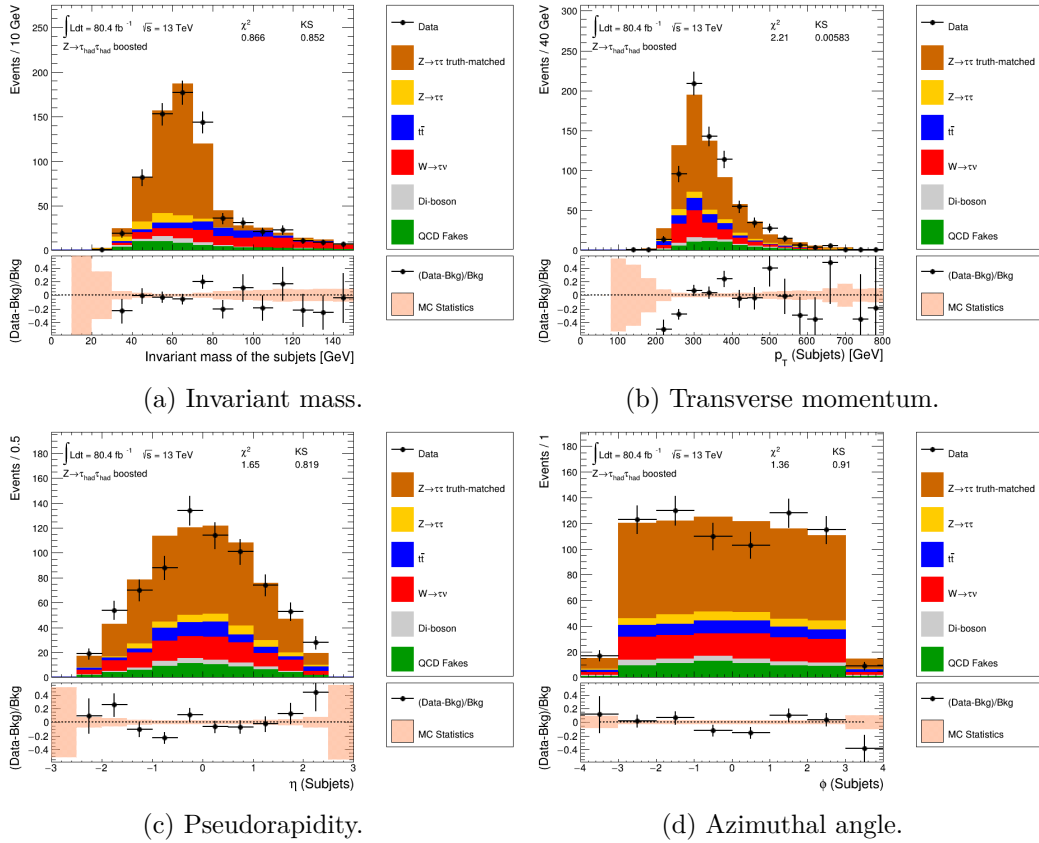


Figure 7.10.: Distributions for the kinematics of the two di-tau subjects after the application of the identification scale factor (0.75) on truth-matched $Z \rightarrow \tau_{\text{had}}\tau_{\text{had}}$ decays.

Comparison with $Z \rightarrow \tau\tau(+\text{jets})$ events generated inclusively with Powheg and Pythia8

The analysis procedure and the scale factor calculation that have been presented up to this point are carried out once more for the $Z \rightarrow \tau\tau(+\text{jets})$ events generated inclusively with Powheg and Pythia8. Accordingly, new fake factors for the QCD fake estimation (see figure 7.11) are derived and applied.

The di-tau kinematics within the signal region are illustrated in figure 7.12. In contrast to the previous distributions, they show a good agreement between data and Monte Carlo, in both shape and normalization. In particular, the QCD background estimation yields an equally good result, indicating that it is somewhat robust in terms of the observed differences in normalization.

The event yields and statistical uncertainties for the determination of the scale factor are summarized in table 7.4. Due to the good agreement between data and signal plus background as well as the larger uncertainty on the number of truth-matched $Z \rightarrow \tau_{\text{had}}\tau_{\text{had}}$ decays, i. e. about 8 % compared to 1 % for Sherpa 2.2.1, the scale factor amounts to 1.0 ± 0.1 , and therefore is compatible with one. Consequently, the overestimation of simulated events as described in the previous sections most likely originates from Sherpa-generated $Z \rightarrow \tau\tau(+\text{jets})$ events, rather than any other Monte Carlo sample.

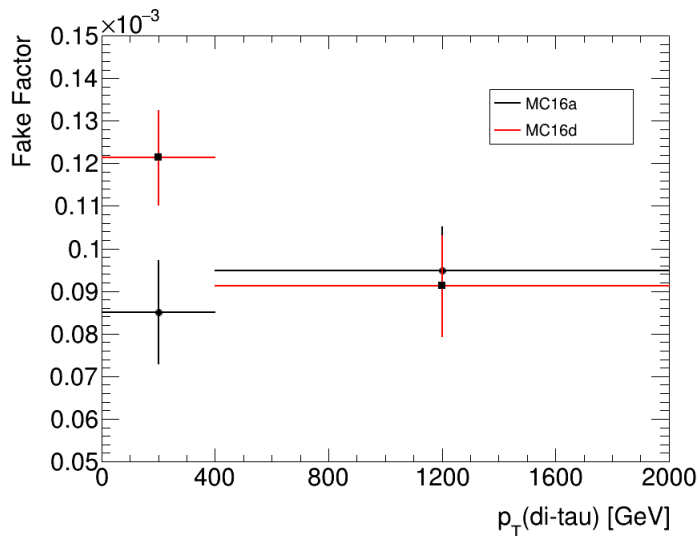


Figure 7.11.: Fake factors for the data-driven QCD background estimation, derived with $Z \rightarrow \tau\tau(+\text{jets})$ events generated with Powheg and Pythia8.

7. Validation Studies for Boosted Di-Taus in Z +jets Events

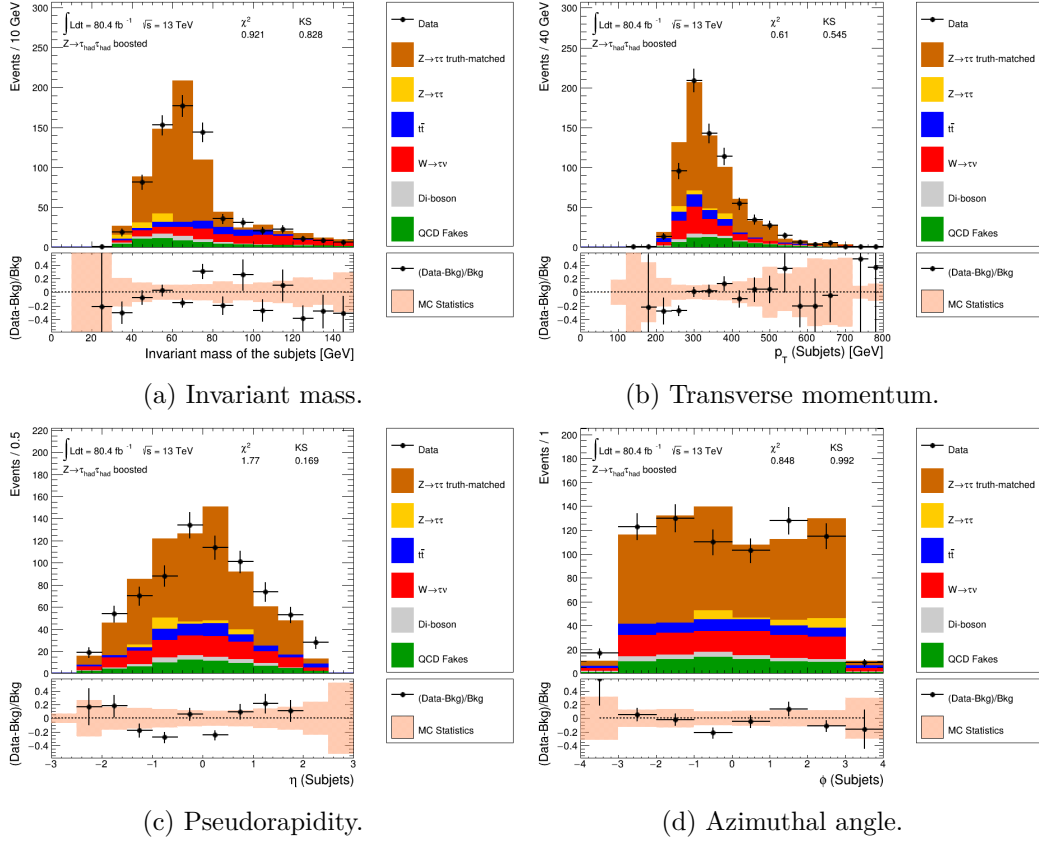


Figure 7.12.: Distributions of the di-tau kinematics in the signal region, taken from the $Z \rightarrow \tau\tau$ (+jets) sample generated with Powheg and Pythia8.

Table 7.4.: Event yields for the $Z \rightarrow \tau\tau$ mass window ($40 \text{ GeV} < m_Z < 90 \text{ GeV}$), derived from the $Z \rightarrow \tau\tau$ (+jets) PowhegPythia8 samples.

Sample name	Number of events	Statistical uncertainty
Data	592	24(4 %)
$Z \rightarrow \tau_{\text{had}}\tau_{\text{had}}$ truth-matched	440	30(8 %)
$Z \rightarrow \tau\tau$ (+jets) non-truth-matched	17	6(36 %)
$W \rightarrow \tau\nu$ (+jets)	52	3(6 %)
$t\bar{t}$	34	4(10 %)
Di-boson	19	1(7 %)
QCD fakes	42.6	0.1(0.2 %)
Data - backgrounds	430	26(6 %)

7.7. $Z \rightarrow \tau\tau(+\text{jets})$ Studies for Semi-Leptonic Di-Tau Decays

To conclude this chapter, some remarks on the possibility of studying the Z mass peak in di-tau decays with an electron or muon in the final state shall be given. As a preliminary step, i. e. before conducting a full analysis, the content of $Z \rightarrow \tau\tau$ decays taken from the inclusively generated Powheg+Pythia8 samples is studied with respect to the two decay modes.

The samples have been processed in the course of the HIGG4D6 dataset derivation (see section 7.1) which is optimized for the $G_{\text{RS}}^{\text{bulk}} \rightarrow \text{hh} \rightarrow \text{bb}\tau\tau$ analysis. The signal topology of this search consists of two high- p_{T} jets, originating from the decay of a boosted pair of b-quarks and tau leptons. According to this expectation, events are not only required to contain at least one reconstructed $\tau_{\text{had}}\tau_{\text{had}}$ di-tau candidate with $p_{\text{T}} > 300$ GeV, but are also skimmed for a minimum of two anti- $k_{\text{t}}(R = 1.0)$ jets with a transverse momentum larger than 300 GeV each.

For the $\tau_{\text{had}}\tau_{\mu}$ channel, this selection rejects almost all signal events from Z boson decays, which is illustrated in figure 7.13a. It depicts the p_{T} -spectra for truth-matched reconstructed di-tau candidates from $Z \rightarrow \tau_{\text{had}}\tau_{\mu}$ before and after the HIGG4D6 jet skimming. Since muons only deposit a very small amount of energy in the calorimeter, most $\tau_{\text{had}}\tau_{\mu}$ candidates do not pass the $p_{\text{T}} = 300$ GeV threshold. Nonetheless, a large amount of them enters the pre-skimming distribution in figure 7.13a, which is most likely explained by a high- p_{T} jet that fakes a fully-hadronic di-tau decay with $p_{\text{T}} > 300$ GeV in the respective event. When no identification requirement is imposed, the recoil system of the boosted Z decay almost always gives a di-tau candidate. Although most $\tau_{\text{had}}\tau_{\mu}$ thus produce one anti- $k_{\text{t}}(R = 1.0)$ jet with sufficient transverse momentum, the second one is lacking in most events.

The p_{T} -distributions for the $\tau_{\text{had}}\tau_{\text{e}}$ mode (see figure 7.13b) show more resemblance to the fully-hadronic channel than those for the $\tau_{\text{had}}\tau_{\mu}$ decays, because in both cases the di-tau reconstruction is seeded by anti- $k_{\text{t}}(R = 1.0)$ jets with $p_{\text{T}} > 300$ GeV. This already excludes di-taus in the low- p_{T} regime. Events with a $\tau_{\text{had}}\tau_{\text{e}}$ candidate thus always contain one sufficiently energetic anti- $k_{\text{t}}(R = 1.0)$ jet and in most cases also a second one from the recoil system.

Throughout the course of this thesis, the new di-tau reconstruction algorithms for the semi-leptonic decay modes (see section 5.2) have been implemented into the analysis framework that is used for the boosted $Z \rightarrow \tau_{\text{had}}\tau_{\text{had}}$ analysis presented in this chapter. From a technical viewpoint, it could therefore be extended to the $Z \rightarrow \tau_{\text{had}}\tau_{\text{e}}$ and $Z \rightarrow \tau_{\text{had}}\tau_{\mu}$ channels. Though due to the limitations set by the dataset derivation this is currently not feasible for $\tau_{\text{had}}\tau_{\mu}$ decays, the $Z \rightarrow \tau_{\text{had}}\tau_{\text{e}}$ search could in principle be attempted. As a first recommendation and rough guideline, a cut selection based on the one described in section 7.3 may be tested. Because the background composition is expected to be similar, i. e. a dominant QCD contribution followed up by $W \rightarrow \tau\nu$, $t\bar{t}$ and perhaps some $W \rightarrow e\nu$ events, this most likely is a reasonable approach.

7. Validation Studies for Boosted Di-Taus in Z+jets Events

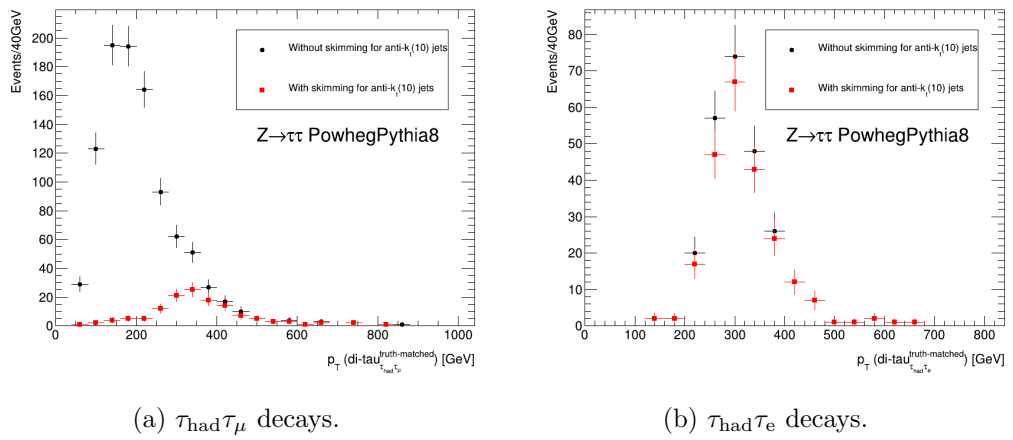


Figure 7.13.: p_T -distribution for truth-matched semi-leptonic di-tau decays, taken from $Z \rightarrow \tau\tau(+\text{jets})$ events generated inclusively with Powheg+Pythia8.

8. Summary

Among the many scenarios trying to go beyond the Standard Model, the Randall-Sundrum model is particularly attractive, both from a theoretical and experimental point of view. While providing a unified description for the well-established electroweak theory and gravity, its prediction of gravitons and their Kaluza-Klein excitations might be within the reach of modern particle colliders, such as the LHC. Accordingly, one of the possible decay channels of the RS graviton, $G_{\text{RS}}^{\text{bulk}} \rightarrow \text{hh} \rightarrow \text{bb}\tau\tau$, provides a sufficiently large branching fraction and a distinct experimental signature that includes a pair of highly boosted tau leptons.

Since the standard tau reconstruction and identification ceases to work when the spatial separation between two tau decays becomes very low, complementary algorithms have been developed, for both fully-hadronic [16] and semi-leptonic [17] di-tau decays. This thesis has studied two means of validating them with events taken from measured data and Monte Carlo samples.

Firstly, for the semi-leptonic di-tau decay modes, systematic uncertainties for the reconstruction and identification efficiencies as well as for the energy scale have been calculated. In both cases, the uncertainties have been derived from $G_{\text{RS}}^{\text{bulk}} \rightarrow \text{hh} \rightarrow 4\tau$ decays with various modifications of the ATLAS detector which have been considered over the course of its simulation. What is more, the kinematics of the di-tau system in the $G_{\text{RS}}^{\text{bulk}} \rightarrow \text{hh} \rightarrow 4\tau$ signal events have been studied. For both semi-leptonic channels, high reconstruction efficiencies of up to about 80%–95% can be achieved in almost all kinematic regions. A significant drop is only observed in two cases: One the one hand, this happens when either of the two tau lepton decays generates visible decay products with a very low p_{T} , i. e. where $p_{\text{T}}(\tau_{\text{had}}^{\text{truth}})$ or $p_{\text{T}}(\ell)$ are smaller than 20 GeV, for which the new reconstruction has not been optimized. Additionally, in the case of di-tau decays with an electron in the final state, the reconstruction is limited by the transverse momentum of the di-tau seed jet, i. e. by $p_{\text{T}}(\text{di-tau}) > 300 \text{ GeV}$, and the overlap between the anti- $k_{\text{t}}(R = 0.2)$ subjet and the energy deposits of the electron. Considering all working points, for $\tau_{\text{had}}\tau_{\text{e}}$ decays the relative efficiency uncertainties amount to 0.5–3% in all kinematic regions, except for the regime where $p_{\text{T}}(\text{di-tau}) < 300 \text{ GeV}$, in which they rise to about 4–6%. In the case of $\tau_{\text{had}}\tau_{\mu}$ decays, values of 0.1–2% are obtained independently of the specific di-tau kinematics. Equally for both semi-leptonic channels, the uncertainties for the di-tau energy scale lie within 0.2–2% for all kinematic regions.

Secondly, fully-hadronic di-tau decays have been studied in 80.4 fb^{-1} of data recorded by the ATLAS detector at $\sqrt{s} = 13 \text{ TeV}$, where the Z boson has served as a benchmark process from the Standard Model. As a starting point for the analysis, the topology of boosted $Z \rightarrow \tau_{\text{had}}\tau_{\text{had}}$ decays with a high- p_{T} hadronic recoil

8. Summary

has been investigated. Based on the result, a strategy to extract the mass peak of the Z boson has been developed. Although the di-tau algorithms already provide a high rejection against fake candidates from QCD, they still pose the largest background contribution immediately after the identification step, only followed by $W \rightarrow \tau\nu$, $t\bar{t}$ and very few di-boson decays. A data-driven estimation for QCD fake candidates has been implemented, which turned out to be fairly robust with regard to the modelling of the remaining Monte Carlo samples. To further suppress the background, several cuts on variables related to the di-tau candidate, the boosted topology and the whole event have been tested. The final selection is both simple and effective, since many analysis have to rely on far more complex cut strategies and yet, in this study, the significance in the signal region is very high. In particular, it allows for the measurement of scale factors for the di-tau identification, from a mass window around the Z peak. The latter have been determined for two different Monte Carlo generators in terms of the $Z \rightarrow \tau\tau(+\text{jets})$ signal process. While for Powheg+Pythia8 the scale factor is compatible with one (1.0 ± 0.1) and thus may be seen as a validation for the di-tau reconstruction and identification, signal events generated with Sherpa 2.2.1 and in the region with zero b-tags on the di-tau seed jet show a significant overestimation compared to data in all considered variables. The corresponding computation of the scale factor yields a value of 0.75 ± 0.05 .

Some first performance studies have been carried out on the Powheg+Pythia8 $Z \rightarrow \tau\tau(+\text{jets})$ signal samples for the semi-leptonic di-tau decay modes. In particular, the impact of the jet skimming applied by the HIGG4D6 dataset derivation has been evaluated, which is optimized for the $G_{\text{RS}}^{\text{bulk}} \rightarrow \text{hh} \rightarrow \text{bb}\tau\tau$ search and accordingly requires at least two high- p_{T} anti- $k_{\text{t}}(R = 1.0)$ jets per event. As a result, the search for boosted $Z \rightarrow \tau_{\text{had}}\tau_{\mu}$ decays has been found to be currently infeasible.

The recently developed reconstruction and identification methods for both semi-leptonic channels [17] have been implemented into the analysis framework that has been used over the course of the $Z \rightarrow \tau_{\text{had}}\tau_{\text{had}}$ study.

9. Outlook

Both the determination of the identification efficiency and energy scale uncertainties for semi-leptonic di-tau decays and the identification scale factors measured around the $Z \rightarrow \tau\tau$ mass peak in the fully-hadronic final state have been completed successfully, and can be handed to the $G_{\text{RS}}^{\text{bulk}} \rightarrow \text{hh} \rightarrow \text{bb}\tau\tau$ analysis. Ultimately, it is the choice of the latter of whether to use the $Z \rightarrow \tau\tau(+\text{jets})$ signal samples that show a good modelling within the context of this thesis, i. e. those generated with PowhegPythia8, or the samples produced with Sherpa 2.2.1, which provide better statistics due to the p_{T} -slicing, though they come with a significant scale factor.

The boosted $Z \rightarrow \tau_{\text{had}}\tau_{\text{had}}$ analysis which has been presented in this thesis may profit substantially from a re-evaluation with the full Run 2 dataset, including an additional integrated luminosity of about 60 fb^{-1} recorded during the 2018 data-taking period. In that case, dedicated background control regions may be found, e. g. for $W \rightarrow \tau\nu$ by selecting an appropriate mass window. Moreover, the scale factor measurement may be refined in terms of different kinematic categories, for example in the transverse momentum or the pseudorapidity of the di-taus.

The set-up for studying the Z mass peak with regard to semi-leptonic di-tau decays has been prepared and tested. Even though the $Z \rightarrow \tau_{\text{had}}\tau_{\mu}$ channel will not be accessible without a new dataset derivation, $Z \rightarrow \tau_{\text{had}}\tau_{\text{e}}$ decays can be analysed on a short timescale. This investigation is very promising, since in terms of signal efficiency and QCD background rejection the semi-leptonic algorithms show results which are equally good as the fully-hadronic ones. It would not only be a valuable test of their performance in an analysis scenario, but may also lead to complementing scale factors for the $G_{\text{RS}}^{\text{bulk}} \rightarrow \text{hh} \rightarrow \text{bb}\tau\tau$ search.

Bibliography

- [1] J. J. Thomson, “Cathode rays”, The London, Edinburgh, and Dublin Philosophical Magazine and Journal of Science **44**, 293 (1897).
- [2] C. D. Anderson, “The Positive Electron”, Phys. Rev. **43**, 491 (1933).
- [3] M. L. Perl et al., “Evidence for anomalous lepton production in e^+e^- annihilation”, Phys. Rev. Lett. **35**, 1489 (1975).
- [4] K. Kodama et al., “Observation of tau neutrino interactions”, Phys. Lett. **B504**, 218 (2001).
- [5] J. Ellis, “The Discovery of the Gluon”, Int. J. Mod. Phys. **A29**, [189(2015)], 1430072 (2014).
- [6] UA1 Collaboration, “Experimental observation of isolated large transverse energy electrons with associated missing energy at $\sqrt{s} = 540$ GeV”, Physics Letters B **122**, 103 (1983).
- [7] UA2 Collaboration, “Observation of single isolated electrons of high transverse momentum in events with missing transverse energy at the CERN pp collider”, Physics Letters B **122**, 476 (1983).
- [8] UA1 Collaboration, “Experimental Observation of Lepton Pairs of Invariant Mass Around 95-GeV/c**2 at the CERN SPS Collider”, Phys. Lett. **B126**, [7.55(1983)], 398 (1983).
- [9] UA2 Collaboration, “Evidence for $Z^0 \rightarrow e^+e^-$ at the CERN anti-p p Collider”, Phys. Lett. **B129**, [7.69(1983)], 130 (1983).
- [10] CDF Collaboration, “Observation of top quark production in $\bar{p}p$ collisions”, Phys. Rev. Lett. **74**, 2626 (1995).
- [11] D0 Collaboration, “Search for high mass top quark production in $p\bar{p}$ collisions at $\sqrt{s} = 1.8$ TeV”, Phys. Rev. Lett. **74**, 2422 (1995).
- [12] ATLAS Collaboration, “Observation of a new particle in the search for the Standard Model Higgs boson with the ATLAS detector at the LHC”, Phys. Lett. **B716**, 1 (2012).
- [13] CMS Collaboration, “Observation of a new boson at a mass of 125 GeV with the CMS experiment at the LHC”, Phys. Lett. **B716**, 30 (2012).
- [14] L. Randall and R. Sundrum, “A Large mass hierarchy from a small extra dimension”, Phys. Rev. Lett. **83**, 3370 (1999).
- [15] L. Randall and R. Sundrum, “An Alternative to compactification”, Phys. Rev. Lett. **83**, 4690 (1999).

Bibliography

- [16] D. Kirchmeier, “Reconstruction and Identification of Boosted Tau Pair Topologies at ATLAS”, MA thesis (Dresden, Tech. U., 2015-05-18).
- [17] C. Wiel, “Reconstruction and Identification of Boosted Di-Tau Decays in the Semi-Leptonic Decay Channel”, MA thesis (Dresden, Tech. U., 2018-05-2).
- [18] C. Quigg, “Electroweak Symmetry Breaking in Historical Perspective”, *Ann. Rev. Nucl. Part. Sci.* **65**, 25 (2015).
- [19] S. L. Glashow, “Partial Symmetries of Weak Interactions”, *Nucl. Phys.* **22**, 579 (1961).
- [20] F. Englert and R. Brout, “Broken symmetry and the mass of gauge vector mesons”, *Phys. Rev. Lett.* **13**, 321 (1964).
- [21] P. W. Higgs, “Broken symmetries and the masses of gauge bosons”, *Phys. Rev. Lett.* **13**, 508 (1964).
- [22] G. S. Guralnik, C. R. Hagen, and T. W. B. Kibble, “Global conservation laws and massless particles”, *Phys. Rev. Lett.* **13**, 585 (1964).
- [23] S. Weinberg, “A model of leptons”, *Phys. Rev. Lett.* **19**, 1264 (1967).
- [24] C. N. Yang and R. L. Mills, “Conservation of isotopic spin and isotopic gauge invariance”, *Phys. Rev.* **96**, 191 (1954).
- [25] W. Pauli, “The connection between spin and statistics”, *Phys. Rev.* **58**, 716 (1940).
- [26] LHCb Collaboration, “Observation of the Resonant Character of the $Z(4430)^-$ State”, *Phys. Rev. Lett.* **112**, 222002 (2014).
- [27] LHCb Collaboration, “Observation of $J/\psi p$ Resonances Consistent with Pentaquark States in $\Lambda_b^0 \rightarrow J/\psi K^- p$ Decays”, *Phys. Rev. Lett.* **115**, 072001 (2015).
- [28] J. Hofstaedt, “Prospects for measuring the neutrino mass hierarchy with ORCA of KM3NeT”, 25th European Cosmic Ray Symposium (ECRS 2016) Turin, Italy, September 04-09, 2016 (2017).
- [29] S. Mertens, “Status of the KATRIN Experiment and Prospects to Search for keV-mass Sterile Neutrinos in Tritium beta-decay”, *Physics Procedia* **61**, 13th International Conference on Topics in Astroparticle and Underground Physics, TAUP 2013, 267 (2015).
- [30] C. S. Wu, E. Ambler, R. W. Hayward, D. D. Hoppes, and R. P. Hudson, “Experimental test of parity conservation in beta decay”, *Phys. Rev.* **105**, 1413 (1957).
- [31] S. H. Neddermeyer and C. D. Anderson, “Note on the nature of cosmic-ray particles”, *Phys. Rev.* **51**, 884 (1937).
- [32] ATLAS Collaboration, “Observation of electroweak production of a same-sign W boson pair in association with two jets in pp collisions at $\sqrt{s} = 13$ TeV with the ATLAS detector”, ATLAS-CONF-2018-030 (2018).

- [33] ATLAS Collaboration, “Observation of electroweak $W^\pm Z$ boson pair production in association with two jets in pp collisions at $\sqrt{s} = 13\text{TeV}$ with the ATLAS Detector”, ATLAS-CONF-2018-033 (2018).
- [34] S. Dittmaier and M. Schumacher, “The Higgs boson in the Standard Model-From LEP to LHC: Expectations, Searches, and Discovery of a Candidate”, Progress in Particle and Nuclear Physics **70**, 1 (2013).
- [35] Y. Tang, “Vacuum Stability in the Standard Model”, Mod. Phys. Lett. **A28**, 1330002 (2013).
- [36] M. Tanabashi et al. (Particle Data Group), “2018 Review of Particle Physics”, Phys. Rev. D **98** (2018).
- [37] A. M. Sirunyan et al., “Measurement of the weak mixing angle using the forward-backward asymmetry of Drell-Yan events in pp collisions at 8 TeV”, (2018).
- [38] S. Schael et al., “Precision electroweak measurements on the Z resonance”, Phys. Rept. **427**, 257 (2006).
- [39] S. D. Drell and T.-M. Yan, “Massive lepton-pair production in hadron-hadron collisions at high energies”, Phys. Rev. Lett. **25**, 316 (1970).
- [40] ATLAS Collaboration, “Measurement of the low-mass Drell-Yan differential cross section at $\sqrt{s} = 7\text{ TeV}$ using the ATLAS detector”, JHEP **06**, 112 (2014).
- [41] ATLAS Collaboration, “Measurement of the double-differential high-mass Drell-Yan cross section in pp collisions at $\sqrt{s} = 8\text{ TeV}$ with the ATLAS detector”, JHEP **08**, 009 (2016).
- [42] ATLAS Collaboration, “Measurement of the Drell-Yan triple-differential cross section in pp collisions at $\sqrt{s} = 8\text{ TeV}$ ”, JHEP **12**, 059 (2017).
- [43] ATLAS Collaboration, “Prospects for the measurement of the rare Higgs boson decay $H \rightarrow \mu\mu$ with 3000 fb^{-1} of pp collisions collected at $\sqrt{s} = 14\text{ TeV}$ by the ATLAS experiment”, (2018).
- [44] CMS Collaboration, “Observation of the Higgs boson decay to a pair of τ leptons with the CMS detector”, Phys. Lett. **B779**, 283 (2018).
- [45] ATLAS collaboration, “Search for new high-mass phenomena in the dilepton final state using 36.1 fb^{-1} of proton-proton collision data at $\sqrt{s} = 13\text{ TeV}$ with the ATLAS detector”, (2017).
- [46] ATLAS Collaboration, “Identification and energy calibration of hadronically decaying tau leptons with the ATLAS experiment in pp collisions at $\sqrt{s}=8\text{ TeV}$ ”, Eur. Phys. J. **C75**, 303 (2015).
- [47] N. Arkani-Hamed, S. Dimopoulos, and G. R. Dvali, “The Hierarchy problem and new dimensions at a millimeter”, Phys. Lett. **B429**, 263 (1998).

Bibliography

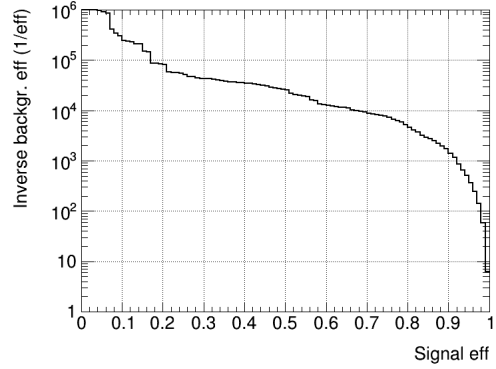
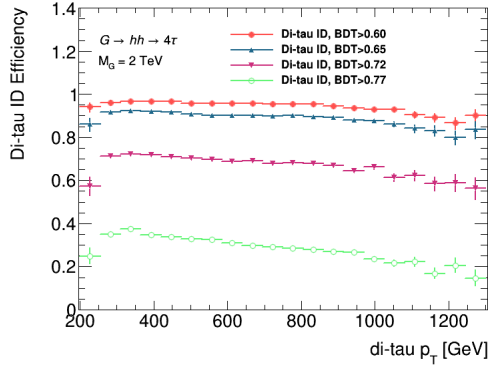
- [48] W. D. Goldberger and M. B. Wise, “Modulus stabilization with bulk fields”, *Phys. Rev. Lett.* **83**, 4922 (1999).
- [49] A. Oliveira, “Gravity particles from Warped Extra Dimensions, predictions for LHC”, (2014).
- [50] ATLAS Collaboration, “Searches for heavy diboson resonances in pp collisions at $\sqrt{s} = 13$ TeV with the ATLAS detector”, *JHEP* **09**, 173 (2016).
- [51] CMS Collaboration, “Search for ZZ resonances in the $2\ell 2\nu$ final state in proton-proton collisions at 13 TeV”, *JHEP* **03**, 003 (2018).
- [52] L. Evans and P. Bryant, “LHC Machine”, *JINST* **3**, S08001 (2008).
- [53] O. S. Bruning, P. Collier, P. Lebrun, S. Myers, R. Ostojic, J. Poole, and P. Proudlock, “LHC Design Report Vol.1: The LHC Main Ring”, (2004).
- [54] ATLAS Collaboration, “The ATLAS Experiment at the CERN Large Hadron Collider”, *JINST* **3**, S08003 (2008).
- [55] CMS Collaboration, “The CMS Experiment at the CERN LHC”, *JINST* **3**, S08004 (2008).
- [56] LHCb Collaboration, “The LHCb Detector at the LHC”, *JINST* **3**, S08005 (2008).
- [57] ALICE Collaboration, “The ALICE experiment at the CERN LHC”, *JINST* **3**, S08002 (2008).
- [58] T. Schörner-Sadenius, “The Large Hadron Collider”, Springer, Berlin (2015).
- [59] J. Pequeno, “Computer generated image of the whole ATLAS detector”, CERN Document Server, Mar. 2008.
- [60] L. Scodellaro, “B tagging in ATLAS and CMS”, in 5th Large Hadron Collider Physics Conference (LHCP 2017) Shanghai, China, May 15-20, 2017 (2017).
- [61] A. La Rosa, “The ATLAS Insertable B-Layer: From construction to operation”, *JINST* **11**, C12036 (2016).
- [62] ATLAS Collaboration, “Performance of the ATLAS Track Reconstruction Algorithms in Dense Environments in LHC Run 2”, *Eur. Phys. J.* **C77**, 673 (2017).
- [63] N. Nikiforou, “Performance of the ATLAS Liquid Argon Calorimeter after three years of LHC operation and plans for a future upgrade”, in Proceedings, 3rd International Conference on Advancements in Nuclear Instrumentation Measurement Methods and their Applications (ANIMMA 2013): Marseille, France, June 23-27, 2013 (2013).
- [64] ATLAS Collaboration, “ATLAS liquid argon calorimeter: Technical design report”, (1996).
- [65] ATLAS Collaboration, “ATLAS tile calorimeter: Technical Design Report”, Technical Design Report ATLAS (1996).

- [66] J. Pequenaio, “Computer Generated image of the ATLAS calorimeter”, CERN Document Server, Mar. 2008.
- [67] ATLAS Collaboration, “ATLAS muon spectrometer: Technical design report”, (1997).
- [68] J. Pequenaio, “Computer generated image of the ATLAS Muons subsystem”, CERN Document Server, Mar. 2008.
- [69] Y. Nakahama, “The ATLAS Trigger System: Ready for Run-2”, J. Phys. Conf. Ser. **664**, 082037 (2015).
- [70] ATLAS Collaboration, “An imaging algorithm for vertex reconstruction for ATLAS Run-2”, (2015).
- [71] W. Lampl, S. Laplace, D. Lelas, P. Loch, H. Ma, S. Menke, S. Rajagopalan, D. Rousseau, S. Snyder, and G. Unal, “Calorimeter clustering algorithms: Description and performance”, (2008).
- [72] ATLAS collaboration, “Electron efficiency measurements with the ATLAS detector using the 2015 LHC proton-proton collision data”, (2016).
- [73] ATLAS Collaboration, “Improved electron reconstruction in ATLAS using the Gaussian Sum Filter-based model for bremsstrahlung”, (2012).
- [74] ATLAS Collaboration, “Electron and photon energy calibration with the ATLAS detector using data collected in 2015 at $\sqrt{s} = 13$ TeV”, ATL-PHYS-PUB-2016-015 (2016).
- [75] ATLAS Collaboration, “Measurement of the differential cross-sections of prompt and non-prompt production of J/ψ and $\psi(2S)$ in pp collisions at $\sqrt{s} = 7$ and 8 TeV with the ATLAS detector”, Eur. Phys. J. **C76**, 283 (2016).
- [76] ATLAS Collaboration, “Muon reconstruction performance of the ATLAS detector in proton-proton collision data at $\sqrt{s} = 13$ TeV”, Eur. Phys. J. **C76**, 292 (2016).
- [77] R. Atkin, “Review of jet reconstruction algorithms”, J. Phys. Conf. Ser. **645**, 012008 (2015).
- [78] M. Cacciari, G. P. Salam, and G. Soyez, “The anti- k_t jet clustering algorithm”, JHEP **04**, 063 (2008).
- [79] ATLAS Collaboration, “Topological cell clustering in the ATLAS calorimeters and its performance in LHC Run 1”, Eur. Phys. J. **C77**, 490 (2017).
- [80] ATLAS Collaboration, “Jet energy scale measurements and their systematic uncertainties in proton-proton collisions at $\sqrt{s} = 13$ TeV with the ATLAS detector”, Phys. Rev. **D96**, 072002 (2017).
- [81] ATLAS Collaboration, “Measurement of the tau lepton reconstruction and identification performance in the ATLAS experiment using pp collisions at $\sqrt{s} = 13$ TeV”, (2017).

- [82] ATLAS Collaboration, “Performance of missing transverse momentum reconstruction with the ATLAS detector using proton-proton collisions at $\sqrt{s} = 13$ TeV”, (2018).
- [83] D. Duschinger, “Search for neutral bosons beyond the Standard Model decaying into tau leptons using the ATLAS detector at the LHC”, In preparation., PhD thesis (TU Dresden, 2018).
- [84] D. Kirchmeier, “Search for new physics in boosted $hh \rightarrow bb\tau\tau$ decays at ATLAS”, in DPG Fruehjahrstagung, Wuerzburg (2018).
- [85] Simulation Infrastructure, “The ATLAS Simulation Infrastructure”, Eur. Phys. J. **C70**, 823 (2010).
- [86] J. Alwall, R. Frederix, S. Frixione, V. Hirschi, F. Maltoni, O. Mattelaer, H. -.-S. Shao, T. Stelzer, P. Torrielli, and M. Zaro, “The automated computation of tree-level and next-to-leading order differential cross sections, and their matching to parton shower simulations”, JHEP **07**, 079 (2014).
- [87] T. Sjostrand, S. Mrenna, and P. Z. Skands, “A Brief Introduction to PYTHIA 8.1”, Comput. Phys. Commun. **178**, 852 (2008).
- [88] ATLAS Collaboration, “ATLAS Run 1 Pythia8 tunes”, (2014).
- [89] NNPDF Collaboration, “Parton distributions with LHC data”, Nucl. Phys. **B867**, 244 (2013).
- [90] D. J. Lange, “The EvtGen particle decay simulation package”, Nucl. Instrum. Meth. **A462**, 152 (2001).
- [91] S. Agostinelli et al., “GEANT4: A Simulation toolkit”, Nucl. Instrum. Meth. **A506**, 250 (2003).
- [92] M. Asai, A. Dotti, M. Verderi, and D. H. Wright, “Recent developments in Geant4”, Annals Nucl. Energy **82**, 19 (2015).
- [93] GEANT4 Collaboration, “Guide for physics lists”, Release 10.4 (2017).
- [94] S. Alioli, P. Nason, C. Oleari, and E. Re, “A general framework for implementing NLO calculations in shower Monte Carlo programs: the POWHEG BOX”, JHEP **06**, 043 (2010).
- [95] T. Gleisberg, S. Hoeche, F. Krauss, M. Schonherr, S. Schumann, F. Siegert, and J. Winter, “Event generation with SHERPA 1.1”, JHEP **02**, 007 (2009).
- [96] ATLAS collaboration, “Implementation of the ATLAS Run 2 event data model”, J. Phys.: Conf. Ser. 664 (2015) 072045 (2015).
- [97] R. Brun and F. Rademacher, “ROOT — An object oriented data analysis framework”, Nuclear Instruments and Methods in Physics Research Section A: Accelerators, Spectrometers, Detectors and Associated Equipment **389**, 81 (1997).
- [98] ATLAS Collaboration, “Luminosity Public Results Run 2”, visited on 8th of December, 2018.

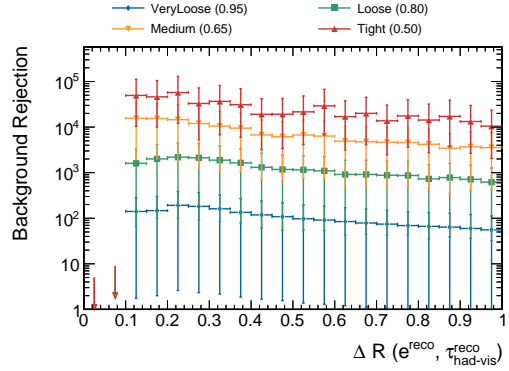
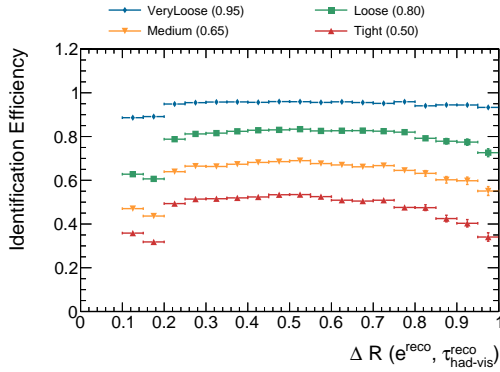
- [99] G. Cowan, K. Cranmer, E. Gross, and O. Vitells, “Asymptotic formulae for likelihood-based tests of new physics”, *Eur. Phys. J.* **C71**, [Erratum: *Eur. Phys. J.*C73,2501(2013)], 1554 (2011).
- [100] M. Owen, “Top quark properties measurements at the LHC”, in *Proceedings, 52nd Rencontres de Moriond on Electroweak Interactions and Unified Theories: La Thuile, Italy, March 18-25, 2017* (2017), pp. 25–32.

A. Performance Plots for the Boosted Di-Tau Algorithms



(a) Identification efficiencies for the VeryLoose, Loose, Medium and Tight working points with respect to the di-tau p_T . (b) Background rejection versus signal efficiency.

Figure A.1.: Performance plots for the $\tau_{\text{had}}\tau_{\text{had}}$ decay channel ([16]).



(a) Identification efficiencies for the VeryLoose, Loose, Medium and Tight working points with respect to $\Delta R(\tau_{\text{had}}, e)$. (b) Background rejection versus $\Delta R(\tau_{\text{had}}, e)$.

Figure A.2.: Performance plots for the $\tau_{\text{had}}\tau_e$ decay channel ([17]).

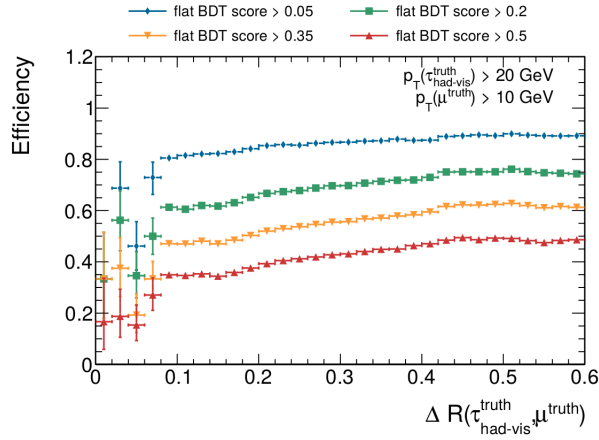
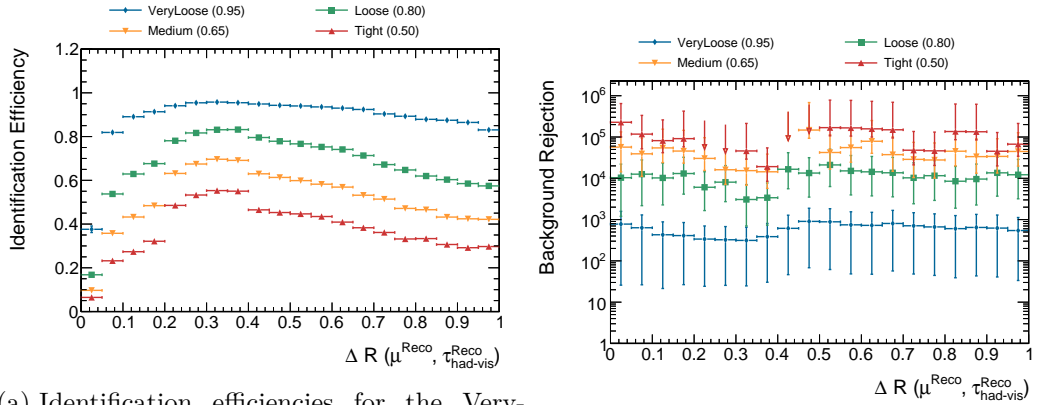


Figure A.3.: Identification efficiencies for $\tau_{\text{had}}\tau_{\mu}$ candidates which have been corrected for the muon track and propagated through the standard tau and muon algorithms with respect to $\Delta R(\tau_{\text{had}}, \mu)$. The cuts in the flat BDT score correspond to the standard tau identification ([17]).



(a) Identification efficiencies for the VeryLoose, Loose, Medium and Tight working points with respect to $\Delta R(\tau_{\text{had}}, \mu)$. (b) Background rejection versus $\Delta R(\tau_{\text{had}}, \mu)$.

Figure A.4.: Performance plots for the $\tau_{\text{had}}\tau_{\mu}$ decay channel with the newly trained identification ([17]).

B. Data and Monte Carlo Samples

B.1. Graviton Signal Samples

Table B.1.: Monte Carlo samples for $G \rightarrow hh \rightarrow 4\tau$ with $M_G = 1\dots 5\text{GeV}$.

Systematic Variation	Sample name
Nominal	mc16_13TeV.425104.MadGraphPythia8EvtGen_A14NNPDF23LO_RS_G_hh_4tau_c10_M2500.merge.AOD.e5485_s3126_r9364_r9315
	mc16_13TeV.425102.MadGraphPythia8EvtGen_A14NNPDF23LO_RS_G_hh_4tau_c10_M2000.merge.AOD.e5485_s3126_r9364_r9315
	mc16_13TeV.425100.MadGraphPythia8EvtGen_A14NNPDF23LO_RS_G_hh_4tau_c10_M1500.merge.AOD.e5485_s3126_r9364_r9315
	mc16_13TeV.425107.MadGraphPythia8EvtGen_A14NNPDF23LO_RS_G_hh_4tau_c10_M5000.merge.AOD.e6072_s3126_r9364_r9315
	mc16_13TeV.425105.MadGraphPythia8EvtGen_A14NNPDF23LO_RS_G_hh_4tau_c10_M3000.merge.AOD.e6072_s3126_r9364_r9315
	mc16_13TeV.425106.MadGraphPythia8EvtGen_A14NNPDF23LO_RS_G_hh_4tau_c10_M4000.merge.AOD.e6072_s3126_r9364_r9315
	mc16_13TeV.425101.MadGraphPythia8EvtGen_A14NNPDF23LO_RS_G_hh_4tau_c10_M1750.merge.AOD.e5485_s3126_r9364_r9315
	mc16_13TeV.425103.MadGraphPythia8EvtGen_A14NNPDF23LO_RS_G_hh_4tau_c10_M2250.merge.AOD.e5485_s3126_r9364_r9315
	mc16_13TeV.425108.MadGraphPythia8EvtGen_A14NNPDF23LO_RS_G_hh_4tau_c10_M1000.merge.AOD.e6072_s3126_r9364_r9315
ALT_GEO	mc16_13TeV.425100.MadGraphPythia8EvtGen_A14NNPDF23LO_RS_G_hh_4tau_c10_M1500.merge.AOD.e5485_s3156_r9477_r9315
	mc16_13TeV.425101.MadGraphPythia8EvtGen_A14NNPDF23LO_RS_G_hh_4tau_c10_M1750.merge.AOD.e5485_s3156_r9477_r9315
	mc16_13TeV.425103.MadGraphPythia8EvtGen_A14NNPDF23LO_RS_G_hh_4tau_c10_M2250.merge.AOD.e5485_s3156_r9477_r9315
	mc16_13TeV.425102.MadGraphPythia8EvtGen_A14NNPDF23LO_RS_G_hh_4tau_c10_M2000.merge.AOD.e5485_s3156_r9477_r9315
	mc16_13TeV.425104.MadGraphPythia8EvtGen_A14NNPDF23LO_RS_G_hh_4tau_c10_M2500.merge.AOD.e5485_s3156_r9477_r9315
	mc16_13TeV.425105.MadGraphPythia8EvtGen_A14NNPDF23LO_RS_G_hh_4tau_c10_M3000.merge.AOD.e6072_s3156_r9477_r9315
	mc16_13TeV.425106.MadGraphPythia8EvtGen_A14NNPDF23LO_RS_G_hh_4tau_c10_M4000.merge.AOD.e6072_s3156_r9477_r9315
	mc16_13TeV.425107.MadGraphPythia8EvtGen_A14NNPDF23LO_RS_G_hh_4tau_c10_M5000.merge.AOD.e6072_s3156_r9477_r9315
	mc16_13TeV.425108.MadGraphPythia8EvtGen_A14NNPDF23LO_RS_G_hh_4tau_c10_M1000.merge.AOD.e6072_s3156_r9477_r9315
IBL_30	mc16_13TeV.425100.MadGraphPythia8EvtGen_A14NNPDF23LO_RS_G_hh_4tau_c10_M1500.merge.AOD.e5485_s3157_r9478_r9315
	mc16_13TeV.425101.MadGraphPythia8EvtGen_A14NNPDF23LO_RS_G_hh_4tau_c10_M1750.merge.AOD.e5485_s3157_r9478_r9315
	mc16_13TeV.425102.MadGraphPythia8EvtGen_A14NNPDF23LO_RS_G_hh_4tau_c10_M2000.merge.AOD.e5485_s3157_r9478_r9315
	mc16_13TeV.425103.MadGraphPythia8EvtGen_A14NNPDF23LO_RS_G_hh_4tau_c10_M2250.merge.AOD.e5485_s3157_r9478_r9315
	mc16_13TeV.425104.MadGraphPythia8EvtGen_A14NNPDF23LO_RS_G_hh_4tau_c10_M2500.merge.AOD.e5485_s3157_r9478_r9315
	mc16_13TeV.425105.MadGraphPythia8EvtGen_A14NNPDF23LO_RS_G_hh_4tau_c10_M3000.merge.AOD.e6072_s3157_r9478_r9315
	mc16_13TeV.425106.MadGraphPythia8EvtGen_A14NNPDF23LO_RS_G_hh_4tau_c10_M4000.merge.AOD.e6072_s3157_r9478_r9315
	mc16_13TeV.425107.MadGraphPythia8EvtGen_A14NNPDF23LO_RS_G_hh_4tau_c10_M5000.merge.AOD.e6072_s3157_r9478_r9315
	mc16_13TeV.425108.MadGraphPythia8EvtGen_A14NNPDF23LO_RS_G_hh_4tau_c10_M1000.merge.AOD.e6072_s3157_r9478_r9315
PP0_50	mc16_13TeV.425100.MadGraphPythia8EvtGen_A14NNPDF23LO_RS_G_hh_4tau_c10_M1500.merge.AOD.e5485_s3169_r9552_r9315
	mc16_13TeV.425101.MadGraphPythia8EvtGen_A14NNPDF23LO_RS_G_hh_4tau_c10_M1750.merge.AOD.e5485_s3169_r9552_r9315
	mc16_13TeV.425102.MadGraphPythia8EvtGen_A14NNPDF23LO_RS_G_hh_4tau_c10_M2000.merge.AOD.e5485_s3169_r9552_r9315
	mc16_13TeV.425103.MadGraphPythia8EvtGen_A14NNPDF23LO_RS_G_hh_4tau_c10_M2250.merge.AOD.e5485_s3169_r9552_r9315
	mc16_13TeV.425104.MadGraphPythia8EvtGen_A14NNPDF23LO_RS_G_hh_4tau_c10_M2500.merge.AOD.e5485_s3169_r9552_r9315
	mc16_13TeV.425105.MadGraphPythia8EvtGen_A14NNPDF23LO_RS_G_hh_4tau_c10_M3000.merge.AOD.e6072_s3169_r9552_r9315
mc16_13TeV.425106.MadGraphPythia8EvtGen_A14NNPDF23LO_RS_G_hh_4tau_c10_M4000.merge.AOD.e6072_s3169_r9552_r9315	

Table B.1.: Monte Carlo samples for $G \rightarrow hh \rightarrow 4\tau$ with $M_G = 1\dots 5\text{GeV}$.

Systematic Variation	Sample name
	mc16_13TeV.425107.MadGraphPythia8EvtGen_A14NNPDF23LO_RS_G_hh_4tau_c10_M5000.merge.AOD.e6072_s3169_r9552_r9315
	mc16_13TeV.425108.MadGraphPythia8EvtGen_A14NNPDF23LO_RS_G_hh_4tau_c10_M1000.merge.AOD.e6072_s3169_r9552_r9315
	mc16_13TeV.425100.MadGraphPythia8EvtGen_A14NNPDF23LO_RS_G_hh_4tau_c10_M1500.merge.AOD.e5485_s3155_r9476_r9315
	mc16_13TeV.425101.MadGraphPythia8EvtGen_A14NNPDF23LO_RS_G_hh_4tau_c10_M1750.merge.AOD.e5485_s3155_r9476_r9315
	mc16_13TeV.425102.MadGraphPythia8EvtGen_A14NNPDF23LO_RS_G_hh_4tau_c10_M2000.merge.AOD.e5485_s3155_r9476_r9315
	mc16_13TeV.425103.MadGraphPythia8EvtGen_A14NNPDF23LO_RS_G_hh_4tau_c10_M2250.merge.AOD.e5485_s3155_r9476_r9315
QGSP_BIC	mc16_13TeV.425104.MadGraphPythia8EvtGen_A14NNPDF23LO_RS_G_hh_4tau_c10_M2500.merge.AOD.e5485_s3155_r9476_r9315
	mc16_13TeV.425105.MadGraphPythia8EvtGen_A14NNPDF23LO_RS_G_hh_4tau_c10_M3000.merge.AOD.e6072_s3155_r9476_r9315
	mc16_13TeV.425106.MadGraphPythia8EvtGen_A14NNPDF23LO_RS_G_hh_4tau_c10_M4000.merge.AOD.e6072_s3155_r9476_r9315
	mc16_13TeV.425107.MadGraphPythia8EvtGen_A14NNPDF23LO_RS_G_hh_4tau_c10_M5000.merge.AOD.e6072_s3155_r9476_r9315
	mc16_13TeV.425108.MadGraphPythia8EvtGen_A14NNPDF23LO_RS_G_hh_4tau_c10_M1000.merge.AOD.e6072_s3155_r9476_r9315

Table B.2.: $G \rightarrow hh \rightarrow 4\tau$ mass slices and number of events.

M_G in TeV	Number of events		
	Nominal	ALT_GEO / IBL_30 / PP0_50	QGSP_BIC
1.00	193000	200000	200000
1.50	200000	200000	199000
1.75	200000	200000	199500
2.00	200000	200000	200000
2.25	200000	200000	199500
2.50	200000	200000	199500
3.00	100000	100000	100000
4.00	100000	100000	100000
5.00	99000	100000	100000

B.2. Samples for the Z+jets Validation Studies

Table B.4.: Data samples from 2015 data taking.

Data 2015
data15_13TeV.00278970.physics_Main.deriv.DAOD_HIGG4D6.r9264_p3083_p3416
data15_13TeV.00280319.physics_Main.deriv.DAOD_HIGG4D6.r9264_p3083_p3416
data15_13TeV.00276336.physics_Main.deriv.DAOD_HIGG4D6.r9264_p3083_p3416
data15_13TeV.00278727.physics_Main.deriv.DAOD_HIGG4D6.r9264_p3083_p3416
data15_13TeV.00280753.physics_Main.deriv.DAOD_HIGG4D6.r9264_p3083_p3416
data15_13TeV.00284484.physics_Main.deriv.DAOD_HIGG4D6.r9264_p3083_p3416
data15_13TeV.00280368.physics_Main.deriv.DAOD_HIGG4D6.r9264_p3083_p3416
data15_13TeV.00279764.physics_Main.deriv.DAOD_HIGG4D6.r9264_p3083_p3416
data15_13TeV.00281143.physics_Main.deriv.DAOD_HIGG4D6.r9264_p3083_p3416
data15_13TeV.00276329.physics_Main.deriv.DAOD_HIGG4D6.r9264_p3083_p3416
data15_13TeV.00278912.physics_Main.deriv.DAOD_HIGG4D6.r9264_p3083_p3416
data15_13TeV.00281411.physics_Main.deriv.DAOD_HIGG4D6.r9264_p3083_p3416
data15_13TeV.00280614.physics_Main.deriv.DAOD_HIGG4D6.r9264_p3083_p3416
data15_13TeV.00284420.physics_Main.deriv.DAOD_HIGG4D6.r9264_p3083_p3416
data15_13TeV.00280950.physics_Main.deriv.DAOD_HIGG4D6.r9264_p3083_p3416
data15_13TeV.00279515.physics_Main.deriv.DAOD_HIGG4D6.r9264_p3083_p3416
data15_13TeV.00283608.physics_Main.deriv.DAOD_HIGG4D6.r9264_p3083_p3416
data15_13TeV.00279685.physics_Main.deriv.DAOD_HIGG4D6.r9264_p3083_p3416
data15_13TeV.00280464.physics_Main.deriv.DAOD_HIGG4D6.r9264_p3083_p3416
data15_13TeV.00279169.physics_Main.deriv.DAOD_HIGG4D6.r9264_p3083_p3416

Table B.4.: Data samples from 2015 data taking.

Data 2015	
data15_13TeV.00279984.physics_Main.deriv.DAOD_HIGG4D6.r9264_p3083_p3416	
data15_13TeV.00278880.physics_Main.deriv.DAOD_HIGG4D6.r9264_p3083_p3416	
data15_13TeV.00283074.physics_Main.deriv.DAOD_HIGG4D6.r9264_p3083_p3416	
data15_13TeV.00278748.physics_Main.deriv.DAOD_HIGG4D6.r9264_p3083_p3416	
data15_13TeV.00276952.physics_Main.deriv.DAOD_HIGG4D6.r9264_p3083_p3416	
data15_13TeV.00279813.physics_Main.deriv.DAOD_HIGG4D6.r9264_p3083_p3416	
data15_13TeV.00279928.physics_Main.deriv.DAOD_HIGG4D6.r9264_p3083_p3416	
data15_13TeV.00276790.physics_Main.deriv.DAOD_HIGG4D6.r9264_p3083_p3416	
data15_13TeV.00281381.physics_Main.deriv.DAOD_HIGG4D6.r9264_p3083_p3416	
data15_13TeV.00280520.physics_Main.deriv.DAOD_HIGG4D6.r9264_p3083_p3416	
data15_13TeV.00280853.physics_Main.deriv.DAOD_HIGG4D6.r9264_p3083_p3416	
data15_13TeV.00283780.physics_Main.deriv.DAOD_HIGG4D6.r9264_p3083_p3416	
data15_13TeV.00281074.physics_Main.deriv.DAOD_HIGG4D6.r9264_p3083_p3416	
data15_13TeV.00278968.physics_Main.deriv.DAOD_HIGG4D6.r9264_p3083_p3416	
data15_13TeV.00279932.physics_Main.deriv.DAOD_HIGG4D6.r9264_p3083_p3416	
data15_13TeV.00282625.physics_Main.deriv.DAOD_HIGG4D6.r9264_p3083_p3416	
data15_13TeV.00283270.physics_Main.deriv.DAOD_HIGG4D6.r9264_p3083_p3416	
data15_13TeV.00276330.physics_Main.deriv.DAOD_HIGG4D6.r9264_p3083_p3416	
data15_13TeV.00276262.physics_Main.deriv.DAOD_HIGG4D6.r9264_p3083_p3416	
data15_13TeV.00279279.physics_Main.deriv.DAOD_HIGG4D6.r9264_p3083_p3416	
data15_13TeV.00284154.physics_Main.deriv.DAOD_HIGG4D6.r9264_p3083_p3416	
data15_13TeV.00282712.physics_Main.deriv.DAOD_HIGG4D6.r9264_p3083_p3416	
data15_13TeV.00280273.physics_Main.deriv.DAOD_HIGG4D6.r9264_p3083_p3416	
data15_13TeV.00284213.physics_Main.deriv.DAOD_HIGG4D6.r9264_p3083_p3416	
data15_13TeV.00281385.physics_Main.deriv.DAOD_HIGG4D6.r9264_p3083_p3416	
data15_13TeV.00283429.physics_Main.deriv.DAOD_HIGG4D6.r9264_p3083_p3416	
data15_13TeV.00280231.physics_Main.deriv.DAOD_HIGG4D6.r9264_p3083_p3416	
data15_13TeV.00280862.physics_Main.deriv.DAOD_HIGG4D6.r9264_p3083_p3416	
data15_13TeV.00280500.physics_Main.deriv.DAOD_HIGG4D6.r9264_p3083_p3416	
data15_13TeV.00276689.physics_Main.deriv.DAOD_HIGG4D6.r9264_p3083_p3416	
data15_13TeV.00283155.physics_Main.deriv.DAOD_HIGG4D6.r9264_p3083_p3416	
data15_13TeV.00281070.physics_Main.deriv.DAOD_HIGG4D6.r9264_p3083_p3416	
data15_13TeV.00276731.physics_Main.deriv.DAOD_HIGG4D6.r9264_p3083_p3416	
data15_13TeV.00281317.physics_Main.deriv.DAOD_HIGG4D6.r9264_p3083_p3416	
data15_13TeV.00284427.physics_Main.deriv.DAOD_HIGG4D6.r9264_p3083_p3416	
data15_13TeV.00279259.physics_Main.deriv.DAOD_HIGG4D6.r9264_p3083_p3416	
data15_13TeV.00284285.physics_Main.deriv.DAOD_HIGG4D6.r9264_p3083_p3416	
data15_13TeV.00279598.physics_Main.deriv.DAOD_HIGG4D6.r9264_p3083_p3416	
data15_13TeV.00276416.physics_Main.deriv.DAOD_HIGG4D6.r9264_p3083_p3416	
data15_13TeV.00280423.physics_Main.deriv.DAOD_HIGG4D6.r9264_p3083_p3416	

Table B.4.: Data samples from 2015 data taking.

Data 2015
data15_13TeV.00276954.physics_Main.deriv.DAOD_HIGG4D6.r9264_p3083_p3416
data15_13TeV.00282784.physics_Main.deriv.DAOD_HIGG4D6.r9264_p3083_p3416
data15_13TeV.00276511.physics_Main.deriv.DAOD_HIGG4D6.r9264_p3083_p3416
data15_13TeV.00279284.physics_Main.deriv.DAOD_HIGG4D6.r9264_p3083_p3416
data15_13TeV.00281130.physics_Main.deriv.DAOD_HIGG4D6.r9264_p3083_p3416
data15_13TeV.00282631.physics_Main.deriv.DAOD_HIGG4D6.r9264_p3083_p3416
data15_13TeV.00282992.physics_Main.deriv.DAOD_HIGG4D6.r9264_p3083_p3416
data15_13TeV.00284473.physics_Main.deriv.DAOD_HIGG4D6.r9264_p3083_p3416
data15_13TeV.00279345.physics_Main.deriv.DAOD_HIGG4D6.r9264_p3083_p3416
data15_13TeV.00284006.physics_Main.deriv.DAOD_HIGG4D6.r9264_p3083_p3416
data15_13TeV.00280977.physics_Main.deriv.DAOD_HIGG4D6.r9264_p3083_p3416
data15_13TeV.00281075.physics_Main.deriv.DAOD_HIGG4D6.r9264_p3083_p3416
data15_13TeV.00280673.physics_Main.deriv.DAOD_HIGG4D6.r9264_p3083_p3416
data15_13TeV.00276778.physics_Main.deriv.DAOD_HIGG4D6.r9264_p3083_p3416
data15_13TeV.00279867.physics_Main.deriv.DAOD_HIGG4D6.r9264_p3083_p3416

Table B.5.: Data samples from 2016 data taking.

Data 2016
data16_13TeV.00302137.physics_Main.deriv.DAOD_HIGG4D6.r9264_p3083_p3416
data16_13TeV.00298690.physics_Main.deriv.DAOD_HIGG4D6.r9264_p3083_p3416
data16_13TeV.00300784.physics_Main.deriv.DAOD_HIGG4D6.r9264_p3083_p3416
data16_13TeV.00304243.physics_Main.deriv.DAOD_HIGG4D6.r9264_p3083_p3416
data16_13TeV.00303338.physics_Main.deriv.DAOD_HIGG4D6.r9264_p3083_p3416
data16_13TeV.00298687.physics_Main.deriv.DAOD_HIGG4D6.r9264_p3083_p3416
data16_13TeV.00304308.physics_Main.deriv.DAOD_HIGG4D6.r9264_p3083_p3416
data16_13TeV.00301932.physics_Main.deriv.DAOD_HIGG4D6.r9264_p3083_p3416
data16_13TeV.00309440.physics_Main.deriv.DAOD_HIGG4D6.r9264_p3083_p3416
data16_13TeV.00300345.physics_Main.deriv.DAOD_HIGG4D6.r9264_p3083_p3416
data16_13TeV.00300655.physics_Main.deriv.DAOD_HIGG4D6.r9264_p3083_p3416
data16_13TeV.00302919.physics_Main.deriv.DAOD_HIGG4D6.r9264_p3083_p3416
data16_13TeV.00307716.physics_Main.deriv.DAOD_HIGG4D6.r9264_p3083_p3416
data16_13TeV.00307195.physics_Main.deriv.DAOD_HIGG4D6.r9264_p3083_p3416
data16_13TeV.00298771.physics_Main.deriv.DAOD_HIGG4D6.r9264_p3083_p3416
data16_13TeV.00306384.physics_Main.deriv.DAOD_HIGG4D6.r9264_p3083_p3416
data16_13TeV.00308084.physics_Main.deriv.DAOD_HIGG4D6.r9264_p3083_p3416

Table B.5.: Data samples from 2016 data taking.

Data 2016
data16_13TeV.00310468.physics_Main.deriv.DAOD_HIGG4D6.r9264_p3083_p3416
data16_13TeV.00300908.physics_Main.deriv.DAOD_HIGG4D6.r9264_p3083_p3416
data16_13TeV.00302053.physics_Main.deriv.DAOD_HIGG4D6.r9264_p3083_p3416
data16_13TeV.00303304.physics_Main.deriv.DAOD_HIGG4D6.r9264_p3083_p3416
data16_13TeV.00303499.physics_Main.deriv.DAOD_HIGG4D6.r9264_p3083_p3416
data16_13TeV.00304337.physics_Main.deriv.DAOD_HIGG4D6.r9264_p3083_p3416
data16_13TeV.00306451.physics_Main.deriv.DAOD_HIGG4D6.r9264_p3083_p3416
data16_13TeV.00307358.physics_Main.deriv.DAOD_HIGG4D6.r9264_p3083_p3416
data16_13TeV.00307732.physics_Main.deriv.DAOD_HIGG4D6.r9264_p3083_p3416
data16_13TeV.00309375.physics_Main.deriv.DAOD_HIGG4D6.r9264_p3083_p3416
data16_13TeV.00305543.physics_Main.deriv.DAOD_HIGG4D6.r9264_p3083_p3416
data16_13TeV.00306278.physics_Main.deriv.DAOD_HIGG4D6.r9264_p3083_p3416
data16_13TeV.00311170.physics_Main.deriv.DAOD_HIGG4D6.r9264_p3083_p3416
data16_13TeV.00308047.physics_Main.deriv.DAOD_HIGG4D6.r9264_p3083_p3416
data16_13TeV.00303208.physics_Main.deriv.DAOD_HIGG4D6.r9264_p3083_p3416
data16_13TeV.00307539.physics_Main.deriv.DAOD_HIGG4D6.r9264_p3083_p3416
data16_13TeV.00310015.physics_Main.deriv.DAOD_HIGG4D6.r9264_p3083_p3416
data16_13TeV.00300600.physics_Main.deriv.DAOD_HIGG4D6.r9264_p3083_p3416
data16_13TeV.00310691.physics_Main.deriv.DAOD_HIGG4D6.r9264_p3083_p3416
data16_13TeV.00306448.physics_Main.deriv.DAOD_HIGG4D6.r9264_p3083_p3416
data16_13TeV.00306269.physics_Main.deriv.DAOD_HIGG4D6.r9264_p3083_p3416
data16_13TeV.00303846.physics_Main.deriv.DAOD_HIGG4D6.r9264_p3083_p3416
data16_13TeV.00311321.physics_Main.deriv.DAOD_HIGG4D6.r9264_p3083_p3416
data16_13TeV.00303943.physics_Main.deriv.DAOD_HIGG4D6.r9264_p3083_p3416
data16_13TeV.00307259.physics_Main.deriv.DAOD_HIGG4D6.r9264_p3083_p3416
data16_13TeV.00305777.physics_Main.deriv.DAOD_HIGG4D6.r9264_p3083_p3416
data16_13TeV.00299584.physics_Main.deriv.DAOD_HIGG4D6.r9264_p3083_p3416
data16_13TeV.00300418.physics_Main.deriv.DAOD_HIGG4D6.r9264_p3083_p3416
data16_13TeV.00302380.physics_Main.deriv.DAOD_HIGG4D6.r9264_p3083_p3416
data16_13TeV.00304008.physics_Main.deriv.DAOD_HIGG4D6.r9264_p3083_p3416
data16_13TeV.00311244.physics_Main.deriv.DAOD_HIGG4D6.r9264_p3083_p3416
data16_13TeV.00302347.physics_Main.deriv.DAOD_HIGG4D6.r9264_p3083_p3416
data16_13TeV.00307306.physics_Main.deriv.DAOD_HIGG4D6.r9264_p3083_p3416
data16_13TeV.00309674.physics_Main.deriv.DAOD_HIGG4D6.r9264_p3083_p3416
data16_13TeV.00300687.physics_Main.deriv.DAOD_HIGG4D6.r9264_p3083_p3416
data16_13TeV.00306419.physics_Main.deriv.DAOD_HIGG4D6.r9264_p3083_p3416
data16_13TeV.00303201.physics_Main.deriv.DAOD_HIGG4D6.r9264_p3083_p3416
data16_13TeV.00303266.physics_Main.deriv.DAOD_HIGG4D6.r9264_p3083_p3416
data16_13TeV.00300540.physics_Main.deriv.DAOD_HIGG4D6.r9264_p3083_p3416
data16_13TeV.00307126.physics_Main.deriv.DAOD_HIGG4D6.r9264_p3083_p3416

Table B.5.: Data samples from 2016 data taking.

Data 2016
data16_13TeV.00309516.physics_Main.deriv.DAOD_HIGG4D6.r9264_p3083_p3416
data16_13TeV.00307354.physics_Main.deriv.DAOD_HIGG4D6.r9264_p3083_p3416
data16_13TeV.00303421.physics_Main.deriv.DAOD_HIGG4D6.r9264_p3083_p3416
data16_13TeV.00305727.physics_Main.deriv.DAOD_HIGG4D6.r9264_p3083_p3416
data16_13TeV.00300415.physics_Main.deriv.DAOD_HIGG4D6.r9264_p3083_p3416
data16_13TeV.00305811.physics_Main.deriv.DAOD_HIGG4D6.r9264_p3083_p3416
data16_13TeV.00310738.physics_Main.deriv.DAOD_HIGG4D6.r9264_p3083_p3416
data16_13TeV.00307656.physics_Main.deriv.DAOD_HIGG4D6.r9264_p3083_p3416
data16_13TeV.00310473.physics_Main.deriv.DAOD_HIGG4D6.r9264_p3083_p3416
data16_13TeV.00310863.physics_Main.deriv.DAOD_HIGG4D6.r9264_p3083_p3416
data16_13TeV.00298862.physics_Main.deriv.DAOD_HIGG4D6.r9264_p3083_p3416
data16_13TeV.00309759.physics_Main.deriv.DAOD_HIGG4D6.r9264_p3083_p3416
data16_13TeV.00298609.physics_Main.deriv.DAOD_HIGG4D6.r9264_p3083_p3416
data16_13TeV.00299243.physics_Main.deriv.DAOD_HIGG4D6.r9264_p3083_p3416
data16_13TeV.00304494.physics_Main.deriv.DAOD_HIGG4D6.r9264_p3083_p3416
data16_13TeV.00304178.physics_Main.deriv.DAOD_HIGG4D6.r9264_p3083_p3416
data16_13TeV.00310249.physics_Main.deriv.DAOD_HIGG4D6.r9264_p3083_p3416
data16_13TeV.00307710.physics_Main.deriv.DAOD_HIGG4D6.r9264_p3083_p3416
data16_13TeV.00311365.physics_Main.deriv.DAOD_HIGG4D6.r9264_p3083_p3416
data16_13TeV.00303892.physics_Main.deriv.DAOD_HIGG4D6.r9264_p3083_p3416
data16_13TeV.00310341.physics_Main.deriv.DAOD_HIGG4D6.r9264_p3083_p3416
data16_13TeV.00301918.physics_Main.deriv.DAOD_HIGG4D6.r9264_p3083_p3416
data16_13TeV.00302831.physics_Main.deriv.DAOD_HIGG4D6.r9264_p3083_p3416
data16_13TeV.00303560.physics_Main.deriv.DAOD_HIGG4D6.r9264_p3083_p3416
data16_13TeV.00303832.physics_Main.deriv.DAOD_HIGG4D6.r9264_p3083_p3416
data16_13TeV.00304198.physics_Main.deriv.DAOD_HIGG4D6.r9264_p3083_p3416
data16_13TeV.00303638.physics_Main.deriv.DAOD_HIGG4D6.r9264_p3083_p3416
data16_13TeV.00310969.physics_Main.deriv.DAOD_HIGG4D6.r9264_p3083_p3416
data16_13TeV.00307935.physics_Main.deriv.DAOD_HIGG4D6.r9264_p3083_p3416
data16_13TeV.00305618.physics_Main.deriv.DAOD_HIGG4D6.r9264_p3083_p3416
data16_13TeV.00309640.physics_Main.deriv.DAOD_HIGG4D6.r9264_p3083_p3416
data16_13TeV.00302925.physics_Main.deriv.DAOD_HIGG4D6.r9264_p3083_p3416
data16_13TeV.00310405.physics_Main.deriv.DAOD_HIGG4D6.r9264_p3083_p3416
data16_13TeV.00300571.physics_Main.deriv.DAOD_HIGG4D6.r9264_p3083_p3416
data16_13TeV.00301973.physics_Main.deriv.DAOD_HIGG4D6.r9264_p3083_p3416
data16_13TeV.00304409.physics_Main.deriv.DAOD_HIGG4D6.r9264_p3083_p3416
data16_13TeV.00305723.physics_Main.deriv.DAOD_HIGG4D6.r9264_p3083_p3416
data16_13TeV.00307514.physics_Main.deriv.DAOD_HIGG4D6.r9264_p3083_p3416
data16_13TeV.00305671.physics_Main.deriv.DAOD_HIGG4D6.r9264_p3083_p3416
data16_13TeV.00298633.physics_Main.deriv.DAOD_HIGG4D6.r9264_p3083_p3416

Table B.5.: Data samples from 2016 data taking.

Data 2016
data16_13TeV.00300487.physics_Main.deriv.DAOD_HIGG4D6.r9264_p3083_p3416
data16_13TeV.00307861.physics_Main.deriv.DAOD_HIGG4D6.r9264_p3083_p3416
data16_13TeV.00304128.physics_Main.deriv.DAOD_HIGG4D6.r9264_p3083_p3416
data16_13TeV.00306442.physics_Main.deriv.DAOD_HIGG4D6.r9264_p3083_p3416
data16_13TeV.00311473.physics_Main.deriv.DAOD_HIGG4D6.r9264_p3083_p3416
data16_13TeV.00302269.physics_Main.deriv.DAOD_HIGG4D6.r9264_p3083_p3416
data16_13TeV.00302956.physics_Main.deriv.DAOD_HIGG4D6.r9264_p3083_p3416
data16_13TeV.00297730.physics_Main.deriv.DAOD_HIGG4D6.r9264_p3083_p3416
data16_13TeV.00299184.physics_Main.deriv.DAOD_HIGG4D6.r9264_p3083_p3416
data16_13TeV.00299144.physics_Main.deriv.DAOD_HIGG4D6.r9264_p3083_p3416
data16_13TeV.00311287.physics_Main.deriv.DAOD_HIGG4D6.r9264_p3083_p3416
data16_13TeV.00304006.physics_Main.deriv.DAOD_HIGG4D6.r9264_p3083_p3416
data16_13TeV.00299288.physics_Main.deriv.DAOD_HIGG4D6.r9264_p3083_p3416
data16_13TeV.00305920.physics_Main.deriv.DAOD_HIGG4D6.r9264_p3083_p3416
data16_13TeV.00299055.physics_Main.deriv.DAOD_HIGG4D6.r9264_p3083_p3416
data16_13TeV.00306310.physics_Main.deriv.DAOD_HIGG4D6.r9264_p3083_p3416
data16_13TeV.00310872.physics_Main.deriv.DAOD_HIGG4D6.r9264_p3083_p3416
data16_13TeV.00304211.physics_Main.deriv.DAOD_HIGG4D6.r9264_p3083_p3416
data16_13TeV.00307569.physics_Main.deriv.DAOD_HIGG4D6.r9264_p3083_p3416
data16_13TeV.00311071.physics_Main.deriv.DAOD_HIGG4D6.r9264_p3083_p3416
data16_13TeV.00304431.physics_Main.deriv.DAOD_HIGG4D6.r9264_p3083_p3416
data16_13TeV.00310247.physics_Main.deriv.DAOD_HIGG4D6.r9264_p3083_p3416
data16_13TeV.00311481.physics_Main.deriv.DAOD_HIGG4D6.r9264_p3083_p3416
data16_13TeV.00302391.physics_Main.deriv.DAOD_HIGG4D6.r9264_p3083_p3416
data16_13TeV.00307394.physics_Main.deriv.DAOD_HIGG4D6.r9264_p3083_p3416
data16_13TeV.00302829.physics_Main.deriv.DAOD_HIGG4D6.r9264_p3083_p3416
data16_13TeV.00305380.physics_Main.deriv.DAOD_HIGG4D6.r9264_p3083_p3416
data16_13TeV.00300279.physics_Main.deriv.DAOD_HIGG4D6.r9264_p3083_p3416
data16_13TeV.00301915.physics_Main.deriv.DAOD_HIGG4D6.r9264_p3083_p3416
data16_13TeV.00299241.physics_Main.deriv.DAOD_HIGG4D6.r9264_p3083_p3416
data16_13TeV.00299343.physics_Main.deriv.DAOD_HIGG4D6.r9264_p3083_p3416
data16_13TeV.00305674.physics_Main.deriv.DAOD_HIGG4D6.r9264_p3083_p3416
data16_13TeV.00298595.physics_Main.deriv.DAOD_HIGG4D6.r9264_p3083_p3416
data16_13TeV.00303007.physics_Main.deriv.DAOD_HIGG4D6.r9264_p3083_p3416
data16_13TeV.00298773.physics_Main.deriv.DAOD_HIGG4D6.r9264_p3083_p3416
data16_13TeV.00302737.physics_Main.deriv.DAOD_HIGG4D6.r9264_p3083_p3416
data16_13TeV.00300800.physics_Main.deriv.DAOD_HIGG4D6.r9264_p3083_p3416
data16_13TeV.00302265.physics_Main.deriv.DAOD_HIGG4D6.r9264_p3083_p3416
data16_13TeV.00307454.physics_Main.deriv.DAOD_HIGG4D6.r9264_p3083_p3416
data16_13TeV.00302393.physics_Main.deriv.DAOD_HIGG4D6.r9264_p3083_p3416

Table B.5.: Data samples from 2016 data taking.

Data 2016
data16_13TeV.00309390.physics_Main.deriv.DAOD_HIGG4D6.r9264_p3083_p3416
data16_13TeV.00311402.physics_Main.deriv.DAOD_HIGG4D6.r9264_p3083_p3416
data16_13TeV.00302300.physics_Main.deriv.DAOD_HIGG4D6.r9264_p3083_p3416
data16_13TeV.00305735.physics_Main.deriv.DAOD_HIGG4D6.r9264_p3083_p3416
data16_13TeV.00303079.physics_Main.deriv.DAOD_HIGG4D6.r9264_p3083_p3416
data16_13TeV.00301912.physics_Main.deriv.DAOD_HIGG4D6.r9264_p3083_p3416
data16_13TeV.00299147.physics_Main.deriv.DAOD_HIGG4D6.r9264_p3083_p3416
data16_13TeV.00310809.physics_Main.deriv.DAOD_HIGG4D6.r9264_p3083_p3416
data16_13TeV.00303264.physics_Main.deriv.DAOD_HIGG4D6.r9264_p3083_p3416
data16_13TeV.00302872.physics_Main.deriv.DAOD_HIGG4D6.r9264_p3083_p3416
data16_13TeV.00298967.physics_Main.deriv.DAOD_HIGG4D6.r9264_p3083_p3416
data16_13TeV.00307619.physics_Main.deriv.DAOD_HIGG4D6.r9264_p3083_p3416
data16_13TeV.00305571.physics_Main.deriv.DAOD_HIGG4D6.r9264_p3083_p3416
data16_13TeV.00303059.physics_Main.deriv.DAOD_HIGG4D6.r9264_p3083_p3416
data16_13TeV.00310370.physics_Main.deriv.DAOD_HIGG4D6.r9264_p3083_p3416
data16_13TeV.00300863.physics_Main.deriv.DAOD_HIGG4D6.r9264_p3083_p3416
data16_13TeV.00303291.physics_Main.deriv.DAOD_HIGG4D6.r9264_p3083_p3416
data16_13TeV.00307601.physics_Main.deriv.DAOD_HIGG4D6.r9264_p3083_p3416
data16_13TeV.00310634.physics_Main.deriv.DAOD_HIGG4D6.r9264_p3083_p3416

Table B.6.: Data samples from 2017 data taking.

Data 2017
data17_13TeV.00337491.physics_Main.deriv.DAOD_HIGG4D6.f873_m1885_p3355
data17_13TeV.00331085.physics_Main.deriv.DAOD_HIGG4D6.f859_m1860_p3355
data17_13TeV.00327761.physics_Main.deriv.DAOD_HIGG4D6.f838_m1824_p3416
data17_13TeV.00331019.physics_Main.deriv.DAOD_HIGG4D6.f846_m1839_p3416
data17_13TeV.00326439.physics_Main.deriv.DAOD_HIGG4D6.f838_m1824_p3416
data17_13TeV.00327745.physics_Main.deriv.DAOD_HIGG4D6.f838_m1824_p3416
data17_13TeV.00330074.physics_Main.deriv.DAOD_HIGG4D6.f843_m1824_p3416
data17_13TeV.00325713.physics_Main.deriv.DAOD_HIGG4D6.f839_m1824_p3416
data17_13TeV.00326468.physics_Main.deriv.DAOD_HIGG4D6.f838_m1824_p3416
data17_13TeV.00326834.physics_Main.deriv.DAOD_HIGG4D6.f837_m1824_p3416
data17_13TeV.00327057.physics_Main.deriv.DAOD_HIGG4D6.f837_m1824_p3416
data17_13TeV.00328017.physics_Main.deriv.DAOD_HIGG4D6.f836_m1824_p3416
data17_13TeV.00328374.physics_Main.deriv.DAOD_HIGG4D6.f836_m1824_p3416

Table B.6.: Data samples from 2017 data taking.

Data 2017
data17_13TeV.00330160.physics_Main.deriv.DAOD_HIGG4D6.f843_m1824_p3416
data17_13TeV.00325789.physics_Main.deriv.DAOD_HIGG4D6.f839_m1824_p3416
data17_13TeV.00331905.physics_Main.deriv.DAOD_HIGG4D6.f848_m1844_p3416
data17_13TeV.00334878.physics_Main.deriv.DAOD_HIGG4D6.f867_m1860_p3416
data17_13TeV.00335016.physics_Main.deriv.DAOD_HIGG4D6.f868_m1870_p3416
data17_13TeV.00332896.physics_Main.deriv.DAOD_HIGG4D6.f854_m1850_p3416
data17_13TeV.00336678.physics_Main.deriv.DAOD_HIGG4D6.f868_m1870_p3416
data17_13TeV.00327582.physics_Main.deriv.DAOD_HIGG4D6.f838_m1824_p3416
data17_13TeV.00327636.physics_Main.deriv.DAOD_HIGG4D6.f838_m1824_p3416
data17_13TeV.00333487.physics_Main.deriv.DAOD_HIGG4D6.f857_m1855_p3416
data17_13TeV.00329716.physics_Main.deriv.DAOD_HIGG4D6.f847_m1839_p3416
data17_13TeV.00329778.physics_Main.deriv.DAOD_HIGG4D6.f843_m1824_p3416
data17_13TeV.00336630.physics_Main.deriv.DAOD_HIGG4D6.f868_m1870_p3416
data17_13TeV.00331462.physics_Main.deriv.DAOD_HIGG4D6.f848_m1844_p3416
data17_13TeV.00333853.physics_Main.deriv.DAOD_HIGG4D6.f857_m1855_p3416
data17_13TeV.00328393.physics_Main.deriv.DAOD_HIGG4D6.f836_m1824_p3416
data17_13TeV.00329835.physics_Main.deriv.DAOD_HIGG4D6.f843_m1824_p3416
data17_13TeV.00329869.physics_Main.deriv.DAOD_HIGG4D6.f843_m1824_p3416
data17_13TeV.00331479.physics_Main.deriv.DAOD_HIGG4D6.f848_m1844_p3416
data17_13TeV.00331825.physics_Main.deriv.DAOD_HIGG4D6.f848_m1844_p3416
data17_13TeV.00332304.physics_Main.deriv.DAOD_HIGG4D6.f851_m1850_p3416
data17_13TeV.00334580.physics_Main.deriv.DAOD_HIGG4D6.f859_m1860_p3416
data17_13TeV.00338834.physics_Main.deriv.DAOD_HIGG4D6.f877_m1892_p3416
data17_13TeV.00331697.physics_Main.deriv.DAOD_HIGG4D6.f848_m1844_p3416
data17_13TeV.00333192.physics_Main.deriv.DAOD_HIGG4D6.f857_m1855_p3416
data17_13TeV.00333367.physics_Main.deriv.DAOD_HIGG4D6.f857_m1855_p3416
data17_13TeV.00337335.physics_Main.deriv.DAOD_HIGG4D6.f871_m1879_p3416
data17_13TeV.00339037.physics_Main.deriv.DAOD_HIGG4D6.f887_m1897_p3416
data17_13TeV.00339346.physics_Main.deriv.DAOD_HIGG4D6.f887_m1897_p3416
data17_13TeV.00333994.physics_Main.deriv.DAOD_HIGG4D6.f859_m1860_p3416
data17_13TeV.00332720.physics_Main.deriv.DAOD_HIGG4D6.f851_m1850_p3416
data17_13TeV.00329385.physics_Main.deriv.DAOD_HIGG4D6.f841_m1824_p3416
data17_13TeV.00330470.physics_Main.deriv.DAOD_HIGG4D6.f843_m1824_p3416
data17_13TeV.00331951.physics_Main.deriv.DAOD_HIGG4D6.f848_m1844_p3416
data17_13TeV.00326446.physics_Main.deriv.DAOD_HIGG4D6.f838_m1824_p3416
data17_13TeV.00326695.physics_Main.deriv.DAOD_HIGG4D6.f838_m1824_p3416
data17_13TeV.00331082.physics_Main.deriv.DAOD_HIGG4D6.f846_m1839_p3416
data17_13TeV.00330166.physics_Main.deriv.DAOD_HIGG4D6.f843_m1824_p3416
data17_13TeV.00330101.physics_Main.deriv.DAOD_HIGG4D6.f843_m1824_p3416
data17_13TeV.00326923.physics_Main.deriv.DAOD_HIGG4D6.f837_m1824_p3416

Table B.6.: Data samples from 2017 data taking.

Data 2017	
data17_13TeV.00326945.physics_Main.deriv.DAOD_HIGG4D6.f837_m1824_p3416	
data17_13TeV.00328221.physics_Main.deriv.DAOD_HIGG4D6.f836_m1824_p3416	
data17_13TeV.00329484.physics_Main.deriv.DAOD_HIGG4D6.f841_m1824_p3416	
data17_13TeV.00329542.physics_Main.deriv.DAOD_HIGG4D6.f841_m1824_p3416	
data17_13TeV.00330079.physics_Main.deriv.DAOD_HIGG4D6.f843_m1824_p3416	
data17_13TeV.00334890.physics_Main.deriv.DAOD_HIGG4D6.f867_m1860_p3416	
data17_13TeV.00335056.physics_Main.deriv.DAOD_HIGG4D6.f868_m1870_p3416	
data17_13TeV.00333707.physics_Main.deriv.DAOD_HIGG4D6.f857_m1855_p3416	
data17_13TeV.00326870.physics_Main.deriv.DAOD_HIGG4D6.f837_m1824_p3416	
data17_13TeV.00331875.physics_Main.deriv.DAOD_HIGG4D6.f848_m1844_p3416	
data17_13TeV.00338967.physics_Main.deriv.DAOD_HIGG4D6.f877_m1897_p3416	
data17_13TeV.00332955.physics_Main.deriv.DAOD_HIGG4D6.f854_m1850_p3416	
data17_13TeV.00334455.physics_Main.deriv.DAOD_HIGG4D6.f859_m1860_p3416	
data17_13TeV.00334710.physics_Main.deriv.DAOD_HIGG4D6.f859_m1860_p3416	
data17_13TeV.00330874.physics_Main.deriv.DAOD_HIGG4D6.f846_m1839_p3416	
data17_13TeV.00328042.physics_Main.deriv.DAOD_HIGG4D6.f836_m1824_p3416	
data17_13TeV.00329780.physics_Main.deriv.DAOD_HIGG4D6.f843_m1824_p3416	
data17_13TeV.00330203.physics_Main.deriv.DAOD_HIGG4D6.f843_m1824_p3416	
data17_13TeV.00335082.physics_Main.deriv.DAOD_HIGG4D6.f868_m1870_p3416	
data17_13TeV.00331020.physics_Main.deriv.DAOD_HIGG4D6.f846_m1839_p3416	
data17_13TeV.00332915.physics_Main.deriv.DAOD_HIGG4D6.f854_m1850_p3416	
data17_13TeV.00328099.physics_Main.deriv.DAOD_HIGG4D6.f836_m1824_p3416	
data17_13TeV.00336567.physics_Main.deriv.DAOD_HIGG4D6.f873_m1885_p3416	
data17_13TeV.00337542.physics_Main.deriv.DAOD_HIGG4D6.f873_m1885_p3416	
data17_13TeV.00338220.physics_Main.deriv.DAOD_HIGG4D6.f877_m1885_p3416	
data17_13TeV.00336506.physics_Main.deriv.DAOD_HIGG4D6.f873_m1885_p3416	
data17_13TeV.00330025.physics_Main.deriv.DAOD_HIGG4D6.f843_m1824_p3416	
data17_13TeV.00327342.physics_Main.deriv.DAOD_HIGG4D6.f838_m1824_p3416	
data17_13TeV.00333979.physics_Main.deriv.DAOD_HIGG4D6.f859_m1860_p3416	
data17_13TeV.00335170.physics_Main.deriv.DAOD_HIGG4D6.f868_m1870_p3416	
data17_13TeV.00339396.physics_Main.deriv.DAOD_HIGG4D6.f887_m1897_p3416	
data17_13TeV.00340368.physics_Main.deriv.DAOD_HIGG4D6.f894_m1907_p3416	
data17_13TeV.00334350.physics_Main.deriv.DAOD_HIGG4D6.f859_m1860_p3416	
data17_13TeV.00338259.physics_Main.deriv.DAOD_HIGG4D6.f877_m1885_p3416	
data17_13TeV.00338767.physics_Main.deriv.DAOD_HIGG4D6.f877_m1892_p3416	
data17_13TeV.00340072.physics_Main.deriv.DAOD_HIGG4D6.f889_m1907_p3416	
data17_13TeV.00333519.physics_Main.deriv.DAOD_HIGG4D6.f857_m1855_p3416	
data17_13TeV.00330875.physics_Main.deriv.DAOD_HIGG4D6.f846_m1839_p3416	
data17_13TeV.00333828.physics_Main.deriv.DAOD_HIGG4D6.f857_m1855_p3416	
data17_13TeV.00334907.physics_Main.deriv.DAOD_HIGG4D6.f867_m1860_p3416	

Table B.6.: Data samples from 2017 data taking.

Data 2017
data17_13TeV.00336944.physics_Main.deriv.DAOD_HIGG4D6.f871_m1879_p3416
data17_13TeV.00338675.physics_Main.deriv.DAOD_HIGG4D6.f877_m1892_p3416
data17_13TeV.00338897.physics_Main.deriv.DAOD_HIGG4D6.f877_m1897_p3416
data17_13TeV.00334849.physics_Main.deriv.DAOD_HIGG4D6.f867_m1860_p3416
data17_13TeV.00337005.physics_Main.deriv.DAOD_HIGG4D6.f871_m1879_p3416
data17_13TeV.00339758.physics_Main.deriv.DAOD_HIGG4D6.f889_m1902_p3416
data17_13TeV.00327662.physics_Main.deriv.DAOD_HIGG4D6.f838_m1824_p3416
data17_13TeV.00333181.physics_Main.deriv.DAOD_HIGG4D6.f854_m1850_p3416
data17_13TeV.00333426.physics_Main.deriv.DAOD_HIGG4D6.f857_m1855_p3416
data17_13TeV.00330328.physics_Main.deriv.DAOD_HIGG4D6.f843_m1824_p3416
data17_13TeV.00337371.physics_Main.deriv.DAOD_HIGG4D6.f871_m1879_p3416
data17_13TeV.00331239.physics_Main.deriv.DAOD_HIGG4D6.f848_m1844_p3416
data17_13TeV.00331085.physics_Main.deriv.DAOD_HIGG4D6.f848_m1844_p3416
data17_13TeV.00337176.physics_Main.deriv.DAOD_HIGG4D6.f871_m1879_p3416
data17_13TeV.00336915.physics_Main.deriv.DAOD_HIGG4D6.f871_m1879_p3416
data17_13TeV.00331860.physics_Main.deriv.DAOD_HIGG4D6.f848_m1844_p3416
data17_13TeV.00337156.physics_Main.deriv.DAOD_HIGG4D6.f871_m1879_p3416
data17_13TeV.00339957.physics_Main.deriv.DAOD_HIGG4D6.f889_m1902_p3416
data17_13TeV.00336852.physics_Main.deriv.DAOD_HIGG4D6.r10258_p3399_p3510
data17_13TeV.00338846.physics_Main.deriv.DAOD_HIGG4D6.f877_m1892_p3416
data17_13TeV.00335131.physics_Main.deriv.DAOD_HIGG4D6.f868_m1870_p3416
data17_13TeV.00339562.physics_Main.deriv.DAOD_HIGG4D6.f889_m1902_p3416
data17_13TeV.00329964.physics_Main.deriv.DAOD_HIGG4D6.f843_m1824_p3416
data17_13TeV.00337451.physics_Main.deriv.DAOD_HIGG4D6.f873_m1879_p3416
data17_13TeV.00331772.physics_Main.deriv.DAOD_HIGG4D6.f848_m1844_p3416
data17_13TeV.00334264.physics_Main.deriv.DAOD_HIGG4D6.f859_m1860_p3416
data17_13TeV.00334779.physics_Main.deriv.DAOD_HIGG4D6.f867_m1860_p3416
data17_13TeV.00334637.physics_Main.deriv.DAOD_HIGG4D6.f859_m1860_p3416
data17_13TeV.00335083.physics_Main.deriv.DAOD_HIGG4D6.f868_m1870_p3416
data17_13TeV.00337662.physics_Main.deriv.DAOD_HIGG4D6.f877_m1885_p3416
data17_13TeV.00339500.physics_Main.deriv.DAOD_HIGG4D6.f889_m1902_p3416
data17_13TeV.00340453.physics_Main.deriv.DAOD_HIGG4D6.f894_m1902_p3416
data17_13TeV.00335222.physics_Main.deriv.DAOD_HIGG4D6.f868_m1870_p3416
data17_13TeV.00334564.physics_Main.deriv.DAOD_HIGG4D6.f859_m1860_p3416
data17_13TeV.00337491.physics_Main.deriv.DAOD_HIGG4D6.f873_m1885_p3416
data17_13TeV.00328333.physics_Main.deriv.DAOD_HIGG4D6.f836_m1824_p3416
data17_13TeV.00330294.physics_Main.deriv.DAOD_HIGG4D6.f843_m1824_p3416
data17_13TeV.00327103.physics_Main.deriv.DAOD_HIGG4D6.f838_m1824_p3416
data17_13TeV.00337263.physics_Main.deriv.DAOD_HIGG4D6.f871_m1879_p3416
data17_13TeV.00340030.physics_Main.deriv.DAOD_HIGG4D6.f889_m1902_p3416

Table B.6.: Data samples from 2017 data taking.

Data 2017	
data17_13TeV.00326657.physics_Main.deriv.DAOD_HIGG4D6.f838_m1824_p3416	
data17_13TeV.00334993.physics_Main.deriv.DAOD_HIGG4D6.f868_m1870_p3416	
data17_13TeV.00335282.physics_Main.deriv.DAOD_HIGG4D6.f868_m1870_p3416	
data17_13TeV.00331215.physics_Main.deriv.DAOD_HIGG4D6.f848_m1844_p3416	
data17_13TeV.00331975.physics_Main.deriv.DAOD_HIGG4D6.f851_m1850_p3416	
data17_13TeV.00338608.physics_Main.deriv.DAOD_HIGG4D6.f877_m1892_p3416	
data17_13TeV.00339070.physics_Main.deriv.DAOD_HIGG4D6.f887_m1897_p3416	
data17_13TeV.00339387.physics_Main.deriv.DAOD_HIGG4D6.f887_m1897_p3416	
data17_13TeV.00333904.physics_Main.deriv.DAOD_HIGG4D6.f857_m1855_p3416	
data17_13TeV.00334960.physics_Main.deriv.DAOD_HIGG4D6.f868_m1870_p3416	
data17_13TeV.00331033.physics_Main.deriv.DAOD_HIGG4D6.f846_m1839_p3416	
data17_13TeV.00334678.physics_Main.deriv.DAOD_HIGG4D6.f859_m1860_p3416	
data17_13TeV.00336832.physics_Main.deriv.DAOD_HIGG4D6.f868_m1879_p3416	
data17_13TeV.00334384.physics_Main.deriv.DAOD_HIGG4D6.f859_m1860_p3416	
data17_13TeV.00338377.physics_Main.deriv.DAOD_HIGG4D6.f877_m1885_p3416	
data17_13TeV.00335290.physics_Main.deriv.DAOD_HIGG4D6.f868_m1870_p3416	
data17_13TeV.00327265.physics_Main.deriv.DAOD_HIGG4D6.f838_m1824_p3416	
data17_13TeV.00337705.physics_Main.deriv.DAOD_HIGG4D6.f877_m1885_p3416	
data17_13TeV.00339535.physics_Main.deriv.DAOD_HIGG4D6.f889_m1902_p3416	
data17_13TeV.00334317.physics_Main.deriv.DAOD_HIGG4D6.f859_m1860_p3416	
data17_13TeV.00336719.physics_Main.deriv.DAOD_HIGG4D6.f868_m1870_p3416	
data17_13TeV.00337833.physics_Main.deriv.DAOD_HIGG4D6.f886_m1885_p3416	
data17_13TeV.00332303.physics_Main.deriv.DAOD_HIGG4D6.f851_m1850_p3416	
data17_13TeV.00336782.physics_Main.deriv.DAOD_HIGG4D6.f868_m1879_p3416	
data17_13TeV.00334737.physics_Main.deriv.DAOD_HIGG4D6.f859_m1860_p3416	
data17_13TeV.00337052.physics_Main.deriv.DAOD_HIGG4D6.f871_m1879_p3416	
data17_13TeV.00337404.physics_Main.deriv.DAOD_HIGG4D6.f871_m1879_p3416	
data17_13TeV.00339205.physics_Main.deriv.DAOD_HIGG4D6.f887_m1897_p3416	
data17_13TeV.00328263.physics_Main.deriv.DAOD_HIGG4D6.f836_m1824_p3416	
data17_13TeV.00327490.physics_Main.deriv.DAOD_HIGG4D6.f838_m1824_p3416	
data17_13TeV.00327764.physics_Main.deriv.DAOD_HIGG4D6.f836_m1824_p3416	
data17_13TeV.00334842.physics_Main.deriv.DAOD_HIGG4D6.f867_m1860_p3416	
data17_13TeV.00331742.physics_Main.deriv.DAOD_HIGG4D6.f848_m1844_p3416	
data17_13TeV.00333778.physics_Main.deriv.DAOD_HIGG4D6.f857_m1855_p3416	
data17_13TeV.00338933.physics_Main.deriv.DAOD_HIGG4D6.f877_m1897_p3416	
data17_13TeV.00338349.physics_Main.deriv.DAOD_HIGG4D6.f877_m1885_p3416	
data17_13TeV.00326551.physics_Main.deriv.DAOD_HIGG4D6.f838_m1824_p3416	
data17_13TeV.00331804.physics_Main.deriv.DAOD_HIGG4D6.f848_m1844_p3416	
data17_13TeV.00335022.physics_Main.deriv.DAOD_HIGG4D6.f868_m1870_p3416	
data17_13TeV.00333380.physics_Main.deriv.DAOD_HIGG4D6.f857_m1855_p3416	

Table B.6.: Data samples from 2017 data taking.

Data 2017
data17_13TeV.00334413.physics_Main.deriv.DAOD_HIGG4D6.f859_m1860_p3416
data17_13TeV.00337215.physics_Main.deriv.DAOD_HIGG4D6.f871_m1879_p3416
data17_13TeV.00338987.physics_Main.deriv.DAOD_HIGG4D6.f887_m1897_p3416
data17_13TeV.00333650.physics_Main.deriv.DAOD_HIGG4D6.f857_m1855_p3416
data17_13TeV.00331129.physics_Main.deriv.DAOD_HIGG4D6.f848_m1844_p3416
data17_13TeV.00338183.physics_Main.deriv.DAOD_HIGG4D6.f877_m1885_p3416
data17_13TeV.00337107.physics_Main.deriv.DAOD_HIGG4D6.f871_m1879_p3416
data17_13TeV.00339849.physics_Main.deriv.DAOD_HIGG4D6.f889_m1902_p3416
data17_13TeV.00331710.physics_Main.deriv.DAOD_HIGG4D6.f848_m1844_p3416
data17_13TeV.00335177.physics_Main.deriv.DAOD_HIGG4D6.f868_m1870_p3416
data17_13TeV.00329829.physics_Main.deriv.DAOD_HIGG4D6.f843_m1824_p3416
data17_13TeV.00334588.physics_Main.deriv.DAOD_HIGG4D6.f859_m1860_p3416
data17_13TeV.00338498.physics_Main.deriv.DAOD_HIGG4D6.f877_m1892_p3416
data17_13TeV.00337662.physics_Main.deriv.DAOD_HIGG4D6.r10258_p3399_p3510
data17_13TeV.00334443.physics_Main.deriv.DAOD_HIGG4D6.f859_m1860_p3416
data17_13TeV.00339435.physics_Main.deriv.DAOD_HIGG4D6.f887_m1897_p3416
data17_13TeV.00325790.physics_Main.deriv.DAOD_HIGG4D6.f839_m1824_p3416
data17_13TeV.00338712.physics_Main.deriv.DAOD_HIGG4D6.f877_m1892_p3416
data17_13TeV.00338263.physics_Main.deriv.DAOD_HIGG4D6.f877_m1885_p3416
data17_13TeV.00327860.physics_Main.deriv.DAOD_HIGG4D6.f836_m1824_p3416
data17_13TeV.00334487.physics_Main.deriv.DAOD_HIGG4D6.f859_m1860_p3416
data17_13TeV.00330857.physics_Main.deriv.DAOD_HIGG4D6.f846_m1839_p3416
data17_13TeV.00332953.physics_Main.deriv.DAOD_HIGG4D6.f854_m1850_p3416
data17_13TeV.00336998.physics_Main.deriv.DAOD_HIGG4D6.f871_m1879_p3416
data17_13TeV.00327862.physics_Main.deriv.DAOD_HIGG4D6.f836_m1824_p3416
data17_13TeV.00336852.physics_Main.deriv.DAOD_HIGG4D6.f871_m1879_p3416
data17_13TeV.00331466.physics_Main.deriv.DAOD_HIGG4D6.f848_m1844_p3416
data17_13TeV.00333469.physics_Main.deriv.DAOD_HIGG4D6.f857_m1855_p3416
data17_13TeV.00336927.physics_Main.deriv.DAOD_HIGG4D6.f871_m1879_p3416
data17_13TeV.00338480.physics_Main.deriv.DAOD_HIGG4D6.f877_m1892_p3416
data17_13TeV.00339590.physics_Main.deriv.DAOD_HIGG4D6.f889_m1902_p3416
data17_13TeV.00336548.physics_Main.deriv.DAOD_HIGG4D6.f873_m1885_p3416

Table B.3.: Trigger list for the $Z \rightarrow \tau\tau(+\text{jets})$ analysis.

Trigger name
HLT_j360_a10r_L1J100
HLT_j360_a10_lcw_L1J100
HLT_j400_a10r_L1J100
HLT_j400_a10_lcw_L1J100
HLT_j420_a10_lcw_L1J100
HLT_j420_a10r_L1J100
HLT_j390_a10t_lcw_jes_30smcINF_L1J100
HLT_j420_a10r_L1J100
HLT_j420_a10t_lcw_jes_L1J100
HLT_j420_a10_lcw_subjes_L1J100
HLT_j420_a10t_lcw_jes_40smcINF_L1J100
HLT_j440_a10r_L1J100
HLT_j440_a10t_lcw_jes_L1J100
HLT_j440_a10_lcw_subjes_L1J100
HLT_j440_a10t_lcw_jes_40smcINF_L1J100
HLT_j460_a10r_L1J100
HLT_j460_a10t_lcw_jes_L1J100
HLT_j460_a10_lcw_subjes_L1J100
HLT_j480_a10r_L1J100
HLT_j480_a10t_lcw_jes_L1J100
HLT_j480_a10_lcw_subjes_L1J100

Table B.7.: MC16a samples (for 2015 and 2016 data-taking).

$Z \rightarrow \tau\tau(+\text{jets})$ inclusive	
mc16_13TeV.361108.PowhegPythia8EvtGen_AZNLOCTEQ6L1_Ztautau.deriv.DAOD_HIGG4D6.e3601_s3126_r9364_r9315_p3415	
$Z \rightarrow \tau\tau(+\text{jets})$	
mc16_13TeV.364137.Sherpa_221_NNPDF30NNLO_Ztautau_MAXHTPTV280_500_CVetoBVeto.deriv.DAOD_HIGG4D6.e5307_s3126_r9364_r9315_p3415	
mc16_13TeV.364134.Sherpa_221_NNPDF30NNLO_Ztautau_MAXHTPTV140_280_CVetoBVeto.deriv.DAOD_HIGG4D6.e5307_s3126_r9364_r9315_p3415	
mc16_13TeV.364140.Sherpa_221_NNPDF30NNLO_Ztautau_MAXHTPTV500_1000.deriv.DAOD_HIGG4D6.e5307_s3126_r9364_r9315_p3415	
mc16_13TeV.364141.Sherpa_221_NNPDF30NNLO_Ztautau_MAXHTPTV1000_E_CMS.deriv.DAOD_HIGG4D6.e5307_s3126_r9364_r9315_p3415	
mc16_13TeV.364131.Sherpa_221_NNPDF30NNLO_Ztautau_MAXHTPTV70_140_CVetoBVeto.deriv.DAOD_HIGG4D6.e5307_s3126_r9364_r9315_p3415	
mc16_13TeV.364136.Sherpa_221_NNPDF30NNLO_Ztautau_MAXHTPTV140_280_BFilter.deriv.DAOD_HIGG4D6.e5307_s3126_r9364_r9315_p3415	
mc16_13TeV.364129.Sherpa_221_NNPDF30NNLO_Ztautau_MAXHTPTV0_70_CFilterBVeto.deriv.DAOD_HIGG4D6.e5307_s3126_r9364_r9315_p3415	
mc16_13TeV.364130.Sherpa_221_NNPDF30NNLO_Ztautau_MAXHTPTV0_70_BFilter.deriv.DAOD_HIGG4D6.e5307_s3126_r9364_r9315_p3415	
mc16_13TeV.364135.Sherpa_221_NNPDF30NNLO_Ztautau_MAXHTPTV140_280_CFilterBVeto.deriv.DAOD_HIGG4D6.e5307_s3126_r9364_r9315_p3415	
mc16_13TeV.364128.Sherpa_221_NNPDF30NNLO_Ztautau_MAXHTPTV0_70_CVetoBVeto.deriv.DAOD_HIGG4D6.e5307_s3126_r9364_r9315_p3415	
mc16_13TeV.364132.Sherpa_221_NNPDF30NNLO_Ztautau_MAXHTPTV70_140_CFilterBVeto.deriv.DAOD_HIGG4D6.e5307_s3126_r9364_r9315_p3415	
mc16_13TeV.364133.Sherpa_221_NNPDF30NNLO_Ztautau_MAXHTPTV70_140_BFilter.deriv.DAOD_HIGG4D6.e5307_s3126_r9364_r9315_p3415	
mc16_13TeV.364138.Sherpa_221_NNPDF30NNLO_Ztautau_MAXHTPTV280_500_CFilterBVeto.deriv.DAOD_HIGG4D6.e5313_s3126_r9364_p3415	
mc16_13TeV.364139.Sherpa_221_NNPDF30NNLO_Ztautau_MAXHTPTV280_500_BFilter.deriv.DAOD_HIGG4D6.e5313_s3126_r9364_p3415	
$W \rightarrow \tau\nu$	
mc16_13TeV.364193.Sherpa_221_NNPDF30NNLO_Wtaunu_MAXHTPTV280_500_CVetoBVeto.deriv.DAOD_HIGG4D6.e5340_s3126_r9364_r9315_p3415	
mc16_13TeV.364186.Sherpa_221_NNPDF30NNLO_Wtaunu_MAXHTPTV0_70_BFilter.deriv.DAOD_HIGG4D6.e5340_s3126_r9364_r9315_p3415	
mc16_13TeV.364197.Sherpa_221_NNPDF30NNLO_Wtaunu_MAXHTPTV1000_E_CMS.deriv.DAOD_HIGG4D6.e5340_s3126_r9364_r9315_p3415	
mc16_13TeV.364184.Sherpa_221_NNPDF30NNLO_Wtaunu_MAXHTPTV0_70_CVetoBVeto.deriv.DAOD_HIGG4D6.e5340_s3126_r9364_r9315_p3415	
mc16_13TeV.364191.Sherpa_221_NNPDF30NNLO_Wtaunu_MAXHTPTV140_280_CFilterBVeto.deriv.DAOD_HIGG4D6.e5340_s3126_r9364_r9315_p3415	
mc16_13TeV.364192.Sherpa_221_NNPDF30NNLO_Wtaunu_MAXHTPTV140_280_BFilter.deriv.DAOD_HIGG4D6.e5340_s3126_r9364_r9315_p3415	
mc16_13TeV.364189.Sherpa_221_NNPDF30NNLO_Wtaunu_MAXHTPTV70_140_BFilter.deriv.DAOD_HIGG4D6.e5340_s3126_r9364_r9315_p3415	
mc16_13TeV.364187.Sherpa_221_NNPDF30NNLO_Wtaunu_MAXHTPTV70_140_CVetoBVeto.deriv.DAOD_HIGG4D6.e5340_s3126_r9364_r9315_p3415	
mc16_13TeV.364188.Sherpa_221_NNPDF30NNLO_Wtaunu_MAXHTPTV70_140_CFilterBVeto.deriv.DAOD_HIGG4D6.e5340_s3126_r9364_r9315_p3415	
mc16_13TeV.364190.Sherpa_221_NNPDF30NNLO_Wtaunu_MAXHTPTV140_280_CVetoBVeto.deriv.DAOD_HIGG4D6.e5340_s3126_r9364_r9315_p3415	
mc16_13TeV.364185.Sherpa_221_NNPDF30NNLO_Wtaunu_MAXHTPTV140_280_CFilterBVeto.deriv.DAOD_HIGG4D6.e5340_s3126_r9364_r9315_p3415	
mc16_13TeV.364194.Sherpa_221_NNPDF30NNLO_Wtaunu_MAXHTPTV280_500_CFilterBVeto.deriv.DAOD_HIGG4D6.e5340_s3126_r9364_r9315_p3415	
mc16_13TeV.364195.Sherpa_221_NNPDF30NNLO_Wtaunu_MAXHTPTV280_500_BFilter.deriv.DAOD_HIGG4D6.e5340_s3126_r9364_r9315_p3415	
mc16_13TeV.364196.Sherpa_221_NNPDF30NNLO_Wtaunu_MAXHTPTV500_1000.deriv.DAOD_HIGG4D6.e5340_s3126_r9364_r9315_p3415	
$t\bar{t}$	

Table B.7.: MC16a samples (for 2015 and 2016 data-taking).

mc16_13TeV.410470.PhPy8EG_A14_ttbar_hdamp258p75_nonallhad.deriv.DAOD_HIGG4D6.e6337_e5984_s3126_r9364_r9315_p3415
mc16_13TeV.410471.PhPy8EG_A14_ttbar_hdamp258p75_allhad.deriv.DAOD_HIGG4D6.e6337_e5984_s3126_r9364_r9315_p3415
di-boson
mc16_13TeV.361600.PowhegPy8EG_CT10nloME_AZNLOCTEQ6L1_WWlvlv.deriv.DAOD_HIGG4D6.e4616_s3126_r9364_p3415
mc16_13TeV.361601.PowhegPy8EG_CT10nloME_AZNLOCTEQ6L1_WZlvll_mll4.deriv.DAOD_HIGG4D6.e4475_s3126_r9364_p3415
mc16_13TeV.361602.PowhegPy8EG_CT10nloME_AZNLOCTEQ6L1_WZlvvv_mll4.deriv.DAOD_HIGG4D6.e4054_s3126_r9364_p3415
mc16_13TeV.361603.PowhegPy8EG_CT10nloME_AZNLOCTEQ6L1_ZZllll_mll4.deriv.DAOD_HIGG4D6.e4475_s3126_r9364_p3415
mc16_13TeV.361607.PowhegPy8EG_CT10nloME_AZNLOCTEQ6L1_WZqqll_mll20.deriv.DAOD_HIGG4D6.e4711_s3126_r9364_p3415
mc16_13TeV.361610.PowhegPy8EG_CT10nloME_AZNLOCTEQ6L1_ZZqqll_mqg20mll20.deriv.DAOD_HIGG4D6.e4711_s3126_r9364_p3415
mc16_13TeV.361605.PowhegPy8EG_CT10nloME_AZNLOCTEQ6L1_ZZvvvv_mll4.deriv.DAOD_HIGG4D6.e4054_s3126_r9364_p3415
mc16_13TeV.361604.PowhegPy8EG_CT10nloME_AZNLOCTEQ6L1_ZZvvll_mll4.deriv.DAOD_HIGG4D6.e4475_s3126_r9364_p3415

Table B.8.: MC16d samples (for 2017 data-taking).

$Z \rightarrow \tau\tau(+\text{jets})$ inclusive
mc16_13TeV.361108.PowhegPythia8EvtGen_AZNLOCTEQ6L1_Ztautau.deriv.DAOD_HIGG4D6.e3601_s3126_r10201_r10210_p3529
$Z \rightarrow \tau\tau(+\text{jets})$
mc16_13TeV.364128.Sherpa_221_NNPDF30NNLO_Ztautau_MAXHTPTV0_70_CVetoBVeto.deriv.DAOD_HIGG4D6.e5307_e5984_s3126_r10201_r10210_p3529
mc16_13TeV.364129.Sherpa_221_NNPDF30NNLO_Ztautau_MAXHTPTV0_70_CFilterBVeto.deriv.DAOD_HIGG4D6.e5307_e5984_s3126_r10201_r10210_p3529
mc16_13TeV.364130.Sherpa_221_NNPDF30NNLO_Ztautau_MAXHTPTV0_70_BFilter.deriv.DAOD_HIGG4D6.e5307_e5984_s3126_r10201_r10210_p3529
mc16_13TeV.364131.Sherpa_221_NNPDF30NNLO_Ztautau_MAXHTPTV70_140_CVetoBVeto.deriv.DAOD_HIGG4D6.e5307_e5984_s3126_r10201_r10210_p3529
mc16_13TeV.364132.Sherpa_221_NNPDF30NNLO_Ztautau_MAXHTPTV70_140_CFilterBVeto.deriv.DAOD_HIGG4D6.e5307_e5984_s3126_r10201_r10210_p3529
mc16_13TeV.364133.Sherpa_221_NNPDF30NNLO_Ztautau_MAXHTPTV70_140_BFilter.deriv.DAOD_HIGG4D6.e5307_e5984_s3126_r10201_r10210_p3529
mc16_13TeV.364134.Sherpa_221_NNPDF30NNLO_Ztautau_MAXHTPTV140_280_CVetoBVeto.deriv.DAOD_HIGG4D6.e5307_e5984_s3126_r10201_r10210_p3529
mc16_13TeV.364135.Sherpa_221_NNPDF30NNLO_Ztautau_MAXHTPTV140_280_CFilterBVeto.deriv.DAOD_HIGG4D6.e5307_e5984_s3126_r10201_r10210_p3529
mc16_13TeV.364136.Sherpa_221_NNPDF30NNLO_Ztautau_MAXHTPTV140_280_BFilter.deriv.DAOD_HIGG4D6.e5307_e5984_s3126_r10201_r10210_p3529
mc16_13TeV.364137.Sherpa_221_NNPDF30NNLO_Ztautau_MAXHTPTV280_500_CVetoBVeto.deriv.DAOD_HIGG4D6.e5307_e5984_s3126_r10201_r10210_p3529
mc16_13TeV.364138.Sherpa_221_NNPDF30NNLO_Ztautau_MAXHTPTV280_500_CFilterBVeto.deriv.DAOD_HIGG4D6.e5313_e5984_s3126_r10201_r10210_p3529
mc16_13TeV.364139.Sherpa_221_NNPDF30NNLO_Ztautau_MAXHTPTV280_500_BFilter.deriv.DAOD_HIGG4D6.e5313_e5984_s3126_r10201_r10210_p3529
mc16_13TeV.364140.Sherpa_221_NNPDF30NNLO_Ztautau_MAXHTPTV500_1000.deriv.DAOD_HIGG4D6.e5307_e5984_s3126_r10201_r10210_p3529
mc16_13TeV.364141.Sherpa_221_NNPDF30NNLO_Ztautau_MAXHTPTV1000_E_CMS.deriv.DAOD_HIGG4D6.e5307_e5984_s3126_r10201_r10210_p3529
$W \rightarrow \tau\nu$

Table B.8.: MC16d samples (for 2017 data-taking).

mc16_13TeV.364184.Sherpa_221_NNP30NNLO_Wtaunu_MAXHTPTV0_70_CVetoBVeto.deriv.DAOD_HIGG4D6.e5340_s3126_r10201_r10210_p3529
mc16_13TeV.364185.Sherpa_221_NNP30NNLO_Wtaunu_MAXHTPTV0_70_CFilterBVeto.deriv.DAOD_HIGG4D6.e5340_e5984_s3126_r10201_r10210_p3529
mc16_13TeV.364186.Sherpa_221_NNP30NNLO_Wtaunu_MAXHTPTV0_70_BFilter.deriv.DAOD_HIGG4D6.e5340_e5984_s3126_r10201_r10210_p3529
mc16_13TeV.364187.Sherpa_221_NNP30NNLO_Wtaunu_MAXHTPTV70_140_CVetoBVeto.deriv.DAOD_HIGG4D6.e5340_e5984_s3126_r10201_r10210_p3529
mc16_13TeV.364188.Sherpa_221_NNP30NNLO_Wtaunu_MAXHTPTV70_140_CFilterBVeto.deriv.DAOD_HIGG4D6.e5340_e5984_s3126_r10201_r10210_p3529
mc16_13TeV.364189.Sherpa_221_NNP30NNLO_Wtaunu_MAXHTPTV70_140_BFilter.deriv.DAOD_HIGG4D6.e5340_e5984_s3126_r10201_r10210_p3529
mc16_13TeV.364190.Sherpa_221_NNP30NNLO_Wtaunu_MAXHTPTV140_280_CVetoBVeto.deriv.DAOD_HIGG4D6.e5340_s3126_r10201_r10210_p3529
mc16_13TeV.364191.Sherpa_221_NNP30NNLO_Wtaunu_MAXHTPTV140_280_CFilterBVeto.deriv.DAOD_HIGG4D6.e5340_s3126_r10201_r10210_p3529
mc16_13TeV.364192.Sherpa_221_NNP30NNLO_Wtaunu_MAXHTPTV140_280_BFilter.deriv.DAOD_HIGG4D6.e5340_e5984_s3126_r10201_r10210_p3529
mc16_13TeV.364193.Sherpa_221_NNP30NNLO_Wtaunu_MAXHTPTV280_500_CVetoBVeto.deriv.DAOD_HIGG4D6.e5340_e5984_s3126_r10201_r10210_p3529
mc16_13TeV.364194.Sherpa_221_NNP30NNLO_Wtaunu_MAXHTPTV280_500_CFilterBVeto.deriv.DAOD_HIGG4D6.e5340_s3126_r10201_r10210_p3529
mc16_13TeV.364195.Sherpa_221_NNP30NNLO_Wtaunu_MAXHTPTV280_500_BFilter.deriv.DAOD_HIGG4D6.e5340_s3126_r10201_r10210_p3529
mc16_13TeV.364196.Sherpa_221_NNP30NNLO_Wtaunu_MAXHTPTV500_1000.deriv.DAOD_HIGG4D6.e5340_s3126_r10201_r10210_p3529
mc16_13TeV.364197.Sherpa_221_NNP30NNLO_Wtaunu_MAXHTPTV1000_E_CMS.deriv.DAOD_HIGG4D6.e5340_e5984_s3126_r10201_r10210_p3529
$t\bar{t}$
mc16_13TeV.410470.PhPy8EG_A14_ttbar_hdamp258p75_nonallhad.deriv.DAOD_HIGG4D6.e6337_e5984_s3126_r10201_r10210_p3529
mc16_13TeV.410471.PhPy8EG_A14_ttbar_hdamp258p75_allhad.deriv.DAOD_HIGG4D6.e6337_e5984_s3126_r10201_r10210_p3529
di-boson
mc16_13TeV.361607.PowhegPy8EG_CT10nloME_AZNLOC7Q6L1_WZqqll_mll20.deriv.DAOD_HIGG4D6.e4711_s3126_r10201_r10210_p3529
mc16_13TeV.361604.PowhegPy8EG_CT10nloME_AZNLOC7Q6L1_ZZvll_mll4.deriv.DAOD_HIGG4D6.e4475_e5984_s3126_r10201_r10210_p3529
mc16_13TeV.361603.PowhegPy8EG_CT10nloME_AZNLOC7Q6L1_ZZllll_mll4.deriv.DAOD_HIGG4D6.e4475_e5984_s3126_r10201_r10210_p3529
mc16_13TeV.361605.PowhegPy8EG_CT10nloME_AZNLOC7Q6L1_ZZvvvv_mll4.deriv.DAOD_HIGG4D6.e4054_e5984_s3126_r10201_r10210_p3529
mc16_13TeV.361610.PowhegPy8EG_CT10nloME_AZNLOC7Q6L1_ZZqqll_mqq20mll20.deriv.DAOD_HIGG4D6.e4711_s3126_r10201_r10210_p3529
mc16_13TeV.361600.PowhegPy8EG_CT10nloME_AZNLOC7Q6L1_WWlvlv.deriv.DAOD_HIGG4D6.e4616_s3126_r10201_r10210_p3529
mc16_13TeV.361602.PowhegPy8EG_CT10nloME_AZNLOC7Q6L1_WZlvvv_mll4.deriv.DAOD_HIGG4D6.e4054_s3126_r10201_r10210_p3529

C. Additional Plots for the Z+jets Validation Studies

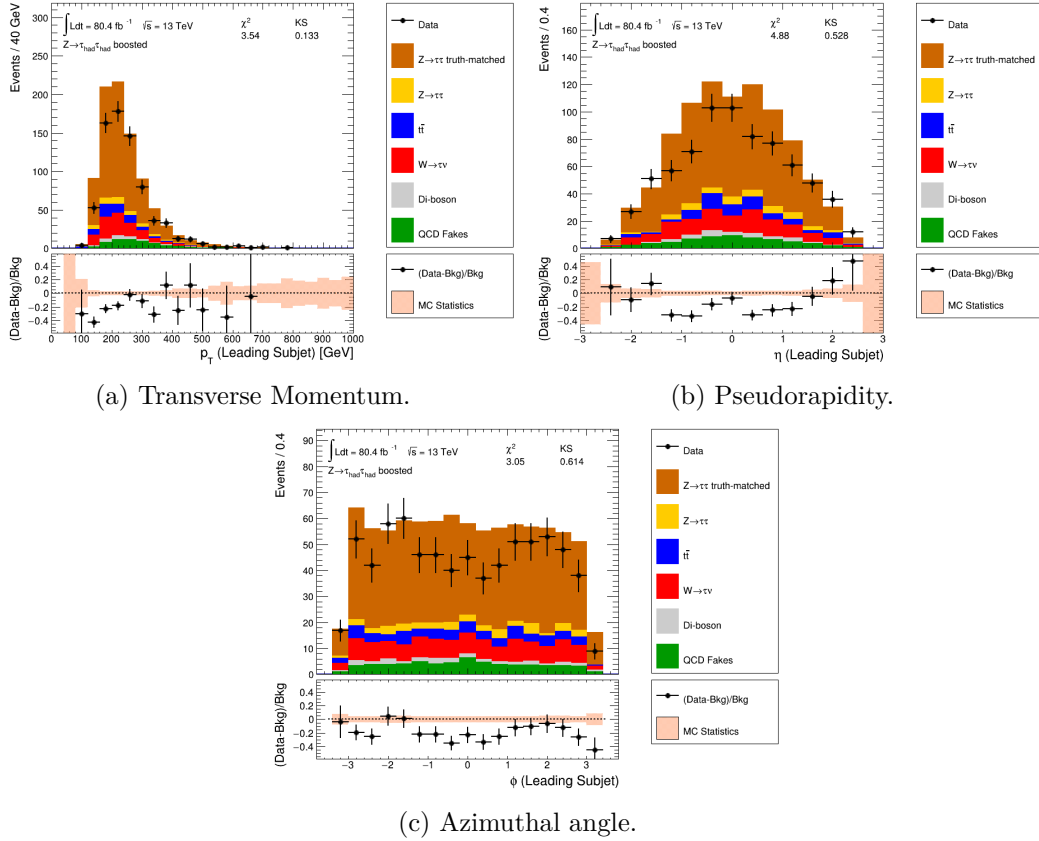


Figure C.1.: Kinematic distributions for the leading di-tau subjet in the signal-region, derived from the Sherpa 2.2.1 $Z \rightarrow \tau\tau(+\text{jets})$ samples.

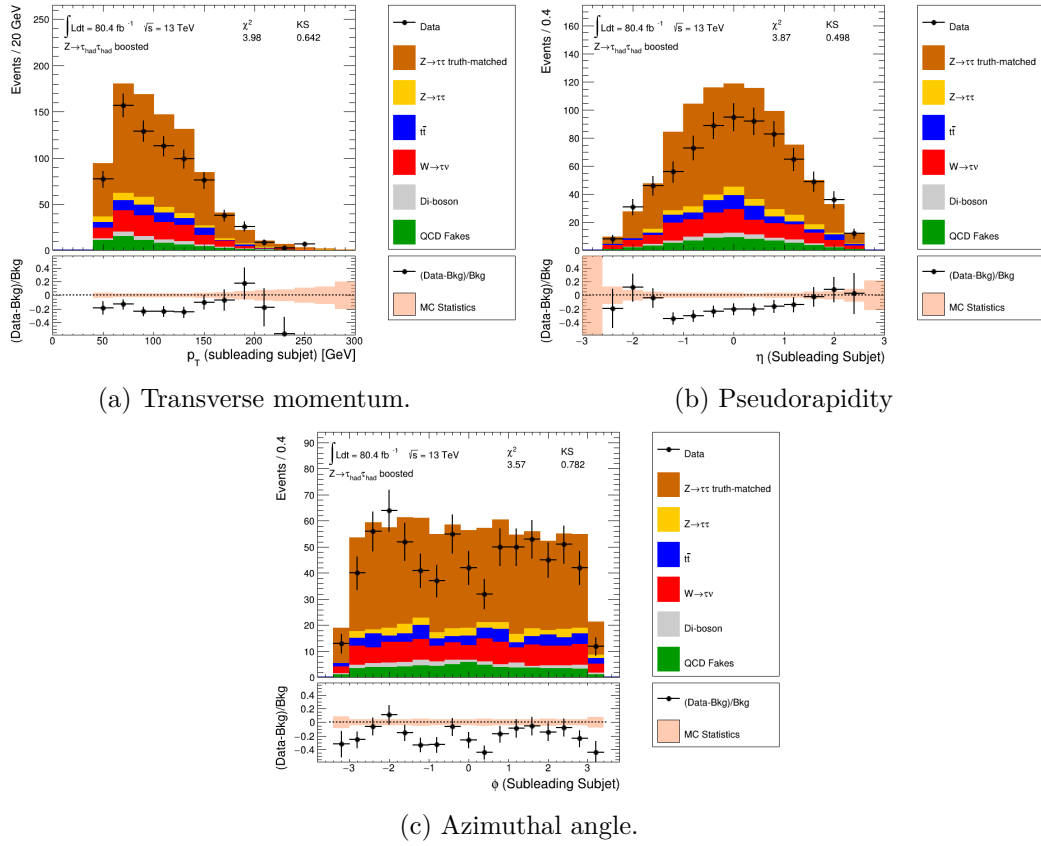
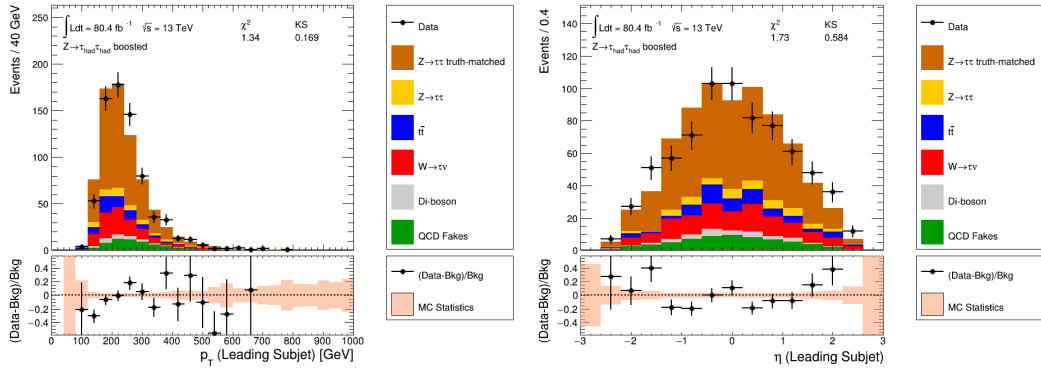
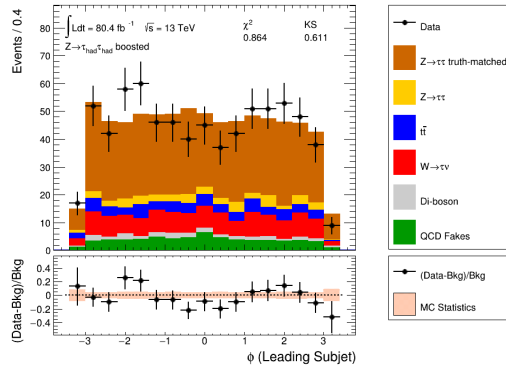


Figure C.2.: Kinematic distributions for the subleading di-tau subject in the signal-region, derived from the Sherpa 2.2.1 $Z \rightarrow \tau\tau(+\text{jets})$ samples.



(a) Transverse Momentum.

(b) Pseudorapidity.



(c) Azimuthal angle.

Figure C.3.: Kinematic distributions for the leading di-tau subject in the signal-region after the application of the identification scale factor (0.75), derived from the Sherpa 2.2.1 $Z \rightarrow \tau\tau(+\text{jets})$ samples.

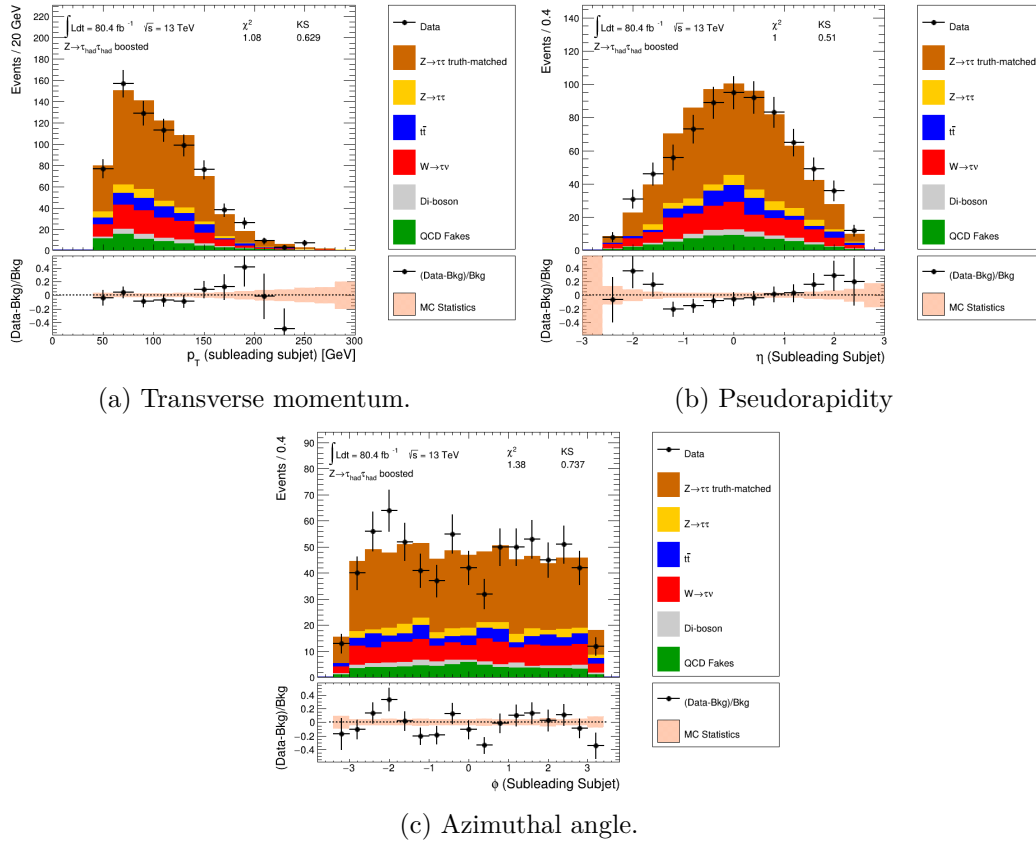


Figure C.4.: Kinematic distributions for the subleading di-tau subjet in the signal-region after the application of the identification scale factor (0.75), derived from the Sherpa 2.2.1 $Z \rightarrow \tau\tau(+\text{jets})$ samples.

Danksagung

Mein Dank gilt all denjenigen, die es mir ermöglicht haben, mein Physikstudium mit einem solch spannenden Projekt abzuschließen. In diesem Zusammenhang möchte ich mich bei Prof. Dr. Arno Straessner, Dr. Wolfgang Mader, David Kirchmeier, Christian Wiel, Paul Moder und allen weiteren Mitgliedern der Arbeitsgruppe für experimentelle Teilchenphysik am IKTP bedanken, die mich wöchentlich und täglich mit wertvollen Anregungen unterstützt und mir wertvolle Hinweise aus ihrem Korrekturlesen gegeben haben. Insbesondere möchte ich ein großes Dankeschön an David und Christian aussprechen, deren Ergebnisse ich im Rahmen dieser Arbeit gewissermaßen zusammenführen durfte.

Selbstständigkeitserklärung

Hiermit erkläre ich, dass ich die vorliegende Arbeit im Rahmen der Betreuung am Institut für Kern- und Teilchenphysik ohne unzulässige Hilfe Dritter verfasst habe und alle verwendeten Quellen als solche gekennzeichnet habe.

Ort, Datum

Unterschrift